MICROFLUIDICS AND BIO-MEMS FOR NEXT GENERATION HEALTHCARE

A DISSERTATION SUBMITTED TO THE GRADUATE DIVISION OF THE UNIVERSITY OF HAWAI‘I AT MĀNOA IN PARTIAL FULFILLMENT OF THE REQUIREMENTS FOR THE DEGREE OF

DOCTOR OF PHILOSOPHY

IN

ELECTRICAL ENGINEERING

AUGUST 2018

By

M Arifur Rahman

Dissertation Committee:

Aaron Ohta, Chairperson
Wayne Shiroma
Victor Lubecke
Olga Boric-Lubecke
Scott Millar

To my beloved sons,

Umair Rahman Ohee
&
Numair Rahman Azan

"Allah will exalt in degree those of you who believe, and those who have been granted knowledge…" – Al Qur'an, Chapter 58, Al-Mujadila (The Pleading Woman), Verse 11

ACKNOWLEDGEMENT

First and foremost, I would like to profoundly thank my PhD advisor, **Dr. Aaron T. Ohta**, who helped me to grow morally and intellectually. Dr. Ohta was always there to listen to me and to give me sincere advice despite my English with a heavy accent. He taught me the process of design thinking, how to ask scientific questions and express my research ideas. Dr. Ohta taught me different ways to approach a research problem. He guided me step by step on how to write conference and journal papers, Instilled self-confidence in me providing, in detail feedback on my writing. Dr. Ohta spent countless hours reviewing my writings, teaching me how to communicate complex experiment results easily in a scholarly gathering. Most importantly, he was always there to meet with me and talk about my ideas, to review the results, and to ask critical questions. Many times, I could find the solution to the long-standing research problems while searching for the answers to his critical questions. Dr. Ohta's enthusiasm and abilities have shaped my interest and understanding of the subject. He allowed maximum freedom in my research, permitting me to take different routes to solve the engineering problems. His trust in me was the constant source of encouragement for me throughout my doctoral program. I could not have finished my dissertation without his constant guidance, true care, and everlasting encouragement. My experience working with Dr. Ohta has been extremely valuable to me, and I will treasure it for the rest of my life.

I am also delighted to express my gratitude to my co-advisor in liquid-metal project **Dr. Wayne Shiroma** for his constant support, encouragements, and help by providing the right tools for the research. I would also like to thank **Dr. Victor Lubecke**, **Dr. Olga Boric-Lubecke**, and **Dr. Scott Miller** for their constructive advice to my dissertation.

I am fortunate to work with a wonderful team of graduate and undergraduate students at the UH Microdevices & Microfluidics Lab and at the MMRL Lab. Thank you, **Julian Cheng**, and **Kainalu Matthews** helping me through many failed experiments until we succeed. I am also thankful to **Dr. Qihui Fan**, **Dr. Ryan Gough**, **Dr. Ashikur Rahman**, **Dr. Richard Ordonez**, **Diana Vera**, **Isaac Lum**, **Kareem Elassy**, **Mohsen Paryavi**, **Richie Chio**, **Matthew Moorefield**, **Kent Sarabia, and Charley Westbrook** for their help, advice, and suggestions.

Thank you to my parents, **Umme Nahar** and **Late M Habibur Rahman**, (may Allah forgive him) for teaching me the true purpose of life, supporting me from thousands of miles away, and taking

care of my sons. Finally, I wish to thank my ex-wife **Mahmuda Morshed** for being a selfless mother to my sons. Thank you for saving our sons from all odds, even while going through the challenges of marital life. Thank you for your courage, and patience in raising our sons alone with utmost love and affection. I was able to continue my doctoral research away from home country, keeping my son's thousands of miles apart from me due to your sacrifices for the kids.

ABSTRACT

Microfluidics and bio-MEMS technology provide essential tools for next-generation healthcare, in areas such as tissue engineering, disease diagnostics, and embryology. Tissue engineering requires precise *in vitro* patterning and multilayer assembly of cells and biomaterial scaffolds, and often requires mesoscale structures to be assembled with microscale resolution. A potential method of micromanipulation for *in vitro* tissue constructs is microassembly by a system employing untethered microrobots. Many microrobots should operate in parallel to increase the throughput of such a bio-micromanipulation system. However, current microrobot systems lack the independent actuation of many entities in parallel. In this dissertation, opto-thermocapillary flow-addressed bubble (OFB) microrobots are studied, and the independent actuation of fifty OFB microrobots in parallel is demonstrated. In addition, individual microrobots and groups of microrobots were moved along linear, circular, and arbitrary 2D trajectories. The independent addressing of many microrobots enables higher-throughput microassembly of micro-objects, and cooperative manipulation using multiple microrobots. Demonstrations of manipulation with numerous OFB microrobots include the transportation of microstructures using a pair or team of microrobots, and the cooperative manipulation of multiple micro-objects. The OFB microrobot system presented here represents an order of magnitude increase in the number of independently actuated microrobots in parallel, as compared to other magnetically or electrostatically actuated microrobots, and a factor of five increase as compared to previous demonstrations of OFB microrobots.

Microfluidics provides precise positioning and manipulation of fluids contained in microscale structures. Microfluidic techniques were used to precisely position room-temperature liquid metal in microtubes, enabling tunable capacitors for the receive coil of a magnetic resonance imaging (MRI) scanner. This liquid-metal-based flexible tunable capacitor functions as the tuning element of the MRI receive coil. In this dissertation, four types of liquid-metal-based tunable capacitors with a high tuning range are demonstrated. The capacitors are easily fabricated by placing a pair of liquid-metal-filled tubes in contact with one another. Tunability is achieved by varying the length of the liquid metal in one of the tubes using a mechanical pump. Four different structures are demonstrated: parallel-tube, folded-tube, coil, and spiral capacitors. The highest measured

tuning ratio is 42:1, and the highest change in capacitance per unit length of the pumped liquid metal is 0.07 $pF.mm^{-1}$.

Microfabricated sensors and actuators for biomedical applications are known as bio-microelectromechanical systems, or bio-MEMS. In this dissertation, a microfluidic bio-MEMS device was designed and made to study embryo viability, which is critical for successful *in vitro* fertilization (IVF) treatment. Conventional methods of embryo evaluation rely mostly on subjective visual analysis of embryo morphological features. Here, two different approaches have been studied for automating the morphological embryo grading and developing a quantitative embryo evaluation process free from human subjective errors. In the first approach, the human blastocyst microscope images were analyzed using image processing tools. Their growth dynamics were studied leading to crucial viability information. In the second approach, the embryo was positioned in between two electrodes inside a microfluidic bio-MEMS device, and their electrical impedance was measured during their development. Experiments with *Artemia* cysts showed a distinct pattern of impedance changes at three different stages of cyst development. The measured impedance changes corresponded to physiological changes as the cyst developed. The change in impedance during the first stage of development provided sufficient quantitative data to predict if the cyst would hatch. This work shows the potential of impedance spectroscopy for developing a non-invasive test to quantitatively determine the health of the embryos.

CONTENTS

LIST OF FIGURES

LIST OF TABLES

CHAPTER. 1 INTRODUCTION

Microfluidics is the science of manipulating and controlling fluids in networks of channels with dimensions of hundreds of micrometers or less. Bio-MEMS (bio-microelectromechanical systems) encompasses microfabricated devices or systems with biomedical applications. Together, microfluidics and bio-MEMS offer portable, cheap, single-use devices and technique for life science research and healthcare applications. The ability of these technologies to manipulate biological cells is extremely useful for various biomedical and industrial applications. One example is the manipulation of cell-seeded scaffolds for creating artificial tissues. The scaffolds for 3D cultures can be made from microfabricated hydrogels that closely mimic the natural cellular microenvironment. This dissertation demonstrates a micromanipulation technique based on microfluidics principles for the precise placement of various micro-object in specific locations described in Chapters 2, 3, 4, and 5 [1]. In addition, the capability of microfluidics to precisely position any liquid has been leveraged in reconfigurable electronics that use liquid metal as conducting elements (Chapter 6) [2]. Also, microfluidic-based cell manipulation enables single-cell analysis, which has been demonstrated in this dissertation by micromanipulation of embryos for monitoring their electrical properties (Chapter 7) [3].

1.1 Microrobot for Micromanipulation

Micromanipulation is a capability that benefits many application areas, including the fabrication of electronic circuits and devices [4], single-cell analysis [5], drug delivery [6], pathogen isolation [7], minimally invasive surgery [8], and tissue engineering [9]. While there are many methods and technologies that are capable of manipulating microscale objects, this dissertation will focus on microrobots, which are untethered sub-millimeter actuators. Microrobots offer a variety of manipulation methods, including contact and noncontact manipulation. Microrobots also generally feature robust, automated control systems, making it easier for operators of various skill levels to perform micromanipulation. Several microrobotic actuation mechanisms suitable for micromanipulation will be described. Desirable features of micromanipulation using microrobots will be discussed, and recent progress in implementing these features will be discussed, with an emphasis on opto-thermocapillary flow addressed bubble microrobots.

1.1.1 Microrobot Actuation Mechanisms

Microrobotic actuation spans a variety of methods, including magnetic actuation, electrostatic actuation, biohybrid systems, optothermal actuation, and combinations of these approaches.

1.1.1.1 Magnetic Forces

A popular approach to the actuation of microrobots is the use of magnetic force [9–12]. Magnetic forces can be relatively large, and magnetic fields can penetrate human tissues with minimal side effects. Magnetic actuation is also amenable to integration with other systems, such as imaging systems: magnetic resonance imagers can be used to actuate magnetic microrobots [13-14]. The magnetic fields can also act upon many magnetic microrobots at once [12,15]. Drawbacks to magnetic actuation include difficulties in creating highly localized magnetic fields, and the high current requirements of electromagnets.

1.1.1.2 Electrical Forces

Electrical forces are also popular for microscale actuators, and have been employed for microrobot actuation [4,16–18]. Electric fields easily localized, helping to increase the actuation resolution. The equipment and setup for electrical actuation is also usually simpler and more compact compared to other actuation methods. However, high electric fields may have harmful effects on some types of microscale objects, such as living cells. Electrical actuation in electrically conductive fluids can also be challenging, due to joule heating and undesirable electrically conductive pathways.

1.1.1.3 Biohybrid Systems

Naturally occurring organisms such as motile cells and bacteria are capable of microscale locomotion, along with other capabilities, such moving along chemical gradients. Thus, there has been efforts to harness these organisms to actuate microrobots [19–23]. This is a promising area of work, but living cells are subject to additional constraints on their working environment.

1.1.1.4 Multiple Forces

Combinations of the aforementioned actuation mechanisms are also used, which helps to address shortcomings of or add functionality to a particular actuation method. For example, biohybrid systems often need an additional applied field to steer the bacteria- or cell-powered microrobots, such as a magnetic field [7], an electrical field [24], or an optical field [25]. Other combinations of actuation mechanisms have also been explored, such as magnetic actuation with an electrostatic anchoring force [26], or optothermal bubble generation with acoustic-driven fluid streaming [27].

1.1.1.5 Optothermal Forces

Optothermal forces are thermal forces that are caused or controlled by an optical source [1]. It is straightforward to focus light into microscale patterns, so high-resolution actuation forces can be created without any microfabrication. Optothermal forces can be gentler on payloads as compared to optical manipulation that directly converts the photon momentum into mechanical force, as the objects under manipulation do not have to be directly illuminated by the light [1, 27, 28]. However, setting up optical equipment is significantly harder than the other methods, and usually more expensive. Optothermal actuated microrobot has an advantage over other methods of actuation, that it is least dependent on the surrounding environmental condition. The microrobot system which has been demonstrated in this dissertation is optothermal actuated bubble microrobots.

1.1.2 Opto-thermocapillary Flow Addressed Bubble (OFB) Microrobots

A microrobot actuation mechanism that allows the parallel actuation of many microrobots is opto-thermal actuation, in which optical energy is converted to thermal energy. This is the mechanism utilized by opto-thermocapillary flow-addressed bubble (OFB) microrobots, which are gas bubbles in liquid media that move along optically generated thermal gradients [28]. OFB microrobots are capable of microassembly [28], single-cell assembly [29, 30], cell-laden hydrogel assembly [30], and single-cell poration [32]. Compared to other methods of actuation discussed above, OFB microrobots have less dependence on the electrical and magnetic properties of both the object under manipulation and the media used for actuation. More importantly, each OFB

microrobot is optically addressed, so it is straightforward to maintain independent control even when moving many microrobots at once. For this work, “independent control” means the uncoupled actuation of individual microrobots, allowing motion along different trajectories at different velocities. The OFB microrobot can operate in conventional cell culturing environment such as in an open reservoir [33]. In addition, the robust control system is able to maneuver the microrobots for advance robotic navigation like path planning, collision detection, and collision avoidance [34].

1.1.3 Micromanipulation with Microrobots

Micromanipulation with microrobots benefit from the capabilities that are highlighted in this section. The recent progress in each of the capabilities is mentioned, with an emphasis on how opto-thermocapillary bubble microrobots can achieve those capabilities.

1.1.3.1 Increasing Throughput of Micromanipulation

A straightforward method to increasing the throughput of micromanipulation operations is to increase the actuation velocity of the microrobots. Microrobots have been actuated at up to tens of cm. per second [35], but this means that the speed of the control system and the microrobot position-sensing system (usually an optical microscope with a camera) also needs to be sufficient to accurately move the microrobot. The throughput of micromanipulation using microrobots can also be increased by using multiple microrobots. Magnetic and electrical actuation are capable of moving multiple microrobots in parallel [12, 15, 17, 18, 35] but if global actuation signals are used, microrobot trajectories are usually coupled to one another. To decouple the movements of multiple microrobots, specialized working surfaces can be used to create localized forces that force the microrobots to travel along different trajectories [36, 37]. Alternatively, each microrobot can be designed to have an individualized response to a global actuation signal, such as by varying the dimensions of the actuation structures [12, 15, 17, 38, 39].

Biohybrid microrobots such as bacteria-propelled microrobots can have motion that is uncoupled from one another [20, 40]. This makes this approach promising for multiple microrobot

micromanipulation [21]. However, to fully realize this promise, more work needs to the done on the positioning accuracy and repeatability of biohybrid microrobots.

Optothermal actuation allows the parallel actuation of many microrobots, as demonstrated by opto-thermocapillary flow-addressed bubble (OFB) microrobots. The OFB microrobots are gas bubbles in a liquid that move along optically generated thermal gradients [28]. As the OFB microrobots are optically addressed, the uncoupled actuation of individual microrobots can be achieved, even when moving many microrobots at once.

1.1.3.2 Increasing Resolution of Micromanipulation

Micromanipulation with microscale precision (or better) is important for applications such as tissue engineering. Precise positioning of a payload can be achieved by employing grasping or caging [1, 15]. Caging refers to positioning multiple microrobots surrounding an object so that neighboring microrobots are placed at a distance smaller than the size of the micro-object. Grasping refers to multiple microrobots in contact with a micro-object. OFB microrobots have demonstrated micromanipulation with increased resolution with caging and grasping [34]. As an example, a spherical OFB microrobot has difficulty pushing or pulling a spherical micro-object on a linear trajectory [33]. However, multiple OFB microrobots were able to grasp spherical and planar micro-objects with increased spatial and temporal resolution [1, 33].

1.1.3.3 Increasing Robustness of Control Systems

The functionality of the various types of microrobots is highly dependent upon a robust control system. For example, the actuation of multiple OFB microrobots was possible for a few years (first demonstrated in 2012 [41]), but it was constrained by manual control by a single operator. This is made more complicated since OFB microrobots have a risk of merging when in contact with each other. The OFB microrobot system was made more robust by using a closed-loop control system capable of actuating each microrobot with knowledge of the location of other microrobots and micro-objects within the workspace [34]. Vision-assisted image-feedback control allowed path planning, grasp planning, collision avoidance, and cooperative micromanipulation using multiple

microrobots [34]. The closed-loop control increased the accuracy of the microrobot placement by 50% compared to one iteration of open-loop actuation.

1.1.3.4 Operating in Conventional Cell Culturing Environment

Microrobot actuation in cell-compatible solutions like phosphate-buffered saline (PBS) enables cell microassembly. Moreover, a cell-friendly microrobot bio-micromanipulation system can operate in an open reservoir, making it compatible with standard cell culture plates. However, it can be challenging to actuate microrobots in electrically conductive PBS solution in an open reservoir. In addition, it is also challenging to control many microrobots at once. Among the actuation methods mentioned above, electric-field-based micromanipulation systems can suffer complications when actuated in electrically conductive fluids such as PBS. Magnetic microrobots are not hampered by electrically conductive fluids, but are limited by the divergence or resolution of the globally applied magnetic fields, making it challenging to independently actuate multiple magnetic microrobots. Microrobots that use magnetotactic or flagellated bacteria as a propulsion mechanism can operate in electrically conductive fluids and open reservoirs, but it is hard to achieve rapid and directional actuation independently using bacterial propulsion. Opto-thermocapillary flow-addressed bubble (OFB) microrobots are generated and actuated by opto-thermal phenomena, and can address the challenges mentioned above. An OFB microrobot system is not affected by the electrical and magnetic properties of the environment, and is capable of actuation in PBS solution in an open reservoir [14]. The optical addressing of the OFB microrobots is also suitable for controlling many of them independently.

1.2 Liquid Metal for Reconfigurable Electronics

1.2.1 Liquid Metal as Tuning Element in Reconfigurable Electronics

Reconfigurable RF devices can respond dynamically to complex RF environments. Liquid metals have the potential to enable reconfigurable devices that cannot be implemented by more conventional materials and technologies. Reconfigurable electronics can adapt to specific tasks or environments, allowing dynamic performance optimization. In addition, multifunctionality,

miniaturization, and low power consumption are critical for mobile RF applications. Generally, RF reconfigurability has been achieved using devices such as MEMS [42], varactors [43], and barium strontium titanate (BST) capacitors [44]. An alternative is to use liquid metals as the conductive elements of RF devices, enabling reconfigurability. Liquid metal has been used in reconfigurable RF devices such as antennas [45–47], switches [48], and resonators [49].

In the past, the liquid-metal devices were not popular because the only naturally occurring metal that exists as a liquid at room temperature was highly toxic mercury. However, in the last few decades several non-toxic gallium-based liquids-metal alloys have become commercially available. One such alloy, Galinstan™, is composed of 68.5% gallium, 21.5% indium, and 10.0% tin, and is a stable liquid across a wide temperature range (-19 °C to over 1300 °C) [48]. Galinstan also has a high RF conductivity (3.83×10^6 $S.m^{-1}$) [50], making it a suitable substitute for mercury in RF applications. The liquid nature of Galinstan is leveraged in this dissertation and liquid-metal tunable capacitor is demonstrated which has the potential to fabricate high SNR tunable MRI receive coil.

1.2.2 Liquid Metal Actuation Mechanisms

Many reconfigurable RF devices made with gallium-based liquid metal use mechanical pumps for actuation [47]. However, electrical actuation is more attractive for commercial reconfigurable devices. Mechanisms for electrically controlling the motion of gallium-based liquid metals include continuous electrowetting, electrocapillary actuation, and self-powered actuation of the liquid metal. Continuous electrowetting (CEW) moves liquid metal by electrically manipulating its surface tension [51]. Electrocapillary actuation (ECA) is another electrical surface-tension manipulation technique [52], in which a DC bias is applied across the liquid metal and the electrolyte to alter the surface charge and liquid-metal surface tension. Self-actuation of liquid metal is an electrochemical actuation technique [53]. However, the liquid-metal devices fabricated in this dissertation use pressure gradients to actuate the liquid metal for reconfigurability.

Dynamic RF hardware capable of serving a multitude of frequency bandwidths continues to be an area of intense study. One important element in reconfigurable RF systems is a tunable capacitor. Conventional methods enabling capacitive tuning include varactors, ferroelectrics with variable

permittivity, and MEMS variable capacitors. Varactors are inexpensive, easy to integrate, and allow analogue tuning. Barium strontium titanate (BST) capacitors offer higher power handling and breakdown field strength compared with varactors. MEMS variable capacitors have low loss, use low power, and offer high isolation. However, all these technologies can have non-linear behavior that limits tunability [42–44, 54]. The tuning ratio achieved by angular vertical comb-drive capacitors, BST capacitors, and MEMS variable capacitors are 31:1 [43], 2.59:1 [44], and 9:1 [42], respectively. An alternate method for realizing reconfigurable electronics is the use of liquid metal as a conductive element [55, 56].

1.2.3 Liquid-Metal Tunable Capacitor for MRI

A high signal-to-noise ratio (SNR) is critical for faster MRI (magnetic resonance imaging) data acquisition. MRI scanning is relatively slow, as scanning for longer durations increases the SNR. However, longer scanning limits the spatial resolution and diagnostic image quality and typically results in long acquisition times that are prone to motion artifacts. Recent progress in advanced image reconstruction [58, 59], higher-field scanners [59], use of contrast agents [60], and receive coils with higher gains [61][62] have increased the SNR.

An MRI procedure starts by placing the patient in the large static magnetic field. Hydrogen protons align with the externally applied static magnetic field to create a net magnetization vector. Radio-frequency (RF) pulses are applied at the resonance frequency of the proton spin. The RF pulses excite the magnetization, and the protons can absorb energy and jump to a higher energy state. Now, the gradient of the magnetic field is used to encode spatial information by changing the resonant frequency in three-dimensional space. When the RF signal is stopped, energy is given off as the spins move from high to low energy states. The absorbed RF energy is retransmitted at the resonance frequency and can be detected with RF antennas or “receive coils” placed around the patient. These received RF signals, which represent partial coded information, are amplified, digitized, stored, and analyzed, becoming the MR images. The use of receive coil arrays, and parallel imaging can improve the SNR [58, 64]. The receive coils and arrays are built for specific areas of the body. Currently, the coils are made of high-quality rigid electronic components packaged using stiff medical-grade materials. A rigid receive coil fails to “hug” the area of the patient under examination. Moreover, if the patient is a smaller person or child, there will be a gap

between the patient body and the coil, which will reduce the SNR. Sometimes, soft padding is added to the rigid coil chassis for patient comfort, but this also affects the SNR. Since a good coil fit is critical for high SNR images, research groups have demonstrated flexible receive arrays using conductors sewn into fabric [64], screen printing on flexible substrates [65], a mercury-based conductor [66], electro-textile-based RF coils [67], and semi-flexible copper tape [68]. These techniques provide flexible, light, and scalable manufacturing of RF coils with relatively high SNR performance. However, none of the techniques provide tunability of the antenna element during the MRI procedure. Here, we hypothesize that non-toxic liquid metal has the potential to build flexible, lightweight, and tunable RF receive coil arrays which can be tuned real-time for high SNR. We fabricated the prototype of one antenna element on PET substrate where the fixed capacitors were built with copper tape, and the tunable capacitor was fabricated with non-toxic Gallium based liquid-metal alloy. In addition, a tunable liquid-metal tube capacitor was fabricated with a high tuning ratio.

1.3 **Assessment of Embryo Viability**

In vitro fertilization is a popular treatment for infertility which has been evolving since the first successful treatment three decades ago. Numerous research has been carried out, and innovative technology has been in practice to aid the IVF process. However, the efficiency remains relatively poor, with most patients requiring more than one treatment cycle to obtain a birth. The overall success rate for this expensive procedure is below 30% [69]. The reasons for IVF failure can be broadly divided into three groups: decreased endometrial receptivity, defective embryonic development, and multifactorial effectors [70]. Decreased endometrial receptivity and multifactorial effectors like suboptimal ovarian stimulations are conditions of the patient that need to be treated clinically. On the other hand, the effect of the defects in embryonic development can be minimized by quantifying the health of the embryo during the preimplantation stage.

Implanting multiple embryos increases the chances of getting pregnant, but while this approach has helped to boost IVF pregnancy rates, it has also led to large numbers of multiple pregnancies. [71]. Multiple pregnancies can easily be stopped by transferring a single embryo to the mother's uterus each cycle, but this will also reduce the pregnancy rates per cycle. Many times, the patient

drops out of multiple cycles of IVF for various reasons like economic situations and psychological trauma [72]. In such cases probability of transferring a viable embryo by chance at the later cycles is diminished. The IVF procedure can be benefited by an advanced morphological grading technique using image-processing algorithms. Ultimately, a quantitative embryo grading technique is desirable

This dissertation reports on two approaches to improve the embryo grading practices. The first approach is to analyze the blastocyst growth rate in real-time using an image-processing algorithm. The second approach is to develop a quantitative embryo grading technique by measuring the electrical impedance of the embryo over a specific period of its development and correlate the data with its biological growth.

1.3.1 Morphological Assessment

Currently, embryos are assessed primarily based on their morphological features in the IVF laboratory [73]. However, despite a large number of clinical studies and published results, there is not a gold standard which can result in the best success. Several morphological features display some association with embryo viability, but it is not always clear how these features should be weighted relative to one another. Besides, the available grading systems rely mostly on visual information obtained by the embryologist and are thus subject to inter-observer variance [74]. Automated image analysis may add objectivity to the process of embryo selection and, might lead to an improvement in the identification of viable embryos.

Recent developments in preimplantation genetic diagnosis (PGD) have led to human embryos being classified for their chromosomal content [75]. PGD is a quantitative analysis of the embryo health which includes an invasive biopsy of the embryo and detailed screening of one cell for chromosome normalcy. The significant disadvantages of this approach are the need to remove one or two blastomeres from embryos for diagnosis and added cost of screening to the patient [76]. An automated image processing algorithm has been developed to analyze human embryos at the blastocyst stage (day 5/6), which provide a robust analysis of human blastocysts. The algorithm

processes the image in real-time and compares the data with pre-recorded data from Euploidy blastocyst.

1.3.2 Impedance Spectroscopy for Embryo Viability Test

The discussion above suggests that a quantitative embryo grading system has the potential to determine the viability of an embryo for IVF. Impedance spectroscopy in a microfluidic environment can satisfy these requirements. Microfluidics allows the addressing of a single embryo for testing. The idea of this approach is to measure the electrical impedance of the embryo over time. When the embryo grows, or cells divide, the metabolic activities and cell mass increase result in a net change in electrical impedance across the embryo. Our preliminary experiment shows that the change of impedance is correlated with the biological growth of the embryo. By measuring the impedance of an embryo over time, important health information can be obtained. We have carried out our preliminary experiments on *Artemia* cysts. A cyst, like an embryo, is in the prenatal development stage; however, a cyst has a hard shell, and an embryo does not. *Artemia* cysts were used in this study due to their hardiness, cost, and availability.

A rapidly prototyped microfluidic device was fabricated that allowed precise positioning of an Artemia (brine shrimp) cyst between two electrodes, and enabled the measurement of impedance during its growth. The microfluidic device described in this dissertation was designed for the health monitoring of the cysts by measuring their impedance as they matured. This device should also be applicable for measuring embryo development. In the first phase, the dielectric properties of cysts were measured as they dried out over time [3]. In contrast, next phase of experiment seeks to quantify embryo development prior to hatching.

1.4 Outline of the Dissertation

This dissertation presents the application of microfluidics and bio-MEMS in four healthcare-related projects. First, optically controlled bubble microrobots were developed for the purpose of assembling living cells into larger structures. This is a step towards assembling tissues and organs outside of a human body, which can be used for more accurate testing of drugs and other therapeutics. Second, liquid-metal-based flexible tunable capacitors for flexible and tunable MRI

receive coils were created. These capacitors have the potential to improve the SNR of MRI receive coils while providing a good fit to patients of all ages. Third, a semi-automatic embryo grading system was developed, where the microscope image of a human blastocyst is analyzed to determine the most viable embryo among a group. Fourth, a non-invasive embryo grading system was developed where the pattern of electrical impedance changes across an embryo due to its biological growth was measured.

In Chapter 2, optothermocapillary flow-addressed bubble microrobot generation and actuation is discussed including single and multiple microrobot actuation. This chapter also discusses the actuation mechanism of the opto-thermal microrobot and different variations of the experimental setup used for optimum efficiency. In addition, the microrobot control system is detailed which is a computer-generated holographic control system. At last, independent actuation of twelve and twenty-four microrobots are demonstrated.

In Chapter 3, the independent actuation of 50 microrobots demonstrated in parallel on a titanium-coated glass slide. The microrobots were simultaneously maneuvered in different directions to demonstrate uncoupled parallel actuation. The multidirectional maneuverability of the microrobots along various trajectories was demonstrated, and provided the flexibility needed to manipulate micro-objects into various orientations. The independent actuation of multiple OFB microrobots enables cooperative micromanipulation, and enhances the assembly capabilities of this microrobot system. Multiple OFB microrobots working together are capable of exerting more force on microstructures. In addition, cooperative micromanipulation by a team of OFB microrobots was used to simultaneously transport multiple micro-objects in less time compared to manipulation using a single microrobot.

In Chapter 4, the parallel actuation of nine OFB microrobots in PBS (phosphate-buffered saline) solution in an open reservoir is presented. The microrobots were independently actuated along different trajectories using a computer-generated holographic (CGH) control system, demonstrating the uncoupled actuation of each of them. In addition, the collaborative manipulation of several glass microbeads was demonstrated in an open reservoir containing PBS. The glass microbeads were transported over several millimeters using two or three microrobots. During the transportation, the microscope stage was moved for coarse motion, and CGH control was used for

the fine actuation of the microrobots. These functionalities of the OFB microrobot system make it attractive for tissue engineering applications.

In Chapter 5, a hybrid closed-loop control system for an OFB microrobot system was developed. The hybrid system uses an open-loop computer-generated holographic control system (developed in LabVIEW) to generate the optical patterns necessary to actuate multiple OFB microrobots simultaneously. The closed-loop part of the hybrid system includes an image-processing algorithm (developed in MATLAB) that provides image feedback control; this allows the actuation of multiple OFB microrobots and the knowledge of the locations of the objects under manipulation. The control system also includes a grasp-planning algorithm (developed in MATLAB) that determines the shortest path and suitable grasping point of micro-objects. Finally, the closed-loop automatic actuation of four microrobots was demonstrated; the OFB microrobots cooperatively caged a star-shaped SU-8 microstructure and transported it to the desired location within the workspace. The hybrid control system achieved higher accuracy compared to open-loop actuation.

In Chapter 6, a liquid-metal tunable antenna element is demonstrated which is fabricated on a flexible substrate to use in MRI receive coil. The receive coil can be tuned in real-time to resonate at the Larmor frequency during MRI scanning. In addition, its flexibility allows the coil to fit at the body part of the patient which is under examination, potentially increasing the SNR of the scanner. Chapter 6 also presents four types of liquid-metal-based tunable capacitors with a high tuning range. Four different structures are demonstrated: parallel-tube, folded-tube, coil, and spiral capacitors. The highest measured tuning ratio is 42:1, and the highest change in capacitance per unit length of the pumped liquid metal is 0.07 $pF.mm^{-1}$.

In Chapter 7, a semi-automatic embryo grading system is presented, in which the microscope image of the human blastocyst is analyzed to determine the most viable embryo. An image-processing algorithm was developed which can measure the growth rate of the embryo and compare it with the previously recorded euploid (normal chromosome) data, aiding the morphological embryo grading process at blastocyst stage for subsequent transfer to the patient.

Chapter 7 also presents a non-invasive embryo grading system where the change of electrical impedance due to its biological growth is measured across an embryo to determine its health in vitro. Here, the impedance of single Artemia (brine shrimp) cysts are measured in a microfluidic

channel and in an open reservoir. The measured impedance corresponds to distinct stages in the cyst development, and can be used to predict if the cyst hatches. As a cyst is like an embryo in its prenatal development stage, these measurements show the potential of this technique for quantifying the health of embryos during development.

CHAPTER. 2 INDEPENDENT ACTUATION OF MULTIPLE BUBBLE MICROROBOTS

Microrobots are untethered sub-millimeter actuators capable of manipulating micro-objects including living cells [9, 29, 30, 78–83], and are useful for applications such as targeted therapeutics [9], molecular delivery to targeted cells [32], minimally invasive surgery [83], and tissue engineering [85, 86]. Microrobots can be actuated using a wide variety of methods, including electrostatic actuation [17, 87], magnetic actuation [35, 78–82, 88, 89], a combination of electrostatic and magnetic actuation [36, 90], optothermal actuation [1, 28, 30, 31, 90–92], a combination of acoustic and optothermal actuation [26, 94], and bacteria-propelled swimming [25, 95–97]. Micro-manipulation using multiple microrobots can increase assembly throughput and reduce manipulation time. For example, a large team of independently controlled microrobots can also split into multiple smaller groups to carry out various micromanipulation tasks in parallel [97]. Moreover, using many microrobots in parallel allows the cooperative manipulation of micro-objects that are too heavy or unwieldy to be transported by a few microrobots. Swarms of multiple microrobots are suitable for the assembly of cell-laden microgels, which are used to create *in vitro* tissue constructs [86, 99]. Similarly, an independently controlled swarm of microrobots can perform molecular or drug delivery [32] to multiple specific cells simultaneously with single-cell resolution.

Electrostatic and electromagnetic actuation can manipulate multiple microrobots in parallel, but it is challenging to move microrobots along independent trajectories using global actuation signals that couple microrobot motion to one another. One solution is to vary the physical properties of the microrobots so that each one has a different response to a global actuation signal [12, 17, 87]. Another approach is the use of specialized working surfaces with arrays of transducers that create localized actuation forces [12, 36, 37]. This enables the simultaneous actuation of microrobots along different trajectories, but has so far been limited to 10 microrobots or less [37]. The motion of bacteria-propelled microrobots is uncoupled to one another, but current levels of control of the trajectories of these microrobots are less precise than other types of microrobots. To summarize, despite progress in the parallel actuation of microrobots, it remains challenging to actuate many microrobots independently; the highest number to date using electrostatic or electromagnetic

actuation is eight microrobots [17]. A microrobot actuation mechanism that allows the parallel actuation of many microrobots is opto-thermal actuation, in which optical energy is converted to thermal energy. This is the mechanism utilized by opto-thermocapillary flow-addressed bubble (OFB) microrobots. This chapter explains the mechanism for single and multiple OFB microrobot generation and actuation along with the different variations of experimental setups used for optimum optical performance. In addition, this chapter demonstrates independent actuation of 12, and 24 OFB microrobots in parallel.

2.1 OFB Microrobot Generation

Opto-thermocapillary flow-addressed bubble (OFB) microrobots are gas bubbles in a liquid media actuated using localized optical patterns [29]. These localized patterns, which are also used in optical tweezers, can be generated by using optical devices such as micromirrors [99], scanning mirrors [100], and spatial light modulators (SLMs) [101]. In comparison to other microrobot methods that have been used for micro-transportation, OFB microrobot actuation is less dependent on the optical, electrical, and magnetic properties of the objects under manipulation and the surrounding media. This is attractive for independent actuation.

2.1.1 Single OFB Microrobot Generation

Focused laser light of various wavelengths can be remotely used to generate OFB microrobots by localizing heating. The heating can cause mechanical deformation of the medium through phase change or can change the surface tension of the liquid around the microrobot, propelling it using the Marangoni effect. These two phenomena generate and drive the microrobot.

To generate an OFB microrobot, a light source such as a laser is focused onto the floor of the substrate [29]. The substrate is coated with light-absorbing material constituting the floor of the fluidic chamber, which converts the optical energy into thermal energy. The localized hot spot at the focal point vaporizes a tiny volume of liquid and generates the OFB microrobot (Fig. 2.1).

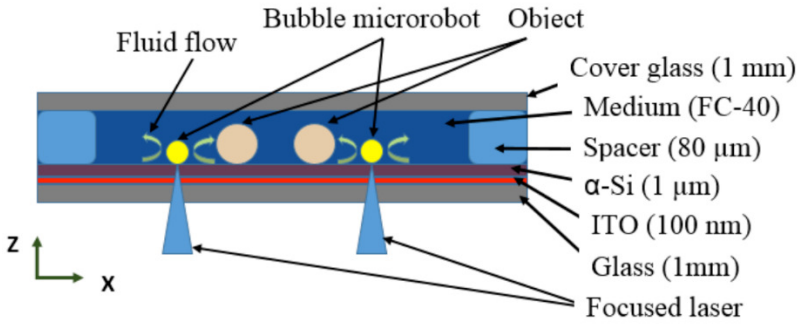

Figure. 2.1. Side view of the generation mechanism of opto-thermocapillary flow-addressed bubble microrobots (OFB). A fluidic chamber was formed over the absorbing layer by bonding a 1-mm thick glass slide over the substrate with 80 µm-thick spacers. Focused laser beams generate a localized hot spot vaporizing small amount of the working fluid and generating the bubble.

2.2 Microrobots Actuation Technique

A single focused laser beam can be used to create a bubble microrobot and actuate the microrobot using thermocapillary forces. Thus, multiple microrobots can be controlled by multiple focused beams of light. Parallel actuation of several OFB microrobots has been demonstrated by quickly switching the laser position between several discrete spatial locations [91]. However, it is also possible to control multiple OFB microrobots with a single laser using a setup similar to holographic optical tweezers (HOT). In a HOT system, the incoming laser beam is modulated to control the light wavefront, usually by holograms displayed on an SLM, shaping the single beam into an array of beams [101]. The OFB system described in this dissertation uses an SLM to phase modulate the laser beam wavefront to create an array of laser spots focused on the absorbing layer of the substrate beneath the OFB microrobots. Each laser spot creates the opto-thermocapillary heating effect necessary for OFB microrobot actuation.

2.2.1 Marangoni Effect

As mentioned earlier, OFB microrobot is a gas bubble in liquid media. When a laser is focused near the body of the microrobot, the laser beam absorbed by the light absorbing floor beneath it and can locally heat the air-fluid interface creating a spatial surface tension gradient. The spatial dependence of the surface tension induces a flow called Marangoni flow at the interface. The Marangoni effect cause the mass transfer along the interface between two fluids (here, gas and fluid) due to surface tension gradient. Primarily, surface tension depends on both the temperature

and chemical composition of at the interface. As a result, Marangoni flows may be created by gradients of either temperature or chemical concentration at the interface, or both. In case of temperature-triggered flow, it is called thermocapillary flow.

2.2.2 Thermocapillary Flow

Marangoni effect due to the local temperature gradient at the interface of two liquids is called thermocapillary effect. The thermal gradient works as stimulus to the thermocapillary stress (force per area), which is given by

$$\sigma_t = \nabla\sigma \tag{2.1}$$

where σ is the surface tension in $N.m^{-1}$ in 1D. The variation of σ due to thermal effects is given by Eq. 2.2 [102],

$$d\sigma = \gamma_t dT \tag{2.2}$$

where γ_t is the susceptibility of surface tension to variations in the temperature in $N.m^{-1}.K^{-1}$. The value of γ_t is different for different species of liquid. Thermocapillary stress due to laser heating can be given from this relation by

$$\sigma_t = \gamma_t \frac{dT}{dx} \tag{2.3}.$$

The thermocapillary force per length can be calculated from this relation.

2.2.3 Opto-thermocapillary Actuation

The OFB microrobots are actuated by optically induced thermocapillary effects, which have been detailed above. To actuate an OFB microrobot, a radial temperature gradient is created by the absorption of a circular laser beam that is incident on the substrate. In the presence of a bubble, the temperature gradient generates a surface-tension gradient along the air/liquid interface, and a thermocapillary fluid flow around the bubble. This results in a net movement of the bubble towards the region with the highest temperature, which corresponds to the position of the laser on the substrate. Once the bubble is centered about the laser beam, the forces on the bubble are balanced,

stably trapping the OFB microrobot. The temperature gradient causes the OFB microrobots to travel towards the localized hot spots, which correspond to the positions of the laser beam. When the carrier beam is moved the lateral component of the thermocapillary force pulls the microrobot towards the center of the localized hot spot. Thus, each microrobot is controlled by the position and motion of the light patterns (Fig. 2.2).

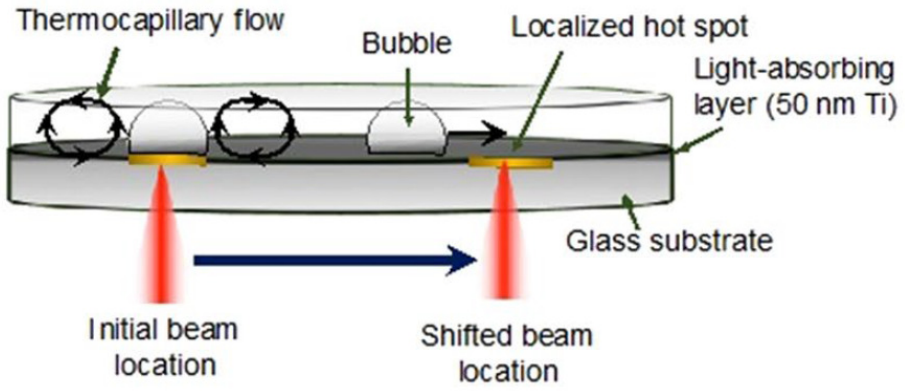

Figure. 2.2 Opto-thermocapillary flow-addressed bubble (OFB) microrobots actuation technique. (**a**) The OFB microrobots are gas microbubbles that are generated by the laser heating of a light-absorbing layer on the substrate. Thermocapillary forces created by the laser-generated temperature gradient are used to actuate the bubble microrobots.

The boundary condition at the liquid/gas interface of the bubble can be described by the following equations:

$$\eta \frac{\partial u}{\partial \boldsymbol{n}} = \gamma_T \frac{\partial T}{\partial \boldsymbol{t}} \tag{2.4}$$

and

$$\gamma_T = \frac{\partial \gamma}{\partial T} \tag{2.5}$$

In Eqn. 4 and Eqn. 5 $\boldsymbol{n}$ and $\boldsymbol{t}$ are the unit vectors normal and tangential to the bubble interface, η is the dynamic viscosity of the liquid, u is the tangential component of the liquid velocity vector due to thermocapillary flow at the liquid/gas bubble interface, T is the temperature, and γ_T is the surface tension [104, 105]. Eqn. 2.4 and Eqn. 2.5 show that a high thermal gradient will create a high shear stress, resulting in a stronger thermocapillary force for actuation.

2.3 Multiple OFB Microrobot Generation

Multiple microrobots were generated primarily using a similar method as explained for single microrobot generation, except the wavefront of the laser beam was shaped using a programmable liquid crystal on silicon spatial light modulator (LCOS-SLM). A phase-only SLM was used which can control lights in two dimensions, and capable of modulating the phase of the reflected light creating the on-demand array of the beam pattern of the incident laser beam. Each beam of the beam array can generate one microrobot while focused at the light absorbing layer of the substrate (Fig. 2.3). The experimental setup, methodology, and control mechanism has been discussed in the following sections.

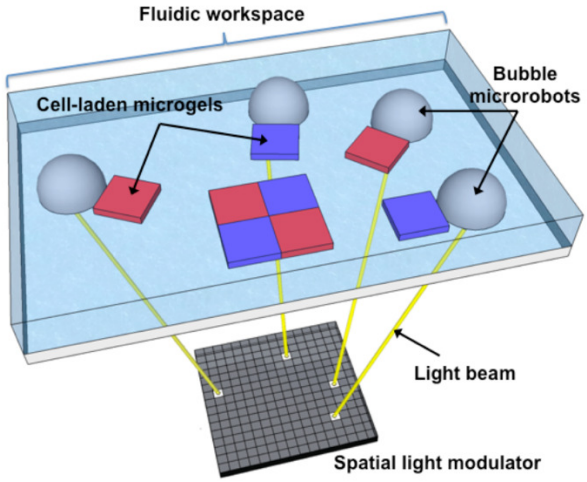

Figure. 2.3 Cartoon drawing of the multiple OFB microrobot generation system. A spatial light modulator is used to pattern the incident laser beam (not shown). Each beam of the light array is capable of generating and actuating one microrobot, which can be used to assemble objects such as cell-laden hydrogels.

2.4 Experimental Setup and Holographic Control System

2.4.1 Experimental Setup

Fig. 2.4 shows the initial optical setup of the OFB microrobot system. The setup has been redesigned to improve the optical efficiency at a later stage of research. A 1064-nm single TEM00 mode, linearly polarized laser (Laser Quantum, Ventus 1064, 1.5+ W) was collimated using a camera lens onto a SLM (Hamamatsu, LCOS-SLM X10468-07) with an effective area of 16 by 12 mm. An 800 pixel by 600-pixel computer-generated hologram (CGH) was created using a

modified version of the Red Tweezers program, licensed under the GNU General Public License, and developed by Dr. Richard Bowman's research group [105]. The SLM outputs the holographic pattern set by the control interface Red Tweezers. The patterned light from the SLM was collimated by achromatic doublets and focused by a 0.42-N.A. 20X objective lens (Mitutoyo) onto the absorbing layer of the substrate. This absorbing layer consists of indium tin oxide (ITO) that is 100 nm in thickness, topped with a layer of 1-μm-thick amorphous silicon (α-Si). The absorbing layer converts the light energy into heat. A fluidic chamber was formed over the absorbing layer by bonding a 1 mm thick glass slide over the substrate with 300-μm-thick spacers. Silicone oil (Fisher Scientific, S159-500) was used in the fluidic chamber.

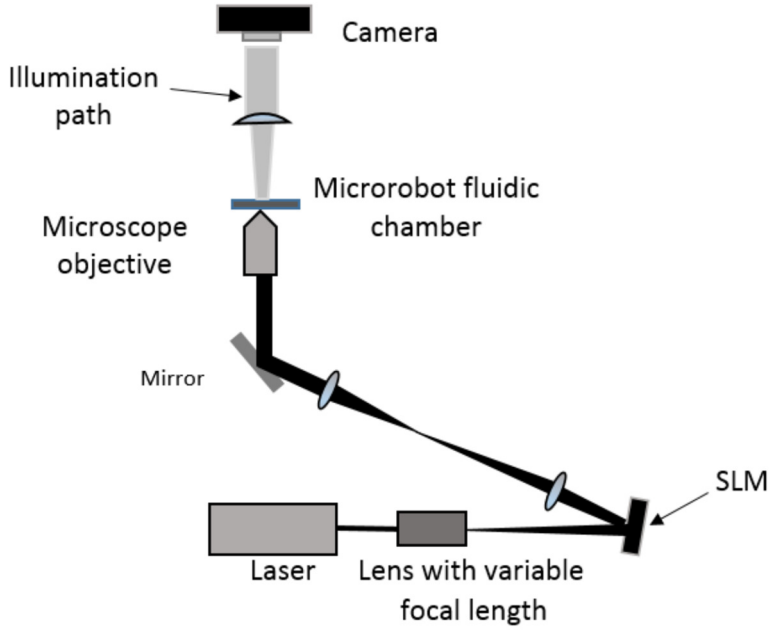

Figure. 2.4 Optical setup for the actuation of multiple OFB microrobots using computer-generated holograms. A collimated TEM00 laser beam was projected through a variable focal length lens to enlarge the beam size. The SLM displays a hologram that reflects multiple beams into the objective lens to create multiple OFB microrobots in the fluidic chamber.

The laser used in the setup has a beam diameter of 1.85 ± 0.2 mm, and is expanded using an adjustable focus lens with a magnification of 6X. The expanded beam is incident on the SLM, which is capable of shaping the beam by adjusting its phase. The incident laser beam can thus be shaped into an array of multiple output beams [101]. The total laser power measured on the substrate was 330 mW.

The maximum laser power available for microrobot actuation was limited by the laser output power and by losses from the optical components, as they were not optimized for IR wavelengths. In addition, the degree of collimation was significantly affected by magnification using a variable-focal-length lens (Fig. 2.4). In this setup, a 4-*f* lens configuration was used for reducing the aberration and for collimating the reflected beam. However, the optical set-up experienced spatial optical noises. In a later experiment, the set-up was redesigned by replacing the variable-focal-length lens with 3x beam expander. The 4-*f* imaging was also removed as the reflected beam from the SLM was already collimated. Figure 2.5 shows the revised experiment setup, which increased the optical efficiency.

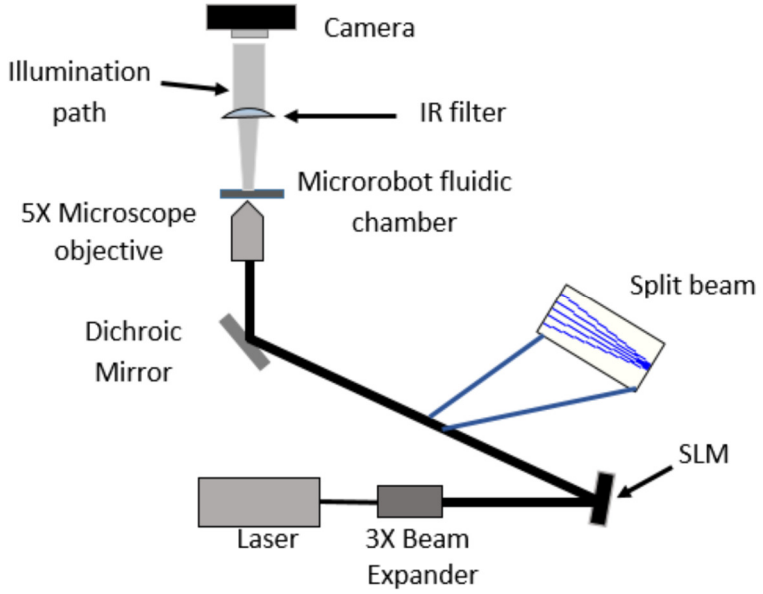

Figure. 2.5 Redesigned experimental setup for the actuation of multiple OFB microrobots.

2.4.2 Computer Generated Holographic Control System

Using light to control the microrobot actuation force enables on-the-fly configurability of multiple OFB microrobots. This is made possible by using a SLM to display holograms that shape a single laser beam into complex optical patterns used to independently address each microrobot. The SLM was controlled using a modified version of Red Tweezers, an open-source software for the control of holographic optical tweezers created with LabVIEW (National Instruments) that renders holograms using the OpenGL Shading language [105]. Red Tweezers was modified for the

requirements of OFB microrobot actuation; a bubble-collision avoidance function was added [29], as the OFB microrobots can be susceptible to merging if they contact each other. Another feature added to Red Tweezers was a sequence generator, a function used for creating sequences of holograms to control the motions of individual microrobots. This feature helped to enable the independent control of many microrobots in parallel. The bubble-collision avoidance function and the sequence generator is discussed later in this chapter. Control of the optical pattern enables control of the OFB microrobots. A focused point of light on the substrate is represented by a circular spot on the user interface of the control software (Fig. 2.6a, d, g). The coordinates of the laser focal points are sent to the OpenGL shader hologram engine,

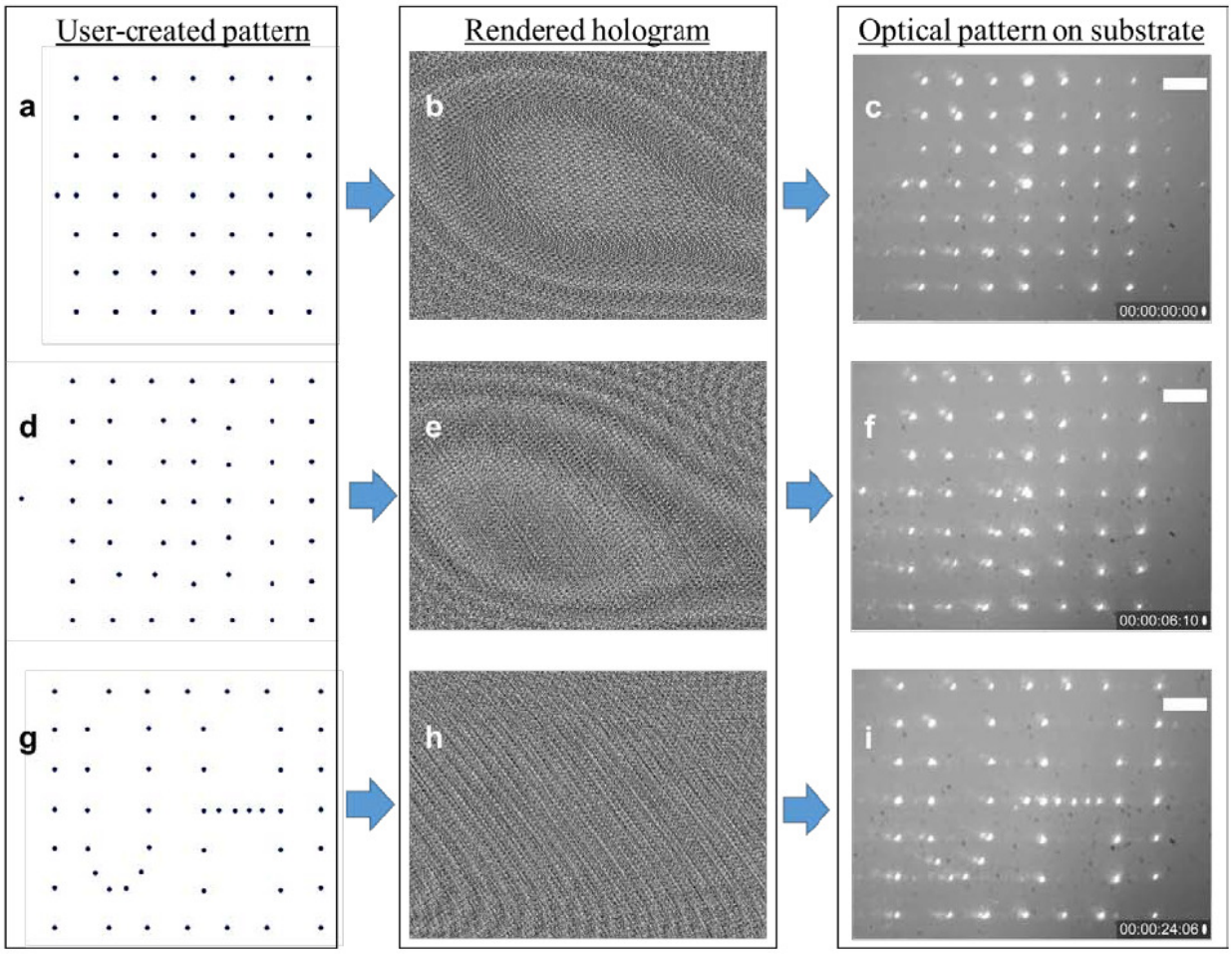

Figure. 2.6 Pattern of 50 optical spots automatically controlled to create the letter "UH." (a) Image of the user interface in LabView, including the pattern sequence. (b) The corresponding hologram rendered by Red Tweezers. (c) The SLM output of 50 spots on the substrate. The pattern on the user interface (d), the corresponding hologram (e), and the spot pattern on the substrate 6 seconds after the initiation of the automatic control sequence. The pattern on

the user interface (g), corresponding hologram (h), and the optical spot pattern on the substrate at the end of the control sequence (i) The pattern forms the letters "UH." The scale bar displayed on (c), (f), (i) is 100 μm.

which calculates the corresponding hologram using the direct superposition algorithm, and displays the hologram on the SLM (Fig. 2.6b, e, h). This computer-generated hologram controls the phase of the incident wavefront, creating the light pattern defined in the user interface (Fig. 2.6c,f,i). The reflected phase-modulated wavefront from the SLM was imaged on the substrate using 4-*f* imaging. The optical spot visible at the center of Fig. 2.6i is the zero-order spot, which was not defined in the user interface, and is an undesirable effect of using the SLM to create the optical pattern. The intensity of the zero-order beam spot is greater when the laser is shaped into an array of only few beams. Thus, for the case presented here, where the laser beam is shaped into an array of 50 spots, the effect of the zero-order spot on microrobot actuation was insignificant.

2.4.2.1 Bubble Collision Avoidance System

As mentioned above, the Red Tweezers program allows the user to create a sequence of holograms to be displayed on the SLM. The program, was created using LabView (National Instruments) and designed for optical tweezer applications. However, Red Tweezers can be used to generate the holograms needed for OFB microrobot actuation, thus controlling the location of each microrobot. In Red Tweezers, each optical trap location is identified by a numerical value assigned by the program. Using either a mouse or the coordinate system provided by the interface, the program is able to control multiple optical traps at once. Some modifications were made to the Red Tweezers program to customize it for OFB microrobot control. This included implementing a collision-avoidance function. If the OFB microrobots come into contact, it is possible that the OFB microrobots will merge into one larger bubble. This can be avoided with the collision-avoidance function, which creates a buffer zone around each optical spot that prevents them from moving too close to one another. When a spot is moved using the mouse, the program calculates the distance, *d*, between the selected spot and all other spots, according to

$$d = \sqrt{(x_1 - x_2)^2 + (y_1 - y_2)^2} \tag{2.6}$$

where x_1 and y_1 are the *x*- and *y*-coordinates of the selected spot, and x_2 and y_2 are the *x*- and *y*-coordinates of another spot.

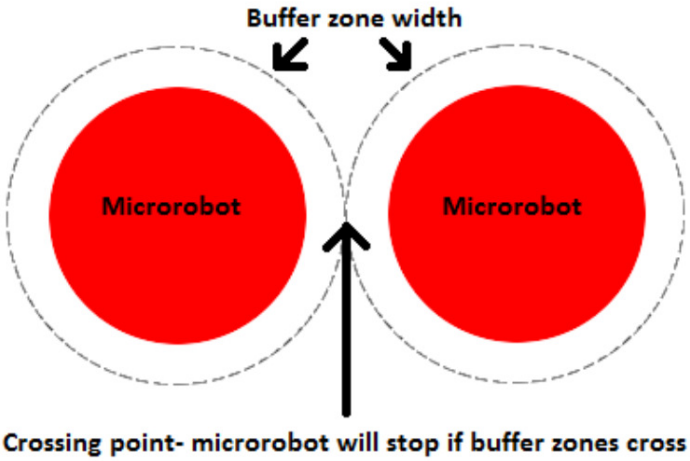

Figure. 2.7 Visual example of the buffer zone. If the buffer zones (dashed lines) surrounding two microrobots (red circles) intersect when a microrobot is moved by the user, then the microrobot will automatically stop. It will only move again if the user moves the microrobot away from the other nearby microrobot.

If this distance is small enough such that the selected spot crosses the buffer zone of the other spot (*d* is less than two times the buffer zone width), the spot stops, and the user is unable to move it (Fig. 2.7). The spot would only be able to change position if the next movement increases *d*. If multiple spots were selected, each selected spot would check its distance between all other spots. The first spot that is detected to have crossed a buffer zone will stop the movement for all selected spots. A future iteration of this function will expand the collision avoidance for coordinate-based movements, as when the user enters *xyz* coordinates for each spot rather than using the mouse.

2.4.2.2 Sequence Generator

To automatically control the OFB microrobots, a sequence generator was created. This function runs in a separate LabView program, and stores the positions of the spots from the Red Tweezers interface in a two-dimensional array. The user creates this array by first declaring the maximum number of microrobots in the sequence and the number of frames in the sequence. Each array cell includes various parameters that can be edited, including the position and intensity of each optical spot. If needed, additional frames can be added to the created sequence. The user then declares the position of the spot in each sequence frame on the Red Tweezers interface. Once a frame is completed, it is saved using the "Save State" button. The frame is then saved to the value that "Sequence Order" points to, starting at sequence frame 0. To verify it has been saved, the user is able to view the coordinates of each microrobot by controlling the "Sequence Storer" array, the

two-dimensional array that stores the coordinates for each frame. The first dimension controls the order of the sequence, while the second shows the ID number of the microrobot that is being displayed. Once the sequence is created, Red Tweezers can play the sequence at a constant frame rate, and the appropriate holograms are sent to the SLM. The frame rate can be adjusted, and the playback of the sequence can also be controlled manually. Each frame of a sequence can also be edited, and stored back into the array.

2.5 Independent Actuation of Twelve and Twenty-Four Microrobots in Parallel

Using the experimental setup of Fig. 2.4 and 2.5 twelve and twenty-four microrobots were actuated independently in parallel Using the holographic OFB actuation system. The aberrations of the optical setup were corrected using the same correction factors as a similar optical setup [106].

2.5.1 Results

The array of beam spots was used to generate 12 OFB microrobots in the fluidic chamber. Each beam spot generated one OFB microrobot each. These microrobots were maneuvered over an area of 528 µm by 360 µm. A rectangular pattern of the 12 OFB microrobots was created and actuated

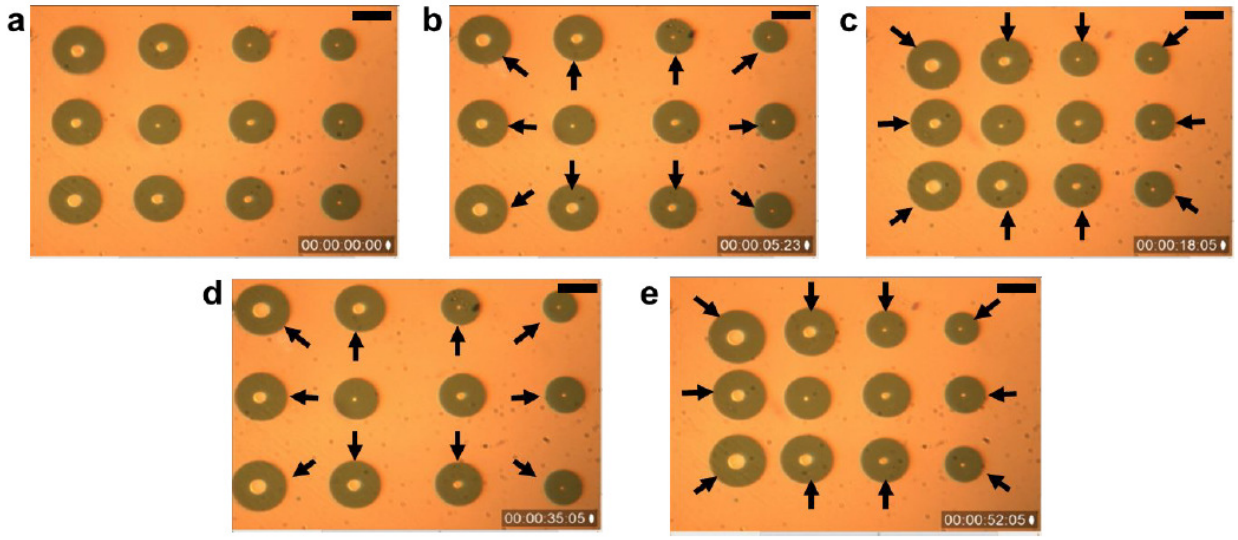

Figure. 2.8 Actuation and control of 12 OFB microrobots. (a) The OFB microrobots in their initial positions. (b) The microrobots were maneuvered radially outward. (c) The microrobots were then maneuvered radially inward. (d, e) The outward and inward microrobot motion was repeated. These maneuvers demonstrate movement of the microrobots in different directions at the same time. The scale displayed on these images is 50 µm.

using the sequence generator described in the previous section (Fig. 2.8). The microrobots had an average diameter of 64 μm and were simultaneously maneuvered in various directions to demonstrate the multidirectional independent movement of each microrobot. The initial OFB microrobot array occupied an area of 443 μm by 277 μm (Fig. 2.8a). Each microrobot was automatically controlled to move radially outward to create a larger rectangular pattern with an area of 500 μm by 320 μm (Fig. 2.8b). The microrobots then moved inward, resizing the rectangular pattern to an area of 397 μm by 240 μm (Fig. 2.8c). This operation was then repeated (Fig. 2.8d, e). The entire automated sequence took 52 seconds to complete, and the average velocity of each microrobot was approximately 5 $\mu m.s^{-1}$.

Using the holographic OFB actuation system, a pattern of 50 optical spots were generated and automatically controlled to create a pattern resembling the letters "UH." The patterns were created using Red Tweezers and the sequence generator to produce 50 spots in a square matrix (Fig. 2.6). Due to the limited laser power in each spot, OFB microrobots could not be generated using all 50 spots. However, this sequence is able to demonstrate the potential for the automatic control parallel of many OFB microrobots. Each spot can be repositioned individually or as part of a group in a set workspace. Each spot can move with a specific trajectory during the sequence, whether it is a part of a group or not. Provided that there is enough power directed to the substrate, 50 OFB microrobots can be controlled by the system at one time.

At a later stage the experimental setup was changed to Fig. 2.5, where twenty-four bubble microrobots were optothermally actuated in parallel. The bubble microrobots were independently controlled by a computer-generated holographic (CGH) control system. This work demonstrated the actuation of many microrobots that are capable of performing an assigned task such as microassembly with increased throughput. A working fluidic chamber was formed for this experiment over the absorbing layer of the substrate by bonding a 1-mm thick glass slide to the absorbing substrate using 80-μm-thick spacers (Fig. 2.1). Fluorinated oil (3M Fluorinert FC-40) was used as working fluid in the fluidic chamber. The output light pattern of the SLM consists of an array of 24 beams focused on the absorbing layer of the substrate. The SLM shapes the wavefront of the Gaussian beam of the laser by changing the spatial distribution of phase of the light without varying the amplitude. Each of the beams in the array has the same relative intensity,

so the total power of the laser on the substrate was equally divided among all the beams. Each of the beams focused on the absorbing layer created localized hot spots in working fluid. The layers of α-Si and ITO absorb 73% [107] and 20% [108] of the incident laser light, respectively. The localized hot spots created on the absorbing layer can vaporize the FC-40, creating gas bubbles that form the OFB microrobots. Subsequently, OFB microrobot actuation was achieved by moving the corresponding light beam in the desired direction, using the holographic SLM system described in Sec. 2.4. Each beam of the desired light pattern used to actuate the OFB microrobots is represented a by circle in the user interface of the control software (Fig 2.9a). The hologram engine calculates the corresponding hologram and displays it on the SLM (Fig. 2.9b). The SLM reflects the beam intensity pattern, which was focused and imaged on the substrate (Fig. 2.9c), producing the desired beam pattern.

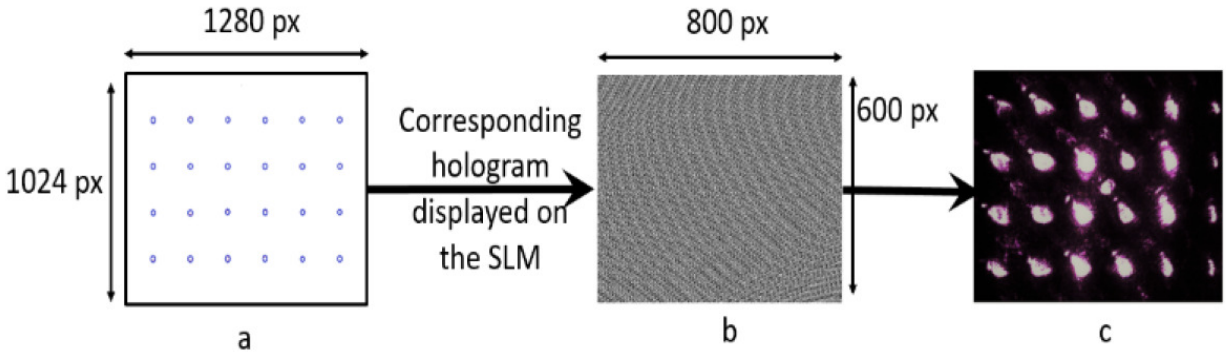

Figure 2.9. Holographic optical pattern control software. (a) A rectangular array of 24 circular spots was created in the user interface, in a workspace area of 1280 px by 1024 px. (b) The x-y coordinates of the spots were sent to the OpenGL shader which rendered the corresponding hologram on the SLM. The hologram size is 800 px by 600 px. (c) The SLM reflects the phase-modulated wavefront, shaping and making an array of the laser beam according to the user-defined light pattern. This image shows a photo of the light pattern on the substrate.

Previously, we achieved the parallel actuation of 12 OFB microrobots [109]; the number of microrobots was limited by the amount of laser power available at the substrate. This earlier experimental setup used a 4-*f* imaging system for collimation. The current setup replaced these components with a 3X beam expander, resulting in a more planar wavefront incident on the SLM. This helped to maintain the collimation after modulation by the SLM, enabling the removal of the 4-*f* imaging lenses, resulting in an additional 20 mW of laser power at the substrate. A laser intensity of approximately 113 $W.cm^{-2}$ of laser was necessary to create a bubble microrobot; this

was done by heating the liquid medium to its boiling point. However, an intensity of only 24.5 $W.cm^{-2}$ was sufficient for OFB actuation. In the experimental setup used for these results, a total of 195 mW of laser power was available on the substrate. This allows the incident laser beam to make an array of 24 beams, corresponding to an intensity of approximately 30 $W.cm^{-2}$ per beam, which is sufficient for OFB microrobot actuation. However, there is insufficient laser intensity for the creation of an OFB microrobot using these 30-$W.cm^{-2}$ beams. Therefore, each bubble was created by increasing the intensity of one specific beam, at the expense of reducing the intensity in all the other beams. This higher intensity beam is only activated to create the OFB microrobots; during microrobot actuation, all the beams have the same intensity of 30 $W.cm^{-2}$.

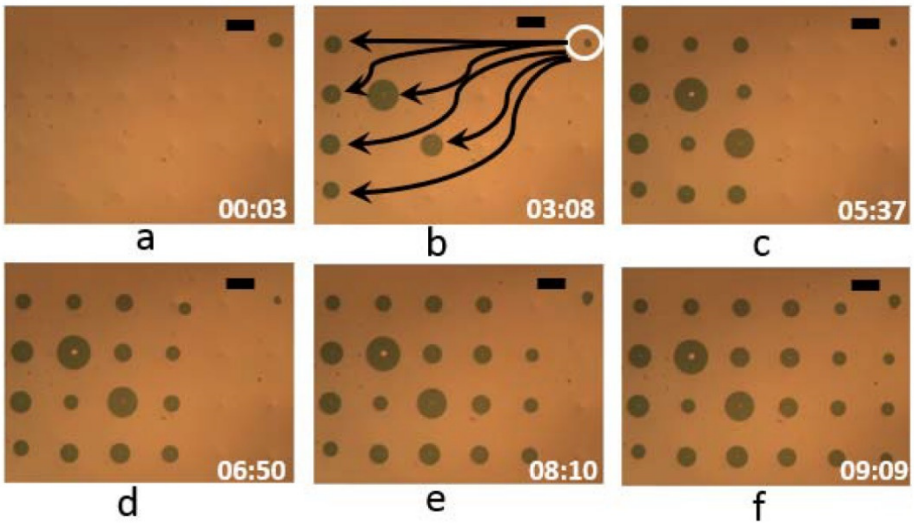

Figure 2.10 Actuation of 24 OFB microrobots. (a) The first bubble was created using beam intensity of 113 $W.cm^{-2}$, focused at a point near the top right of this image. (b) From the bubble-creation position (indicated by the white circle), the OFB microrobots are actuated to specific locations, as indicated by the arrows. At these positions, other laser beams are used to hold the microrobots in place. (c.d.e,f) Subsequent creation of 12, 16, 19, and 24 OFB microrobots, and actuation to their respective locations. Scale bar: 100 μm.

Figure 4 shows the actuation of 24 OFB microrobots in a 1578 μm by 1180 μm workspace. Figure 2.10(a) shows the creation of a microrobot. To create each OFB microrobot, the intensity of the laser beam was momentarily increased to approximately 113 $W.cm^{-2}$ at a specific location on the substrate (Fig. 2.10b). The same nucleation location was used to generate all of the microrobots of the array. The generated microrobots had an average radius of 45 μm. Immediately after the OFB microrobot was created, the beam intensity was reduced to 30 $W.cm^{-2}$, and the light beam was used to transport the microrobot to another position on the substrate. When the microrobot reached

its new position, another 30-W.cm^{-2} laser beam was used to stably hold the microrobot in place. This process was repeated until 24 microrobots were created and placed at specific positions. The total process shown in Figure 2.10 took approximately 9 minutes.

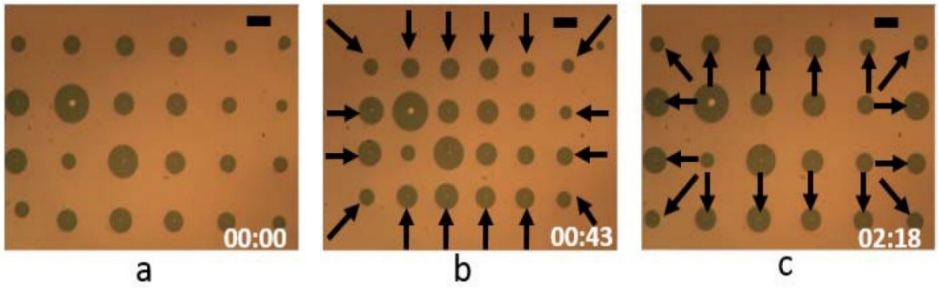

Figure 2.11 Independent maneuvering of 24 OFB microrobots. (a) Initial positions of the microrobots. (b) The matrix pattern of the microrobots was contracted. (c) The matrix pattern was expanded, demonstrating independent manipulation of each microrobot. Scale bar: 100 μm.

Figure 2.11(a) shows the microrobot matrix, initially covering an area of 1206 μm by 748 μm. The matrix was contracted (Fig. 2.11b) and expanded (Fig. 2.11c) to demonstrate independent, multidirectional maneuvering of each microrobot. The microrobots were maneuvered at an average velocity of 6 μm.s-1. In the future, by improving the fill factor over the entire working area of the SLM, even larger numbers of microrobots can be actuated and maneuvered in a macroscale area with microscale precision.

2.5.2 Discussion

The number of microrobots generated in a given setup is limited by the laser power available on the substrate, the size of the modulated wavefront reflected from the SLM, and the input aperture of the objective lens. The SLM has an effective area of 16 mm by 12 mm, and can thus modulate a 12-mm-diameter circular beam. If the maximum beam diameter of 12 mm is used, the number, size, and resolution of the microrobots will be limited by the pixel size of the SLM. The SLM used here is 800 px by 600 px over a 16 mm by 12 mm area, so a beam with a diameter of 12 mm can be shaped into and array of approximately 70,000 beams, assuming each beam has a diameter of 20 μm, and there is an edge-to-edge spacing of 20 μm between beams. However, it is hard to realize this many individual beams in a practical setup, due to limitations of the other optical components. The focusing of the reflected wavefront requires the use of objective lenses. Higher magnification lenses have smaller entrance pupils. As an example, a 10x long-working-distance

objective lens has an entrance pupil of 12 mm, whereas a 20x lens has an entrance pupil of 9 mm. Thus, a 20x objective lens provides tighter focusing of individual beam spots, at the cost of a reduced entrance pupil. The smaller entrance pupil reduces the wavefront size, creating a smaller working area on the substrate. The total laser power available on the substrate also depends on the working area on the substrate. A larger working area requires a larger wavefront at the entrance pupil of the objective lens. However, if the wavefront size is bigger than the entry pupil, the wavefront is clipped, resulting in less power available on the substrate.

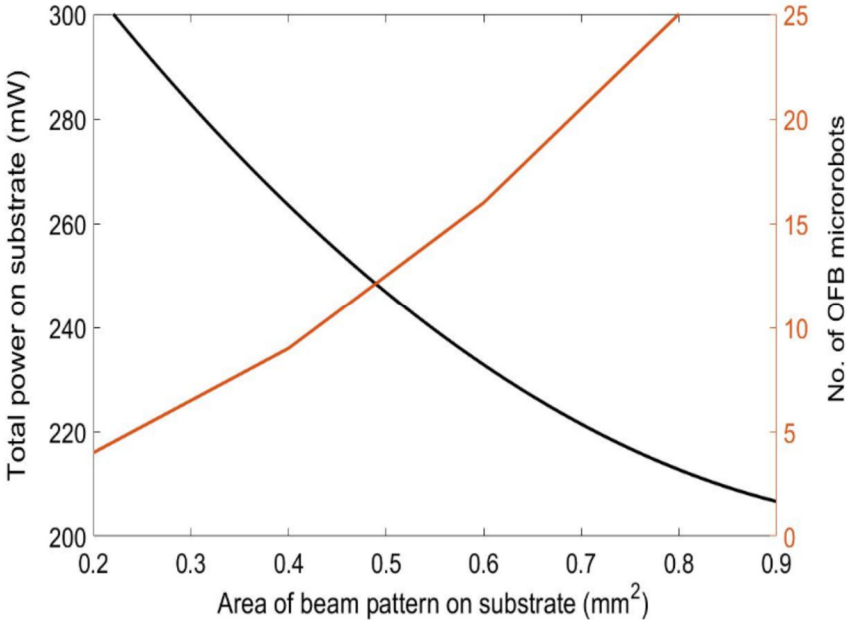

Figure 2.12. Total laser power available and number of microrobots actuated on the substrate. Here, the laser power available is plotted with corresponding number of microrobots that can be actuated as a function of the optical pattern area. This data is specific to the experimental setup used in this work (Fig. 2.5). The curves are quadratic fits to the measured data points.

The laser power on the substrate and number of OFB microrobots that can be controlled are plotted as a function of the optical pattern size (Fig. 2.12), for the specific experimental setup used here. The microrobots were assumed to have radii of 50 μm with and edge-to-edge spacing of 100 μm. The power distribution was assumed to be 8 mW/ beam for actuation and 30 mW in one laser beam for generating the OFB microrobots. Figure 6 shows that up to 25 microrobots can be generated and controlled over an area of approximately 0.8 mm, provided 300 mW of laser power is available in the modulated wavefront. In this experiment, one laser beam was used to serially generate the

microrobots at a specific point, then each microrobot was transferred to its respective actuating beam. When the intensity of the generating beam was increased, the power of the other laser beams (the actuating beams) was decreased. This had a significant effect when the actuating beams were controlling OFB microrobots. Since the generating beam had five times higher power than the actuating beams, a strong thermocapillary flow occurred during nucleation, and adjacent microrobots could be pulled towards the nucleation point if their actuating beam intensities are not strong enough to hold the microrobots in place. This issue was mitigated by using a short duration (2 seconds) for the generating beam. To further minimize the effect of the generating beam, all actuating beams were given higher beam intensities compared to previous configurations that used fewer microrobots in the workspace [28, 110]. By giving higher intensities to the actuating beams, the microrobots will be more stably trapped. In addition, each microrobot was generated as far as possible from the existing microrobots within the workspace. Keeping the nucleation point farther from the actuating beams reduces the possibility of having a generated bubble merge with an existing bubble.

2.6 Conclusion

In this chapter, the actuation mechanism of single and multiple microrobots has been discussed along with different experimental setups used for reducing the optical error and optimizing the optical efficiency. The OFB microrobot control software, a computer-generated holographic control system developed in LabVIEW, is also discussed. Finally, the independent actuation of 12 and 24 OFB microrobots was demonstrated in parallel, with potential to actuate up to 50 OFB microrobots. Increasing the light intensity can increase the maximum microrobot speed from 5 $\mu m.sec^{-1}$. to 475 $\mu m.sec^{-1}$ [1, 92, 109]. The intensity of each spot was relative to the total laser power available on the substrate. The microrobot actuation velocity increased with the higher spot intensities. However, at optical intensities over 10 $kW.cm^{-2}$ per optical spot, the radius of the microrobot can increase to over 150 μm. This increase in size resulted in a lower velocity, as larger microrobots experienced higher friction with the surface.

The next chapter shows the independent actuation of 50 OFB microrobots along with the co-operative micromanipulation of various micro-objects in the liquid medium using single, pairs, and multiple microrobots independently in parallel.

CHAPTER. 3 COOPERATIVE MICROMANIPULATION USING THE INDEPENDENT ACTUATION OF MANY MICROROBOTS IN PARALLEL

As mentioned in Chapter 1, the control of sub-millimeter objects has a significant role in many disciplines, including physics, chemistry, material science, biology, engineering, and medical research. Untethered sub-millimeter robots are capable of micro-object manipulation, and have promising applications in targeted therapy [111], disease diagnoses [112], single-cell manipulation [79, 113], tissue engineering [79, 114], and cell surgery [31, 79]. The independent control of multiple microrobots is useful for increasing the throughput of micro-object manipulation, or for enabling cooperative manipulation.

In this chapter, the independent actuation of 50 opto-thermocapillary flow-addressed bubble (OFB) microrobots in parallel is demonstrated. Individual microrobots and groups of microrobots were moved along linear, circular, and arbitrary 2D trajectories. The independent addressing of many microrobots enables higher-throughput microassembly of micro-objects, and cooperative manipulation using multiple microrobots. Demonstrations of manipulation with multiple OFB microrobots include the transportation of microstructures using a pair or team of microrobots, and the cooperative manipulation of multiple micro-objects. The results presented here represent an order of magnitude increase in the number of independently actuated microrobots in parallel as compared to other magnetically or electrostatically actuated microrobots, and a factor of two increase as compared to previous demonstrations of OFB microrobots.

3.1 Methods and Experiment Setup

Previously, up to 24 OFB microrobots were generated and independently actuated on a glass substrate coated with amorphous silicon [92]. This chapter presents the independent actuation of 50 microrobots in parallel on a titanium-coated glass slide. The microrobots were simultaneously maneuvered in different directions to demonstrate uncoupled parallel actuation. The multidirectional maneuverability of the microrobots along various trajectories was demonstrated, and provided the flexibility needed to manipulate micro-objects into various orientations. The independent actuation of multiple OFB microrobots enables cooperative micromanipulation, and

enhances the assembly capabilities of this microrobot system. Multiple OFB microrobots working together are capable of exerting more force on microstructures. In addition, cooperative micromanipulation by a team of OFB microrobots was used to simultaneously transport multiple micro-objects in less time compared to manipulation using a single microrobot.

Figure 3.1b shows the optical setup used for creating and actuating fifty OFB microrobots. The light source was a 1064-nm single-mode (TEM_{00}) linearly polarized laser (Laser Quantum, Ventus 1064, 1.5 + W). The 3.3-mm-diameter beam from the laser was incident on the 3.3 mm-diameter input pupil of a 3X beam expander, resulting in an approximately 10-mm-diameter collimated beam. The collimated beam was incident on a spatial light modulator (SLM) from Hamamatsu (LCOS-SLM X10468–07). This SLM alters the phase of the incident beam, and has an effective area of 16 mm by 12 mm. In this experiment, the SLM was used to shape the wavefront of a single input laser beam into the optical patterns used to actuate multiple OFB microrobots. The phase-modulated wavefront from the SLM was 4-*f* imaged (focal length *L1* = 100 mm, focal length *L2* = 50 mm) on the back focal plane of a long-working-distance 10x objective lens (Mitutoyo, 0.28 N.A.), which focused the light onto the absorbing layer of the substrate. The substrate was a glass microscope slide coated with 50 nm of titanium, and formed the floor of the fluidic chamber for the OFB microrobots.

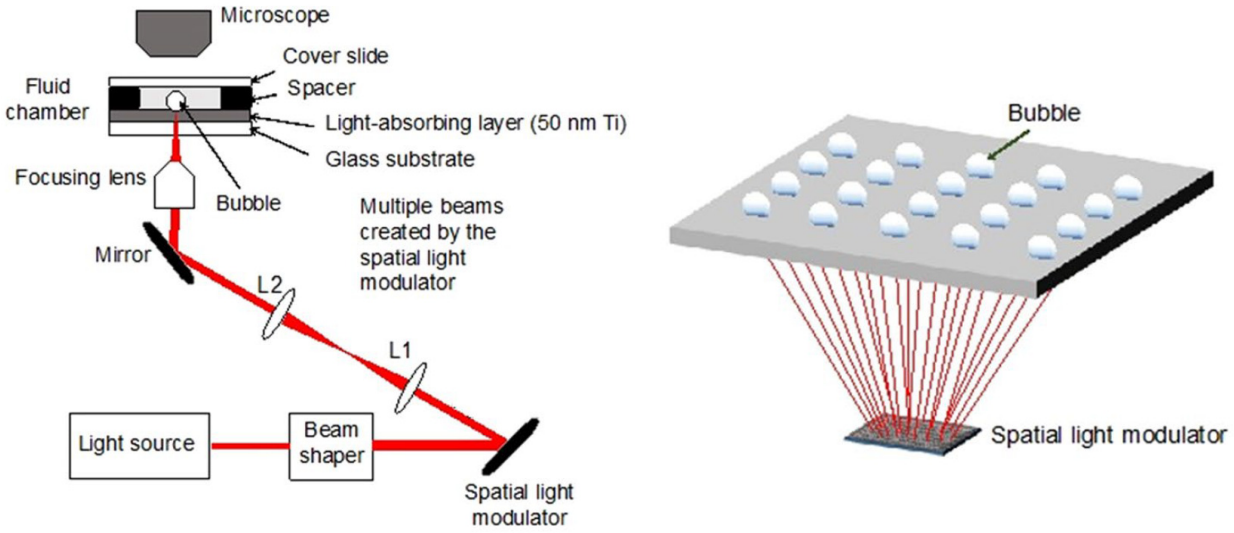

(a) (b)

Figure. 3.1. Setup and methodology for multiple opto-thermocapillary flow-addressed bubble (OFB) microrobots. (**a**) Experimental setup for the OFB microrobot system. (**b**) A simplified schematic showing that a single

laser beam can be shaped using a spatial light modulator, creating dynamic optical patterns that enable the simultaneous control of multiple OFB microrobots.

A fluidic chamber was established on the substrate using 500-μm spacer consisting of double-sided polyimide tape between a glass microscope slide and the titanium-coated glass slide. Silicone oil (Fisher Scientific, S159–500) was used as the working medium in the fluidic chamber. The wavefront of the single laser beam was shaped into 50 beams focused on the absorbing layer of the substrate by a programmable spatial light modulator (SLM), creating the necessary hot spots for microrobot generation (Fig. 3.1c).

3.2 Microrobot Control Using Computer-generated Holograms

Using light to control the microrobot actuation force enables on-the-fly configurability of multiple OFB microrobots. This is made possible by using a SLM to display holograms that shape a single laser beam into complex optical patterns used to independently address each microrobot. The SLM was controlled using a modified version of Red Tweezers, an open-source software for the control of holographic optical tweezers created with LabVIEW (National Instruments) that renders holograms using the OpenGL Shading language [105]. Red Tweezers was modified for the requirements of OFB microrobot actuation; these modifications have been detailed in Chapter 2. Control of the optical pattern enables control of the OFB microrobots. A focused point of light on the substrate is represented by a circular spot on the user interface of the control software (Fig. 3.2a). The coordinates of the laser focal points are sent to the OpenGL Shader hologram engine, which calculates the corresponding hologram using the direct superposition algorithm and displays the hologram on the SLM (Fig. 3.2b). This computer-generated hologram controls the phase of the incident wavefront, creating the light pattern defined in the user interface (Fig. 3.2c). The reflected phase-modulated wavefront from the SLM was imaged on the substrate using 4-*f* imaging. The optical spot visible at the center of Fig. 3.2c is the zero-order spot, which was not defined in the user interface, and is an undesirable effect of using the SLM to create the optical pattern. The intensity of the zero-order beam spot is greater when the laser is shaped into only a few spots. Thus, for the case presented here, where the laser beam is shaped into 50 spots, the effect of the zero-order spot on microrobot actuation was insignificant.

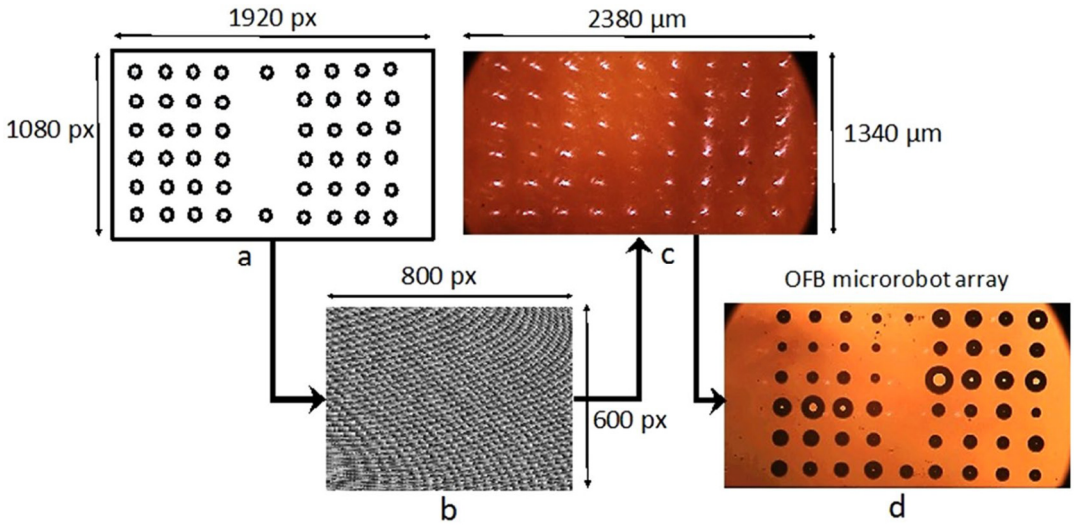

Figure. 3.2 User-defined OFB microrobot control pattern generation. (**a**) A pattern of 50 focused laser spots for the control of 50 OFB microrobots created by the user. (**b**) The corresponding hologram used to create the optical pattern from a single input laser is generated and displayed on the spatial light modulator. (**c**) The optical pattern as viewed through the microscope. (**d**) Fifty OFB microrobots controlled using the optical pattern.

3.3 OFB Microrobot Generation and Actuation

OFB microrobots can be generated on demand within the fluidic chamber, making it simple to create and control multiple microrobots. An OFB microrobot can be nucleated by momentarily increasing the optical power of a single laser focal point to a level sufficient to vaporize a small volume of the liquid medium. The power of the nucleating laser beam was reduced as soon as the bubble was created, to avoid an increase in the bubble size. The laser intensity used for bubble nucleation was five to six times higher than the intensity used for actuation, and is quantified later in this section. There are two primary considerations for nucleating and actuating OFB microrobots. The first is sufficient optical intensity; nucleation requires higher intensity than actuation. Strong light absorbance by the substrate helps to convert the incident optical energy into thermal energy. Another consideration is the degree of localization of the optical and thermal energy, which depends upon the optical elements in the experimental setup and the thermal conductivity of the absorbing material. Generally, a higher intensity of the optical beam and a lower thermal conductivity of the light-absorbing material is desirable for creating microscale hot spots.

In Chapter 2, 24 OFB microrobots were independently actuated [92], but the number of microrobots was limited by the available laser power and its conversion to a thermal gradient. The degree of parallelization in a multiple OFB microrobot system is proportional to the conversion of optical power to localized hot spots on the substrate, which is dependent on the laser intensity at the substrate and the efficiency of the conversion of light into heat. Increasing the laser intensity can compensate for losses in the optical elements or low optical absorption by the substrate, but this will increase the cost of the laser. Thus, for the system described here, the laser output power was regarded as a fixed quantity. Instead, to increase the number of OFB microrobots that could be actuated in parallel, the substrate material was changed: a titanium (Ti)-coated substrate [115] replaced the amorphous-silicon (α-Si)-coated substrate used in previous work [28]. The absorbing substrate used in previous microrobot experiments consisted of a 1-mm-thick glass slide coated with 100-nm-thick layer of indium tin oxide (ITO) and 1-μm-thick layer of α-Si [92].

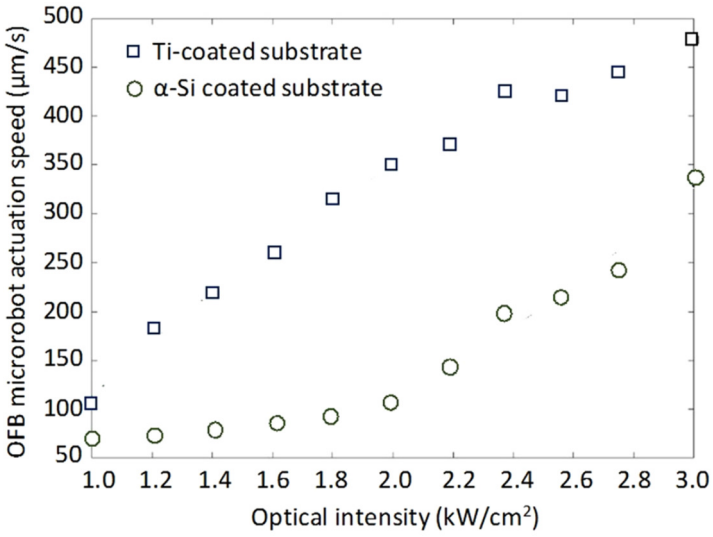

Figure. 3.3 OFB microrobot actuation velocity on different substrates. The maximum OFB microrobot actuation speed for various intensities of the actuating laser beam is higher on substrates coated with 50 nm of titanium (Ti) as compared to substrates coated with 1 μm of amorphous silicon (α-Si). The size of OFB microrobots was kept constant during these measurements.

The Ti-coated substrate absorbs 16% more light than the α-Si-coated substrate, as measured using an optical power meter (Newport 1830C). This translated into a higher OFB microrobot actuation velocity compared to an α-Si-coated substrate (Fig. 3.2). However, optical intensities above 2 $kW.cm^{-2}$ resulted in growth of the bubble size, which is not desirable during OFB microrobot actuation (Fig. 3.4).

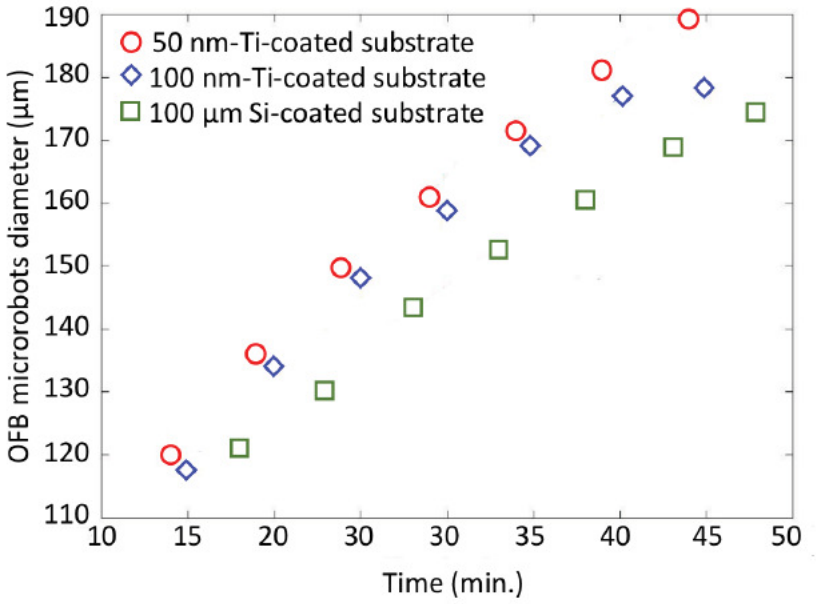

Figure. 3.4 OFB microrobot generation on different substrates. The average diameter of OFB microrobots over time on different substrates. The diameters are an average of a regularly spaced array of 24 microrobots over the 2380 µm by 1339 µm working area.

To avoid unwanted bubble growth, the optical intensity of this system was kept near 1.35 kW.cm^{-2} during actuation, although the bubbles still increased in size at an average rate of 0.5 µm.min^{-1} due to the continuous laser illumination. The microrobot size depends on the laser intensity and the duration of illumination [116]. Reducing the size of an OFB microrobot can be achieved by setting the actuating optical intensity to zero (Fig. 3.5) which can be utilized to control the bubble size. At an optical intensity of 1.35 kW.cm^{-2}, the Ti-coated substrate results in approximately 25% faster actuation speeds compared to the α-Si-coated substrate. Previously, 24 OFB microrobots were generated on an α-Si-coated substrate with a total laser power of 195 mW, resulting in 8.1 mW for each optical spot. In this work, 50 OFB microrobots were generated on a Ti-coated substrate, with a laser power of 330 mW, resulting in 6.6 mW for each optical spot. The minimum power required for bubble actuation on the α-Si-coated substrate was 23% higher than the power needed to actuate the same size bubble on a Ti-coated substrate. This suggests that 23% more OFB microrobots can be generated on a Ti-coated substrate. In addition to the amount of light absorbed by the substrate, the actuation speed is also affected by the thermal gradient of the localized hot spot. A higher thermal gradient results in stronger thermocapillary effects and faster

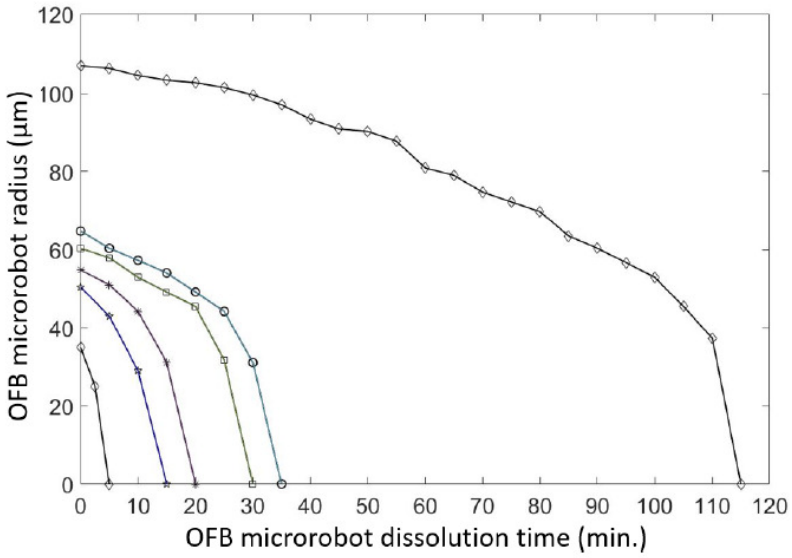

Figure. 3.5 Dissolution rates of OFB microrobots in silicone oil. Different sizes of OFB microrobots dissolve in silicone oil at varying rates once the actuating laser power is set to zero. Microrobots with radii of 50 μm or larger take significant time to dissolve completely. When the microrobot radius is close to 25 μm, the microrobot dissolves within four minutes. The minimum and maximum average rate of decrease in radius for 108 μm-radii and 35 μm-radii OFB microrobots is approximately 0.93 $\mu m \cdot min^{-1}$ and 7 $\mu m \cdot min^{-1}$, respectively.

OFB microrobot actuation. The thermal gradient on Ti- and α-Si-coated glass substrates was measured by filling the fluid chamber with 1% poly(*N*-isopropyl acrylamide (PNIPAAm) in phosphate-buffered saline (PBS) solution. The PNIPAAm becomes insoluble in water when the temperature exceeds 32 °C ref. [117], creating a noticeable gel under optical microscopy [31]. The laser beam was focused on the absorbing layer of the fluid chamber, in the same setup shown in Fig. 3.1, and the laser power was gradually increased until an OFB microrobot was nucleated in the 1% PNIPAAm solution. When the bubble is nucleated, the temperature of the liquid should be 100 °C. There was an observable gelled area of PNIPAAm around the nucleated bubble, with a boundary representing the phase-transition temperature of the PNIPAAm. Thus, the temperature gradient can be measured by assuming the temperature at the center of the laser focus is 100 °C and the temperature at the edge of the area of gelled PNIPAAm is 32 °C. Using this method, the temperature gradient was measured to be 1.08 $°C.\mu m^{-1}$ on the Ti-coated substrate and 0.67 $°C.\mu m^{-1}$ on the α-Si-coated substrate. The approximately 60% higher thermal gradient on the Ti-coated substrate, along with the increased absorption of the laser light, contributes to higher actuation speeds observed on these substrates (Fig. 3.3).

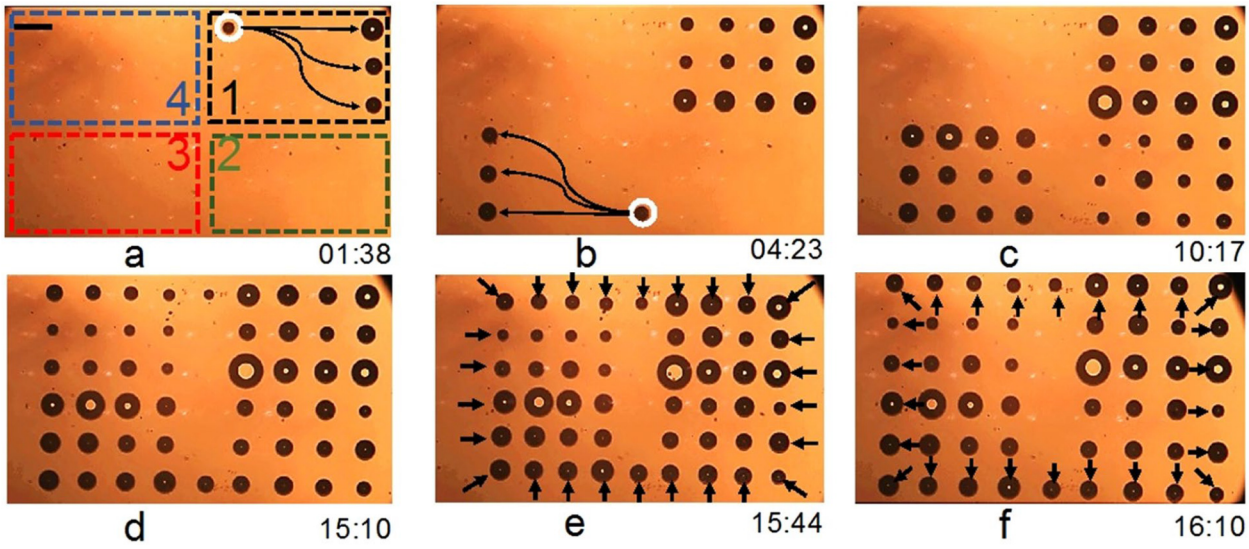

Figure 3.6. Generation and independent actuation of 50 OFB microrobots in parallel. (**a**) Top view of the workspace, virtually divided into four quadrants as labeled. The OFB microrobots were serially generated by the laser spot marked with the white circle. After generation, the bubbles were moved along trajectories indicated by the arrows using additional actuation laser spots. (**b**) Twelve OFB microrobots were generated in quadrant 1. Each microrobot is held in place by its own dedicated actuation laser spot. The laser beam marked with the white circle nucleated the microrobots at quadrant 3, following the same procedure used for the microrobots in quadrant 1. (**c**) and (**d**) Fifty microrobots were serially nucleated by the laser beams marked with the white circles in (**a**) and (**b**). (**d**) As the serial nucleation occurred in quadrants 1, 3, 2, and 4, the microrobots were assembled in a rectangular matrix. (**e**) The array of 50 microrobots was made to contract towards the center of the workspace (arrows indicate the approximate direction of motion during this operation). To complete the contraction operation, each microrobot needed to move in a different direction, thus demonstrating the independent actuation of 50 OFB microrobots in parallel. (**f**) The array of microrobots was expanded outwards, demonstrating the parallel, independent actuation of each microrobot in a different direction (arrows indicate the approximate direction of motion). Scale bar: 150 μm. Time format: minutes:seconds.

The increased OFB actuation velocities on the Ti-coated glass substrates indicated a more efficient conversion of optical energy into thermocapillary force as compared to the α-Si-coated substrates. Thus, the Ti-coated substrates were used to increase the number of OFB microrobots that could be actuated at once. Using the experimental setup described earlier, 50 OFB microrobots, with an average radius of 35 μm, were generated in a workspace spanning 2400 μm by 1350 μm (Fig. 3.6). The total amount of laser power available on the substrate was 330 mW, distributed among the 50 laser spots used to actuate the microrobots. In this setup, each laser spot needs an intensity of approximately 1.35 $kW.cm^{-2}$ to stably actuate an OFB microrobot. Although this level of optical

intensity is sufficient to actuate an OFB microrobot, it is not enough to generate a microbubble. To enable the generation of the 50 OFB microrobots with the limited laser power available, the workspace was divided into four quadrants (Fig. 3.6a) The OFB microrobots in quadrant 1 were generated by the laser spot marked with a white circle in Fig. 3.6a. The optical intensity of the generating laser spot was temporarily increased to approximately 7.5 $kW.cm^{-2}$. The bubble microrobot was generated in 2 seconds, and then the beam power was reduced to the actuation intensity of 1.35 $kWcm^{-2}$. The bubble generation process occurred serially for the 12 OFB microrobots in quadrant 1; after each bubble was generated, an actuation light spot was used to move the OFB microrobot into position (Fig. 3.6a and b). Next, the 12 OFB microrobots in quadrant 3 were generated in a similar fashion by the optical spot marked with a white circle in Fig. 3.6b. Subsequently, OFB microrobots in quadrant 2, then quadrant 4 were generated, followed by two more microrobots (Fig. 3.6c and d). The total time for generating 50 OFB microrobots was 15 minutes, 10 seconds; however, bubble generation could be done in parallel, reducing the duration of the operation, by using a laser with a higher output power.

Following the generation of the 50 OFB microrobots, the parallel, independent actuation of the microrobots was demonstrated (Fig. 3.6e and f). The formation of the microrobots was contracted and expanded, allowing each of the 50 microrobots to be actuated in different directions at the same time. Initially, the microrobots were spaced in a rectangular pattern of 1806 μm by 1125 μm (Fig. 3.6d). The pattern was contracted to a rectangular arrangement of 1471 μm by 893 μm, at an average actuation velocity of 5 $\mu m.s^{-1}$ (Fig. 3.6e). The 50 OFB microrobots were then actuated to expand the formation into a rectangular arrangement of 1786 μm by 1146 μm, at an average velocity of 7 $\mu m.s^{-1}$ (Fig. 3.6f). During this operation, the OFB microrobots were manually controlled. The actuation speed during contraction was maintained slightly lower than the actuation speed during expansion to minimize the risk of bubbles merging.

3.4 Independent Actuation of Pairs and Groups of Microrobots in Various Trajectories

The OFB microrobots were also actuated in subgroups. Two subgroups of 24 microrobots were formed, and the remaining two of the 50 total OFB microrobots were actuated in linear and circular trajectories, demonstrating both group motion and individual actuation of single microrobots along distinct paths. First, the 24 OFB microrobots on the left side of the workspace were made to

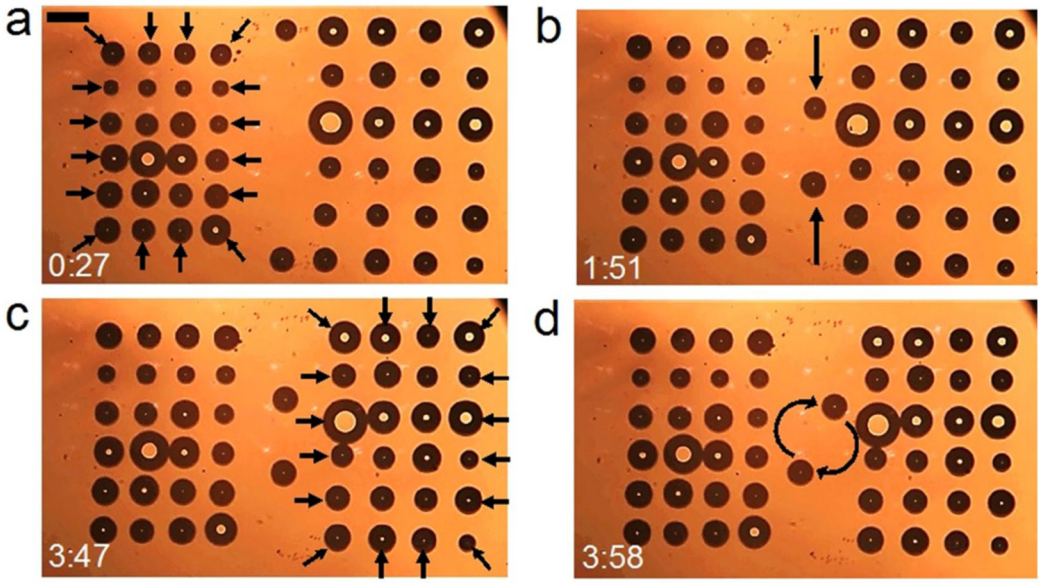

Figure 3.7 Actuation of subgroups of microrobots in various trajectories. (**a**) The matrix of 24 OFB microrobots at the left side of the workspace was made to contract, as indicated by the arrows. The other 26 microrobots were kept stationary. (**b**) A pair of microrobots were actuated towards each other while the other 48 microrobots were kept stationary, showing independent movement of a small subset of the microrobots. (**c**) The matrix of 24 OFB microrobots at the right side of the workspace was made to contract, as indicated by the arrows, while other twenty-six microrobots were kept stationary. (**d**) A pair of microrobots were actuated along a circular trajectory, first in the clockwise direction, then in the counter-clockwise direction. Scale bar: 150 μm. Time format: minutes:seconds

contract their formation, at a speed of 5.5 μm.s^{-1} (Fig. 3.7a). The other 26 microrobots remained in their respective positions, thus demonstrating actuation of a subgroup of the total available OFB microrobots. Then, the two OFB microrobots at the middle of the workspace were moved towards each other, demonstrating actuation of a smaller subgroup in a linear trajectory (Fig. 3.7b). The 24 OFB microrobots on the right-hand side of the workspace were then moved towards each other in parallel, while other microrobots were kept at their respective positions (Fig. 3.7c). The two OFB microrobots at the center of the workspace were also rotated clockwise and counter-clockwise, demonstrating the actuation of OFB microrobots along a circular trajectory with a diameter of 314 μm, at an angular velocity of 0.14 rad.s^{-1} (Fig. 3.7d and e).

3.5 Micromanipulation of a Microstructure by a Pair of OFB Microrobots

The independent actuation of multiple OFB microrobots enables the flexible manipulation of micro-objects, with control over orientation. This was performed using a pair of OFB microrobots

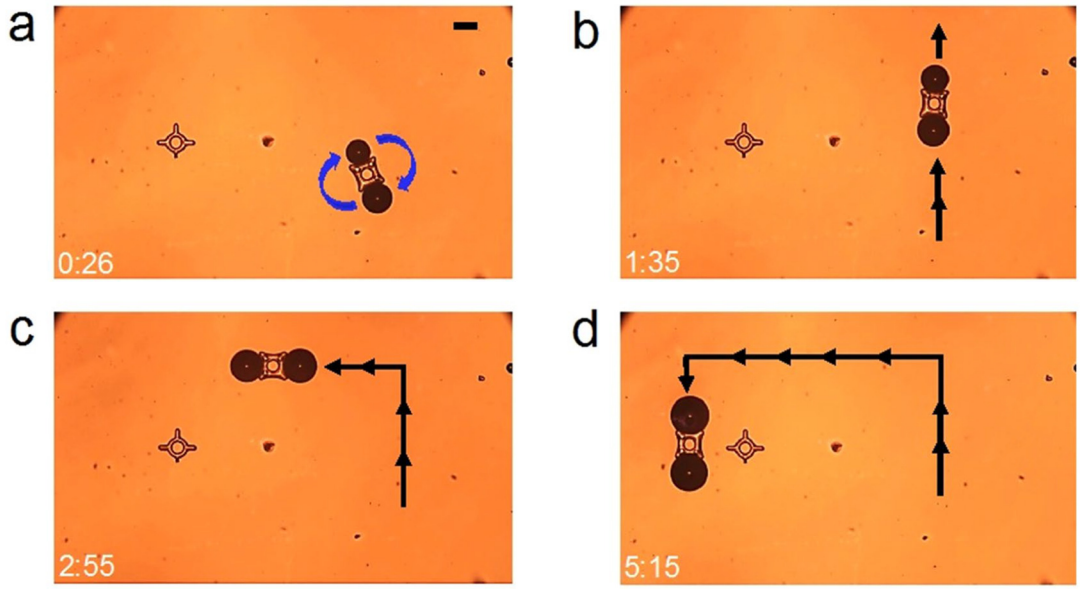

Figure 3.8. Micromanipulation of a microstructure using a pair of OFB microrobots. (**a**) A pair of OFB microrobots approached an SU-8 structure, grasped it, and rotated it towards the direction of the navigation. (**b–d**) The micro-object was transported along a piecewise linear path. The micro-object was transported along the 2017-μm-long path at the average speed of 6.0 μm.s^{-1}. Scale bar: 100 μm. Time format: minutes:seconds.

on a 50-μm-high SU-8 microstructure that measured 124 μm per side, and had walls 33 μm thick that surrounded a circular hollow core (Fig. 3.8). A pair of microrobots were used to hold the microstructure in a pincers-like grasp, rotate the structure, and move it along linear trajectories. Upon completion of the micro-transportation, the microstructure was released at the destination location. Importantly, the friction and drag forces on this SU-8 structure were too large for a single OFB microrobot to overcome. Thus, the manipulation of this object was possible only because the OFB microrobots can perform cooperative micromanipulation.

3.6. Micromanipulation by Multiple OFB Microrobots

The independent operation of OFB microrobots allows them to perform micromanipulation tasks that may not be achievable by a single microrobot. For example, a star-like SU-8 microstructure was transported using multiple OFB microrobots (Fig. 3.9). The microstructure has three arms, each with a length of 100 μm, radiating from a hollow circular core with a diameter of 100 μm. The friction and drag forces on this microstructure make it difficult for one OFB microrobot to move. A single microrobot was able to rotate the structure (Fig. 3.9a), but could not translate it. Even the cumulative effort of two OFB microrobots did not generate sufficient force to move the

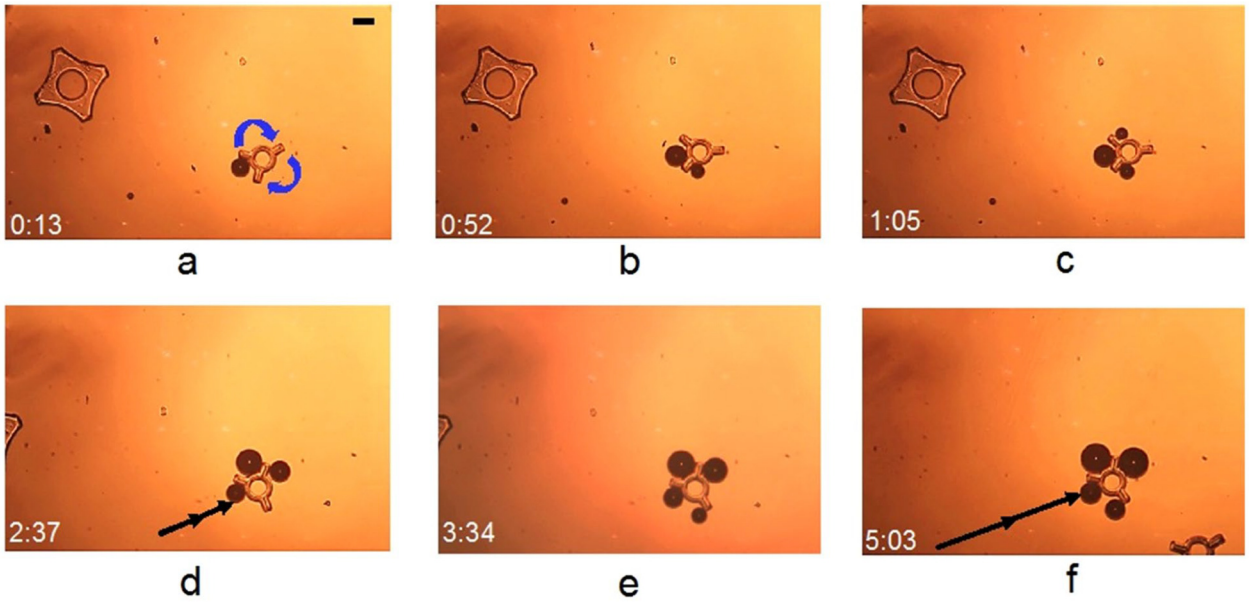

Figure 3.9. Micromanipulation by multiple microrobots. (**a**) A single OFB microrobot attempted to transport a star-like SU-8 microstructure but could only effect limited rotational movement. (**b**) A failed attempt to move the microstructure by two OFB microrobots. (**c, d**) Three OFB microrobots were able to transport the microstructure along a linear path at a speed of 8 μm · s−1. The micro-object was transported over a distance of 490 μm. (**e,f**) Four OFB microrobots grasping the same microstructure and transporting it along the similar linear trajectory. The micro object was carried over a distance of 1890 μm at 22 μm · s−1. Scale bar: 100 μm. Time format: minutes:seconds.

microstructure (Fig. 3.9b). However, the combined force of three OFB microrobots was sufficient to move the structure in a linear trajectory at 8 $\mu m.^{-1}s^{-1}$ (Fig. 3.9d). The manipulation speed was increased to 22 $\mu m.s^{-1}$ along the same straight path when four OFB microrobots were used to move the object. To quantify the effect of moving an object using varying numbers of OFB microrobots, one to four OFB microrobots were used to transport a 500-μm-diameter glass bead. A single microrobot moved the bead at a maximum velocity of 61 $\mu m.s^{-1}$ (443 nN), and two microrobots working together moved the same bead at 92 $\mu m.s^{-1}$ (669 nN). (The forces were calculated from the maximum velocity using Stokes' Law with Faxen's correction [99]). The speed of manipulation increases as more microrobots are used, although this effect begins to saturate for more than three microrobots (Fig. 3.10). Part of the reason for the saturation is that the forces exerted by four or more microrobots were not entirely in the direction of motion of the bead, so adding additional microrobots did not result in a linear increase in the transportation velocity (Fig. 3.10). Thus, the optimum number of microrobots required for manipulation of a microstructure partly depends on the shape and size of the microstructure.

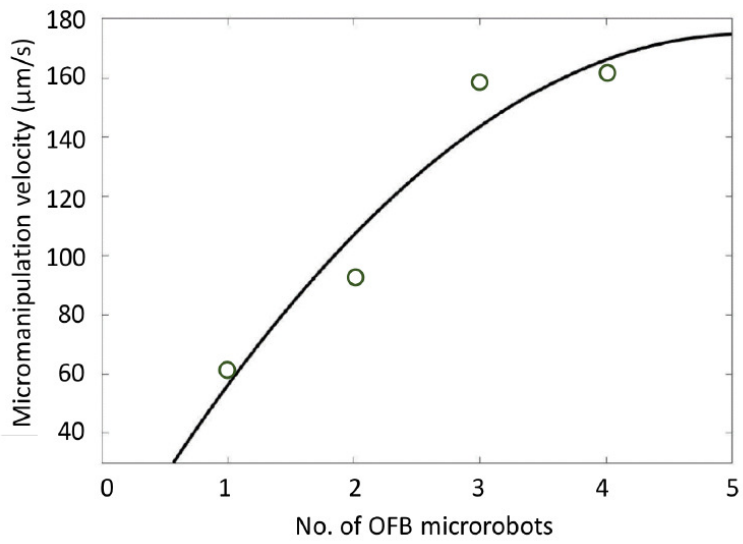

Figure. 3.10 Single micro-object manipulation with increasing numbers of microrobots. The maximum velocity achieved while transporting a 500-µm glass bead increases as more microrobots contribute to the manipulation, due to the increased actuation force. However, this effect saturates, as using four microrobots starts to increase the cross-sectional area of the bead-microrobot cluster, increasing drag.

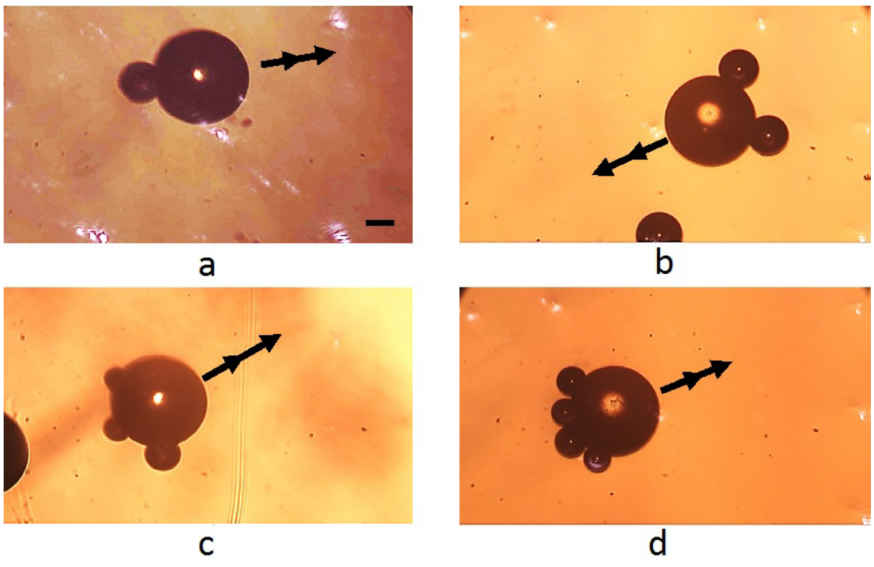

Figure. 3.11 Micro-object manipulation using single and multiple OFB microrobots. (**a**) A single OFB microrobot transports a 500-µm-diameter glass bead. (**b**) Two microrobots transport the same bead. (**c**) Three microrobots transporting the bead. (**d**) Four OFB microrobots pushing the same glass bead. The arrows indicate the direction of transportation in each image. Scale bar: 100 µm.

3.7 Cooperative Microrobot Transportation of Multiple Micro-objects

The potential for the rapid delivery of multiple payloads is demonstrated by using multiple OFB microrobots to perform the simultaneous transportation of multiple micro-objects, as compared to a single microrobot performing the same task (Fig. 3.12). The micromanipulation time using a single microrobot, six microrobots controlled manually, and six microrobots controlled automatically were consecutively 2 minutes 53 seconds, 1 minute 32 seconds, and 26 seconds. The baseline experiment used a single OFB microrobot to transport the 64-μm-radii (average) glass beads from their initial locations to a desired location (Fig. 3.12a–d). Since there was only a single microrobot, this was a serial operation. The center of the assembly location was 844 μm away from the initial positions of the beads (Fig. 3.12a–d), so the microrobot has to travel a total distance of more than 5908 μm during the assembly operation. The average transportation velocity was 34 $\mu m.s^{-1}$, resulting in an assembly time of 2 minutes, 53 seconds.

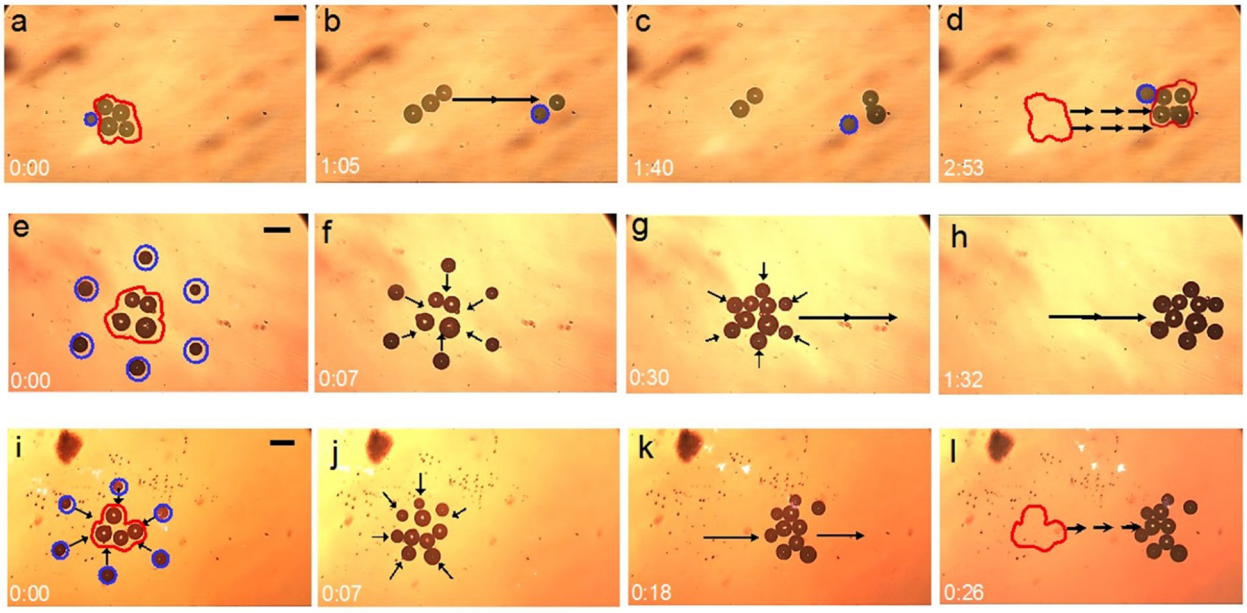

Figure. 3.12 Cooperative microrobot transportation of multiple micro-objects. (**a–d**) An assembly of four glass beads was transported serially using a single OFB microrobot. (**a**) The OFB microrobot is circled in blue, and the four glass beads are enclosed by a red line. (**b–d**) The four glass beads were serially transported 844 μm away from the initial location, over an assembly time of 2 minutes and 53 seconds. (**e–h**) Manually controlled cooperative microrobot transportation of multiple micro-objects. (**e**) Six microrobots are positioned equidistant from the glass beads. The microrobots are circled in blue, and the glass beads are enclosed by a red line. (**f**) The OFB microrobots were manually

controlled to approach the beads to grasp them. (**g, h**) The glass beads were grasped by the microrobots, and the beads were transported to the delivery location. The assembly time was 1 minute, 32 seconds. (**i–l**) Automated cooperative microrobot transportation of multiple micro-objects. (**i, j**) The microrobots, circled in blue, grasped the glass beads enclosed by a red line. (**k**) The glass beads were grasped by the OFB microrobots and transported to the desired location. (**l**) The glass beads were transported from the initial position to the final destination in 26 seconds.

In contrast, cooperative manipulation using multiple microrobots accomplished the transportation of the glass beads in 1 minute, 32 seconds (Fig. 3.12e–h). A different set of four glass beads with an average radius of 64 μm was transported the same distance as before, but this time all the beads were transported at once. In this case, six microrobots were moved by the user into a configuration that surrounded the beads (Fig. 3.12e–f), then the microrobot group was used to transport the all the beads to the desired location (Fig. 3.12g, h). The average speed of manipulation was 13.6 $\mu m.s^{-1}$, which is 60% less than in the single-microrobot-assisted manipulation. However, despite the lower manipulation speed, there was a 50% reduction in manipulation time because all the beads were transported at once. The lower manipulation speed during the transportation of multiple micro-objects was partially to reduce the risk of bubbles merging. The adjacent microrobots were spaced slightly less than the diameter of the beads under manipulation to securely cage the beads, but the close proximity of adjacent microrobots meant that there was a risk of OFB microrobots merging while carrying the payload. Thus, during the manual operation of transporting multiple micro-objects simultaneously the actuation speed was varied from 11 μm to 16 μm, which allowed the operator to maintain a stable trapping formation of the microrobots.

Simultaneous transportation of the four glass beads was also carried out by controlling the OFB microrobots using an automated sequence (Fig. 3.12i–l). In the automated sequence, six OFB microrobots were used to grasp an assembly of four glass beads of 62-μm-radii (average) and transported them the same distance as in previous experiments, but by controlling the microrobots without continuous human interaction. The total operation of approaching the beads, grasping, and carrying the payload by six microrobots was initiated with a single click of a button on the user interface. The automated simultaneous transportation of multiple micro-objects was accomplished by running 34 sequences of frames of the optical patterns at an interval of 750 ms per frame. This controlled the formation of the microrobots that transported the payload 835 μm from the initial position in 26 seconds, at an average transportation speed of 46 $\mu m.s^{-1}$.

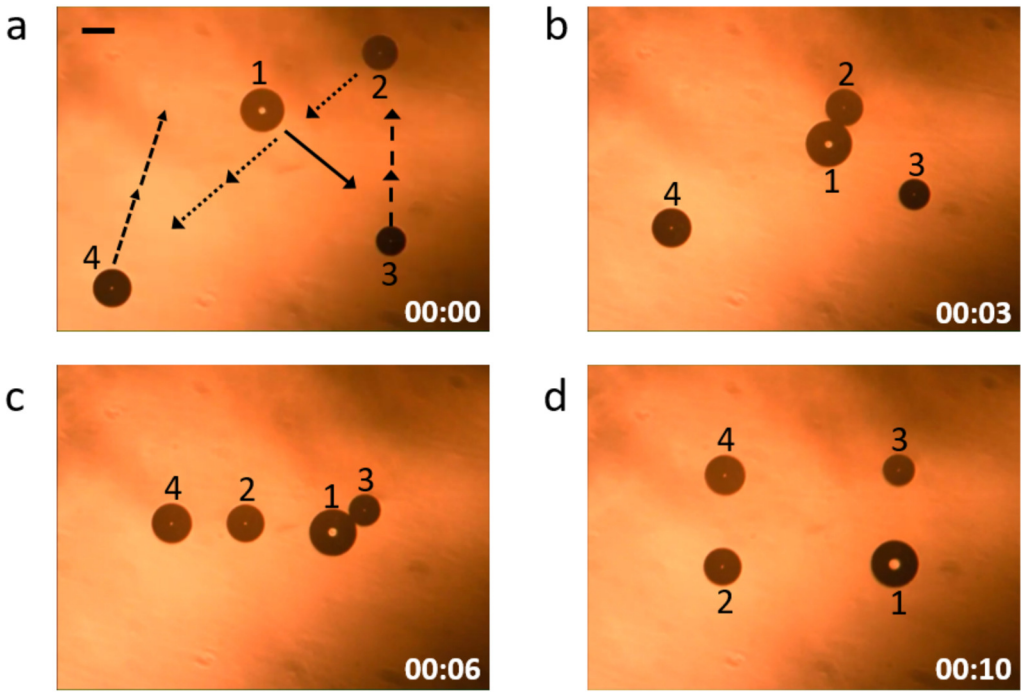

Figure. 3.13 Independent actuation of multiple microrobots at different velocities. (a) Four OFB microrobots were generated at random locations within the workspace. Each microrobot was actuated along a separate trajectory, as indicated by the arrows. (b) The microrobots are actuated towards their respective destinations. Microrobots 1 and 2 contacted each other, but did not merge. (c) Microrobots 1 and 3 contacted each other, but did not merge. (d) The four microrobots have reached their destination location, forming a rectangular shape. Microrobots 1 to 4 were independently actuated along different linear trajectories at velocities of 47.2, 83.1, 44.9, and 64.7 μm·sec-1, respectively. Scale bar: 100 μm. Time format: minutes:seconds.

Automatic cooperative microrobot transportation of the microbeads improved the assembly further: it resulted in an 80% reduction in assembly time compared to single-microrobot manipulation, and a 66% reduction in assembly time compared to manually controlled multiple microrobot transportation. In both the single-microrobot micromanipulation and the manual multiple microrobot transportation, the operator controls the microrobots using a computer mouse. Using the control interface, a human operator can control only one microrobot at a time during the payload transportation. Using the automated control, each microrobot can be independently actuated at the same time to adjust the trapping formation for efficient delivery of the beads, resulting in a shorter assembly time. For example, in this experiment, the microrobots were concentrated on the trailing edge of the cluster of beads, so that more microrobots were engaged in the transportation of the beads. Automatic actuation also allows the independent control of

multiple OFB microrobots along the different directions at different velocities at the same time, demonstrating actuation that is uncoupled to each other (Fig. 3.13).

3.8 Discussion

Light was used to control the actuation of OFB microrobots, providing flexibility and on-the-fly adaptability for various micromanipulation tasks. Furthermore, optical control makes it straightforward to independently control many microrobots at once. This was demonstrated with by the independent actuation of 50 OFB microrobots in parallel. The microrobots can work cooperatively, as shown by the micromanipulation of micro-objects using a pair of microrobots, the transportation of a micro-structure using multiple microrobots, and the simultaneous transportation of multiple micro-objects by a team of microrobots. Independent actuation of multiple microrobots resulted in increased forces exerted on objects under manipulation, and shorter completion times for tasks like the transportation of multiple micro-objects. Further automation of the control system, as well as the implementation of motion planning and formation control algorithms, will further enhance the microassembly capabilities of the OFB microrobot system. The current OFB microrobot system is limited to the micromanipulation of objects in 2D, as the bubbles are formed and actuated on the surface of the substrate. Most microrobotic systems have the same limitation, with the exception of some recently demonstrated 3D microassembly platforms [118]. However, it may be possible to implement layer-by-layer 3D microassembly in the OFB microrobot system, in a manner similar to methods used in other systems that generate forces near a surface [119].

The liquid media used in the experiments presented here was silicone oil, instead of cell culture media or buffer solutions such as PBS. However, the mechanism of OFB microrobot actuation is compatible with aqueous solutions, including PBS [29, 30]. Silicone oil was used in these experiments due to its lower thermal conductivity compared to water. This helps to maintain the thermal gradients necessary for the actuation of many OFB microrobots, which is limited by the output power of the laser that was available. Actuation of 50 OFB microrobots is feasible in aqueous solutions if there is sufficient optical intensity at the substrate (approximately 400 kW・cm^{-2}) ref. [31]. This can be accomplished by using a higher-power laser, and reducing power losses in the optical system (the lenses used here are designed for visible wavelength transmission, and

have increased losses for infrared light). Even without actuation in water, OFB microrobots actuated in silicone oil can manipulate cells seeded in hydrogels [41] or water droplets [120], as silicone oil is biocompatible [121] and oxygen permeable [122]. Microrobotic manipulation in silicone oil can also be used to transport droplets of immiscible fluid for clinical diagnostics [123–125] and to manipulate droplets with encapsulated biological materials [124].

3.9 Conclusion

In this chapter the independent actuation of 50 microrobots in parallel on a titanium-coated glass slide was demonstrated. The microrobots were simultaneously maneuvered in different directions to demonstrate uncoupled parallel actuation. The multidirectional maneuverability of the microrobots along various trajectories was demonstrated, and provided the flexibility needed to manipulate micro-objects into various orientations. The independent actuation of multiple OFB microrobots enables cooperative micromanipulation, and enhances the assembly capabilities of this microrobot system. Multiple OFB microrobots working together are capable of exerting more force on microstructures as demonstrated by one microrobot exerting 443 nN force and two microrobots exerting 669 nN force while co-operatively manipulating one micro-object. In addition, cooperative micromanipulation by a team of OFB microrobots was used to simultaneously transport multiple micro-objects in 26 s, compared to manipulation using a single microrobot that took 2 min. 53 s. Here, micro-object transport is demonstrated in closed chamber. However, bio-micromanipulation task benefits if the manipulation takes place in an open reservoir. In the next chapter, microrobot actuation and cooperative micromanipulation is demonstrated in open reservoir, and in cell-compatible media.

CHAPTER. 4 COLLABORATIVE MICROMANIPULATION USING MULTIPLE BUBBLE MICROROBOTS IN AN OPEN RESERVOIR

Micromanipulation of bio-microobjects is useful in tissue engineering, and requires high-throughput, scalable, cell-friendly assembly of mesoscale structures with micron resolution. One potential method of achieving such functionality is manipulation by independently actuated multiple microrobots in cell-culture media. In previous chapters up to fifty OFB microrobots were generated, actuated, and co-operatively operated to perform various micromanipulation task in a closed chamber filled with silicone oil. Here, nine opto-thermocapillary flow-addressed bubble (OFB) microrobots were independently actuated in saline solution in an open reservoir, demonstrating the operability of the OFB microrobot system in a conventional cell-culturing environment. Laser heating generated the bubble microrobots in a fluid medium, and controlled the actuation of the microrobots, as detailed in Chapter 2. The microrobots were controlled using a computer-generated holographic (CGH) control system, also explained in Chapter 2. The collaborative manipulation of four glass beads was demonstrated using two to three OFB microrobots. The micro-objects were transported over several millimeters by moving the microscope stage for coarse motion, and by CGH control for fine actuation of the microrobots. Following transportation, the micro-objects were assembled into a particular geometry. Independent actuation of multiple microrobots in saline solution along with collaborative long-range manipulation demonstrates the capability of the system to assemble cell-laden microgels over a large area with potential microscale accuracy, making this suitable for tissue engineering applications. This work also shows that the system is scalable, as tasks can be assigned to the required number of microrobots, and the system is compatible with a traditional open-reservoir cell-culturing environment.

4.1 Parallel Actuation of Multiple Bubble Microrobots in Saline Solution in an Open Reservoir

Manipulation of bio-microobjects in a cell-friendly environment allows assembled cells to grow upon completion of the manipulation. This functionality requires the manipulation to take place in cell-compatible solutions, and it is also preferable to occur in an open reservoir, which is

compatible with conventional cell culturing protocols. Further, micromanipulation for an application like tissue engineering requires the mesoscale assembly of cells with microscale accuracy, which can be achieved by the parallel actuation of multiple microrobots. However, it is challenging to meet all these criteria at once: actuation of multiple microrobots in parallel, in electrically conductive cell-compatible media, and in an open reservoir. Magnetic microrobots can be actuated in electrically conductive culture media, but actuating multiple magnetic microrobots independently remains challenging [12]. Microrobotic systems that use electric fields face hurdles when actuated in electrically conductive fluids [86]. Bacteria-propelled microrobots based on the motility of the bacteria can operate in electrically conductive fluids and open reservoirs, but these have a limited degree of controllability, and primarily use global control of multiple microrobots [126]. Pneumatic actuation has also been used for particle manipulation in closed fluidic chambers, but this may not be suitable for open reservoirs [127, 128].

A microrobot actuation method which can address all the challenges mentioned above is opto-thermocapillary flow-addressed bubble (OFB) microrobots [129]. OFB microrobots are gas bubbles in liquid media generated by opto-thermal heating of a substrate, and these bubble microrobots can be actuated along optically generated thermal gradients [27]. Compared to the microrobot actuation methods mentioned previously, an OFB microrobot system has less dependence on the electrical and magnetic properties of the micro-object under manipulation and the surrounding medium, making it suitable for actuation in an electrically conductive cellcompatible solution like phosphate-buffered saline (PBS) [130]. Opto-thermal nucleation and actuation enable the OFB microrobot to operate in open reservoir and makes it possible to control many of them independently [1]. In addition, mesoscale manipulation of payloads with microscale accuracy is possible, making this system suitable for an application like tissue engineering [29, 85, 131, 132]. In previous chapter, 50 OFB microrobots were independently actuated, and the cooperative manipulation of various micro-objects was performed in silicone oil in a closed fluidic chamber [1]. This chapter is focused on the cooperative manipulation of micro-objects in cell-compatible media in an open reservoir for demonstrating the performance of the microrobot system if used in conjunction with conventional cell culturing. Here, we present the parallel actuation of nine OFB microrobots in PBS solution in an open reservoir. The microrobots were independently actuated along different trajectories using a computer-generated holographic (CGH) control

system, demonstrating the uncoupled actuation of each of them. In addition, the collaborative manipulation of several glass microbeads was demonstrated in an open reservoir containing PBS. The glass microbeads were transported over several millimeters using two or three microrobots. During the transportation, the microscope stage was moved for coarse motion, and CGH control was used for the fine actuation of the microrobots. These functionalities of the OFB microrobot system make it attractive for tissue engineering applications.

4.1.1 Experiment Setup

The floor of the fluid reservoir used in this experiment is coated with a light-absorbing material (Fig. 4.1a). Two different substrates were used; the first type was a 1-mm-thick glass slide coated with 100 nm of indium tin oxide (ITO) and 1 μm of amorphous silicon (α-Si). Eight layers of 80-μm-thick double-sided polyimide tape stacked on the surface of the substrate formed the walls of the fluid reservoir on this substrate (Fig. 4.1a). The second substrate was a 1-mm-thick glass slide coated with 100 nm of titanium. To make the walls of the fluidic reservoir on the second type of substrate, 4-mm-thick Polydimethylsiloxane (PDMS) was bonded to the surface using oxygen plasma bonding (Harrick Plasma PDC 32G). The titanium-coated substrate was used in the micromanipulation experiments to take advantage of higher light absorption as compared to the α-Si-coated substrate [1]. This resulted in a higher speed of manipulation on the titanium-coated substrates for the same laser power. PBS was used as the liquid media for all experiments.

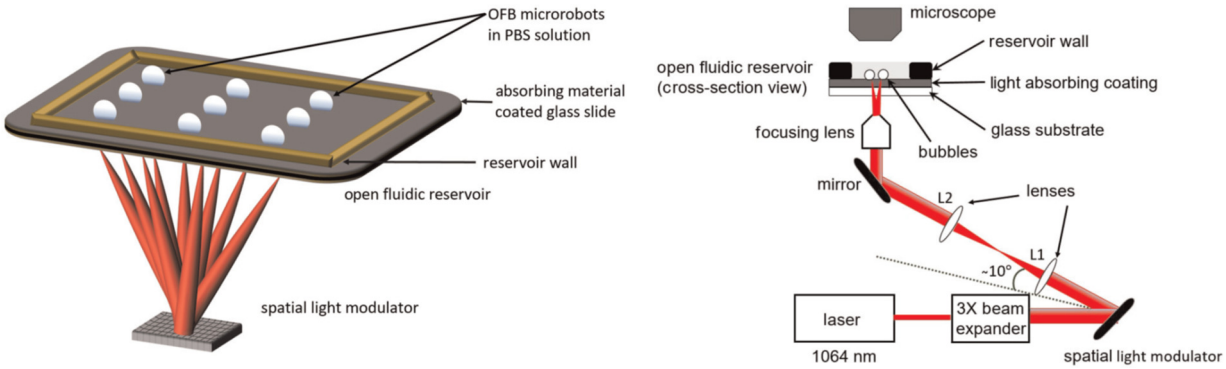

(a) (b)

Figure. 4.1 Schematic of the OFB microrobot system. (a) The substrate of the open reservoir is a glass slide coated with a light-absorbing material. A spatial light modulator creates multiple laser spots on the absorbing layer of the reservoir; each microrobot is actuated by a single laser spot. The height of the reservoir wall determines the height of

the fluid column in the reservoir. (b) Experimental setup for the actuation of multiple OFB microrobots and collaborative micromanipulation in PBS solution in the open reservoir

The collimated wavefront of the single laser beam was shaped into nine beams using a programmable spatial light modulator (SLM) (Fig. 4.1a), focused on the absorbing layer of the substrate. This created the required hot spots necessary to actuate nine OFB microrobots. Each OFB microrobot was nucleated by momentarily increasing the optical power of a single focused laser spot (of the nine total laser spots) to a level sufficient to vaporize a small volume of liquid medium. The power of nucleating laser beam was reduced as soon as the bubble was generated to a level appropriate for actuating the bubble microrobot. The actuating laser beam induces thermal gradients around the absorbing layer, creating surface tension gradients and thermal Marangoni effects that act upon the bubble. This causes the OFB microrobot to move towards the hot spots created by the laser beams, enabling actuation of each microrobot by the location and movement of the laser beam pattern (Fig. 4.1a).

The experimental setup consists of a 1064-nm single-mode (TEM 00) linearly polarized laser (Laser Quantum, Ventus 1064, 1.5 W) with a beam diameter of 3.2 mm (approx.). The laser is input into a 3X beam expander (Edmund Optics), resulting in 10-mm-diameter (approx.) collimated beam (Fig. 4.1b). The expanded beam was incident on a SLM (Hamamatsu, LCOS-SLM X10468-07) capable of modulating the reflected laser beam to create desired beam pattern. The SLM was configured by a CGH control system, which is an application developed by modifying the existing Red Tweezers program [28, 106]. User defined beam patterns were created by displaying the corresponding hologram on the SLM. The phase modulated wavefront was then focused onto the absorbing layer of the substrate with a 10x objective lens (Mitutoyo, 0.28 NA), creating the desired beam pattern consisting of nine laser spots. Both types of substrates mentioned previously were functionalized to increase hydrophilicity, to facilitate bubble actuation. The substrates were cleaned using an oxygen plasma cleaner (Harrick Plasma PDC 32 G) and soaked in a poly(ethyleneglycol)–silane solution (2-[methoxy(polyethyleneoxy)propyl]-trimethoxysilane, Gelest Inc.) for 8 h. The coated substrate was gently rinsed with ethanol and air dried before use.

4.1.2 Microrobot Nucleation and Driving Mechanism

An SLM was used to display user-defined holograms that shaped an input laser beam into a pattern of multiple laser spots, as required for the actuation of multiple microrobots. The computer generated holographic control system explained in section 2.4 was used for creating the beam pattern and control them according to user desire. Once a pattern consisting of nine spots was created on the LabVIEW user interface (Fig. 4.2a), the location of each spot in the LabVIEW work area are sent to the OpenGL Shader hologram engine, and the corresponding hologram is calculated (Fig. 4.2b). The CGH controls the phase of the incident wavefront, creating the user-defined light pattern on the floor of the fluid reservoir (Fig. 4.2c). The light pattern is focused on the absorbing layer of the substrate, generating the array of OFB microrobots (Fig. 4.2d). Each optical beam in the array actuates one OFB microrobot. The physical size of each pixel in the camera image represents 1.24 μm on the substrate. The workspace in LabVIEW interface was divided into 1920 by 1080 divisions of equal-size pixels. The SLM was set to represent one division on LabVIEW interface, equal to one pixel on the camera. image and 1.24 μm on the substrate.

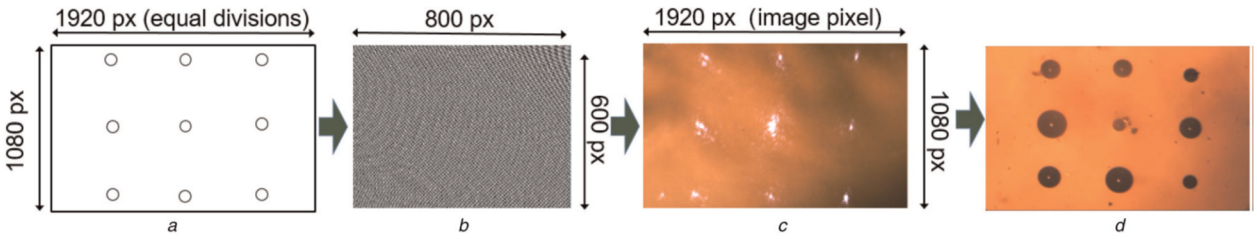

Figure.4.2 OFB microrobot control pattern generation. (a) Pattern of nine focused laser spots created in the LabVIEW user interface window. The window is divided into equal divisions of 1920 px by 1080 px. The locations of the spots are expressed in pixel co-ordinates. (b) Spot coordinates are sent to the OpenGL hologram engine, which calculates and displays the corresponding hologram on the SLM. (c) Microscope image of the fluid reservoir, showing the array of laser beams defined on the LabVIEW interface. (d) Nine OFB microrobots nucleated and controlled using the optical pattern.

4.1.3 Microrobot Actuation in Open Reservoir in Saline Solution

The functionality of the OFB microrobot system was demonstrated by nucleating nine microrobots serially and actuating them independently in parallel in PBS solution. The operation was shown in an open reservoir with a fluid depth of ~700 μm. Figs. 4.3a–d illustrate the nucleation of the OFB microrobots. A square pattern of nine focused laser spots was created on the absorbing layer of the

substrate (Fig. 4.2c). The pattern is not visible in Fig. 4.3 because an infrared filter was placed in front of the camera. The red circle in Fig. 4a shows the location of the laser spot used to serially nucleate the bubbles momentarily increasing the beam power density to ~33 $kW.cm^{-2}$. After bubble generation, the beam power density was reduced to 17.2 $kW.cm^{-2}$, which is sufficient to actuate the microrobot to another laser spot (Fig. 4.3a). One by one, eight OFB microrobots were nucleated by the laser spot marked by the red circle, actuated to their respective actuation spot position, and transferred to the individual actuation spots (Figs. 4.3b and c). The maximum speed of actuation was 40 $\mu m.s^{-1}$ during the transfer (Fig. 4.3). Figs. 4.3 e–g illustrates the independent actuation of nine microrobots in parallel. Once eight OFB microrobots were generated and positioned, the array of microrobots was contracted towards the array center, demonstrating parallel actuation of eight microrobots independently in different directions (Fig. 4.3e). In the middle of the inward actuation of the eight microrobots, the ninth microrobot was nucleated at the array center by increasing the power of the respective laser spot power, and demonstrating the parallel actuation and nucleation of multiple microrobots independently (Fig. 4.3f). The microrobot array was initially placed over an area of 1314 μm × 1130 μm, contracted to occupy an area of 998 μm × 776 μm, and expanded to an area of 1078 μm × 920 μm at an average actuation speed of 2.5 $\mu m.s^{-1}$ (Fig. 4.3g). Multidirectional actuation of nine microrobots in parallel shows that the OFB microrobot system allows actuation of uncoupled individual entities in parallel in PBS solution. Microrobots were manually actuated by the operator by using the computer mouse to drag the circular spots in the LabVIEW user interface. The actuation accuracy is determined by the operator's ability to move the mouse precisely. The operator can also enter the desired coordinates of the microrobot for more precise movement. The highest microrobot positioning accuracy is 3.7 μm (this measurement is limited by the pixel size of the camera used in the setup).

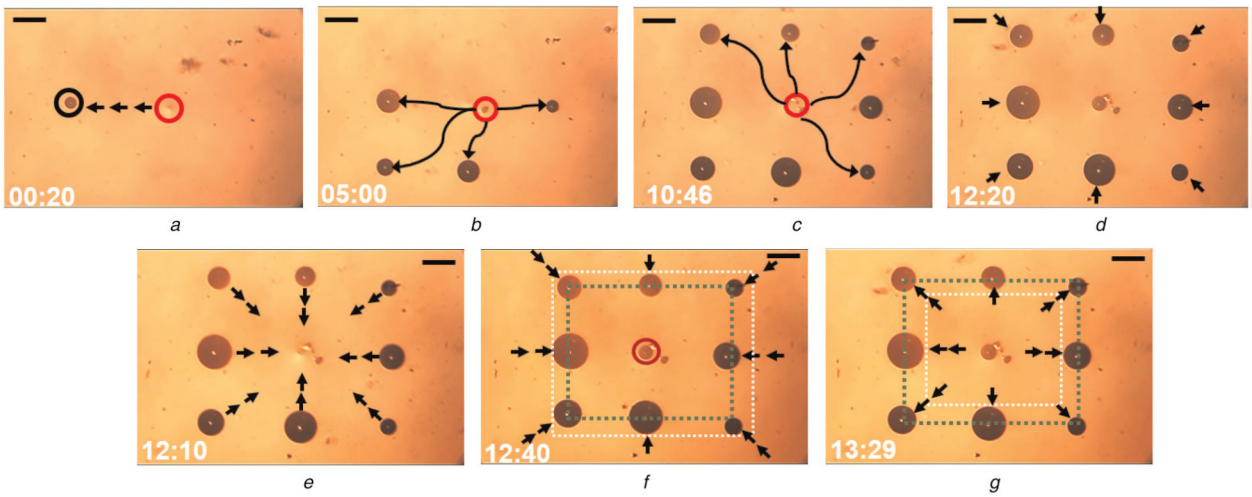

Fig. 4.3 Nucleation and independent actuation of nine OFB microrobots in parallel. Nucleation is shown in a–d, and actuation is shown in e–g. (a) First bubble was nucleated by a laser spot at the position marked by the red circle, and transferred to the actuating beam, marked with by the black circle. (b, c) Eight microrobots were serially generated and transferred to their respective actuation beams. (d) Simultaneous nucleation of the ninth microrobot in parallel with the other eight microrobots moving independently inward, along different trajectories as indicated by the arrows. (e) Array of eight microrobots contracting towards the centre from their initial locations. (f) Nine OFB microrobots actuated in parallel along different trajectories. The pattern occupying the white rectangle contracted to occupy the area of the green rectangle. (g) Pattern occupying the white rectangle expanded to occupy the area of the green rectangle, showing independent manipulation of each microrobot in parallel. Time format is mm:ss. Scale bar: 200 µm

4.1.4 Discussion

In this work the OFB microrobots were nucleated using a continuous-wave laser, resulting in continuous heating of the microrobots over the duration of the actuation. This constant heating increases the size of the microrobot, as seen in Figure 4a-d. A consistent size of OFB microrobots is more desirable to assemble or manipulate compatible sizes of biological micro-objects. As an example, a 50-µm-radius or smaller OFB microrobot is suitable for manipulating mammalian cells, which are approximately 5 to 20 µm in diameter [93], whereas a 100- µm-radius OFB microrobot will be better suited for manipulating larger objects like an *Artemia* cyst (approximately 200 µm in diameter) [133]. The size of the microrobot needs to be controlled for efficient micromanipulation of various biological micro-objects. Using the present experimental setup, one way of controlling the size of the microrobot is to control the power density of each of the laser focal points. However, this is a non-trivial task in an open-loop control system. Another way of

controlling the OFB microrobot size is varying the time of actuation. Figure 4.4 shows the increase in the size of OFB microrobots as a function of time under continuous laser illumination in PBS solution. The microrobot was kept stationary and illuminated by the corresponding actuation spot for 10 minutes. The actuating spots had an optical intensity of approximately 10.74 $kW.cm^{-2}$. These results show that OFB microrobot size increases after nucleation due to the continuous heating by the actuating laser beam. The rate of increase of the microrobot radii was 16 $\mu m.minute^{-1}$. With the appropriate combination of microrobot nucleation close to the location of the micro-objects under manipulation and an actuation time to complete the task, a desired range of microrobot sizes can be maintained by following the plot in Figure 4.4.

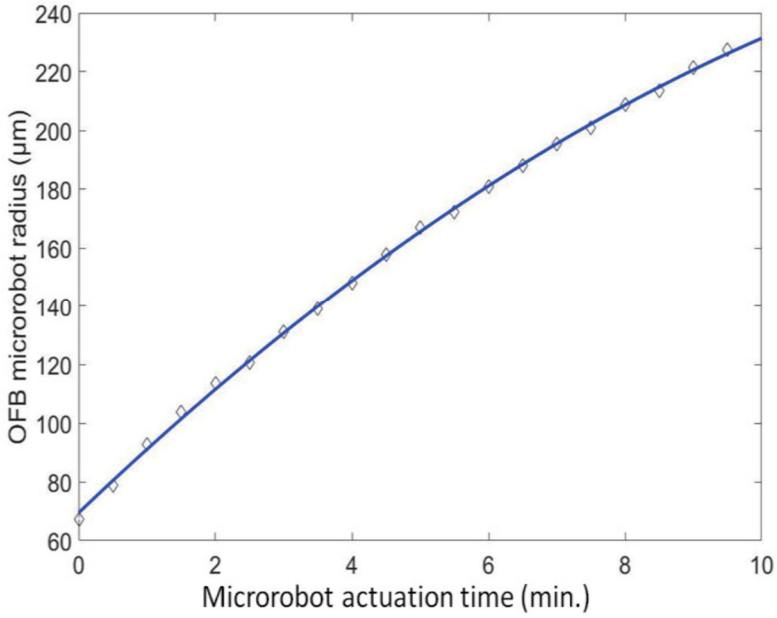

Figure 4.4. The radius of the OFB microrobot over time in PBS solution under continuous illumination by a laser at an intensity of 10.74 $kW.cm^{-2}$.

One advantage of the OFB microrobots is ease of nucleating the microrobots at any desired location, and the ease of eliminating the microrobots after the manipulation task is finished. The bubble microrobots can be nucleated on demand at any arbitrary position within the workspace. Upon completion of the assigned task, the OFB microrobots can be allowed to dissipate into the liquid by switching off the actuating laser spot. The time needed for the largest OFB microrobot in Figure 4.4 (approximately 220 μm in radius after 9.5 minutes of continuous illumination) to dissipate was measured to be 308 ms. The time required for different sizes of OFB microrobots to

dissipate in PBS solution after the laser beam power is set to zero is shown in Figure 4.5. The plot indicates that the time needed for OFB microrobots to dissipate varies mainly within 225 ms to 250 ms, over a range of bubble radii from 50 to 200 μm. The rapid decrease in bubble size can also be used to help maintain the size of the OFB microrobots by modulating the laser [96].

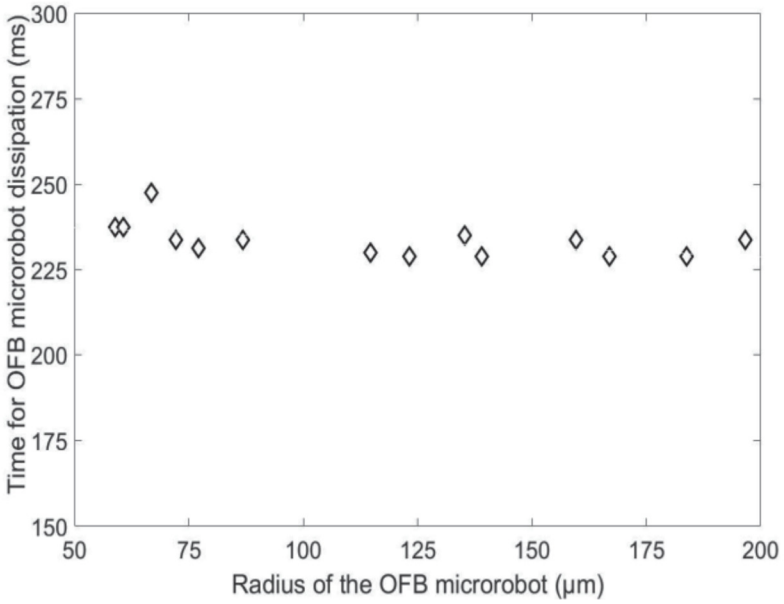

Figure 4.5. Time required by different sizes of OFB microrobot in PBS solution to disappear after the laser illumination is turned off.

4.2 Cooperative Micromanipulation in Open Reservoir

The independent operation of OFB microrobots allows them to engage multiple microrobots to collaboratively perform micromanipulation tasks which may not be carried out by a single microrobot. Moreover, this microrobot system is capable of mesoscale manipulation of micro-objects with potential microscale accuracy. These functionalities of the OFB microrobot system have been demonstrated in the cell-friendly media in an open reservoir.

4.2.1 Mesoscale Collaborative Micromanipulation with Microscale Resolution

The reservoir construct mentioned in Section 4.1.1 was filled with PBS to a depth of 4 mm. Three 475-μm-diameter (approx.) glass beads positioned several millimeters apart from each other were transported and assembled to form a single line formation using two or three OFB microrobots. Fig. 4.6 illustrates the overall micromanipulation operation. Four pairs of partially submerged glass

microbeads were randomly placed on the substrate (Fig. 4.6a). Fig. 4.6b shows a schematic drawing showing the pairs of microbeads, represented with black circles. Three microbeads, numbered 1–3, were manipulated serially along the trajectories marked with black, red, and white arrows. The dotted circle at the end of each trajectory shows the destination location of the beads (Fig. 4.6b). Fig. 4.6c shows the schematic diagram showing the completed microbead assembly, with the beads forming a single line formation. Fig. 4.6d shows an image of the glass beads in PBS solution in the open reservoir after manipulation.

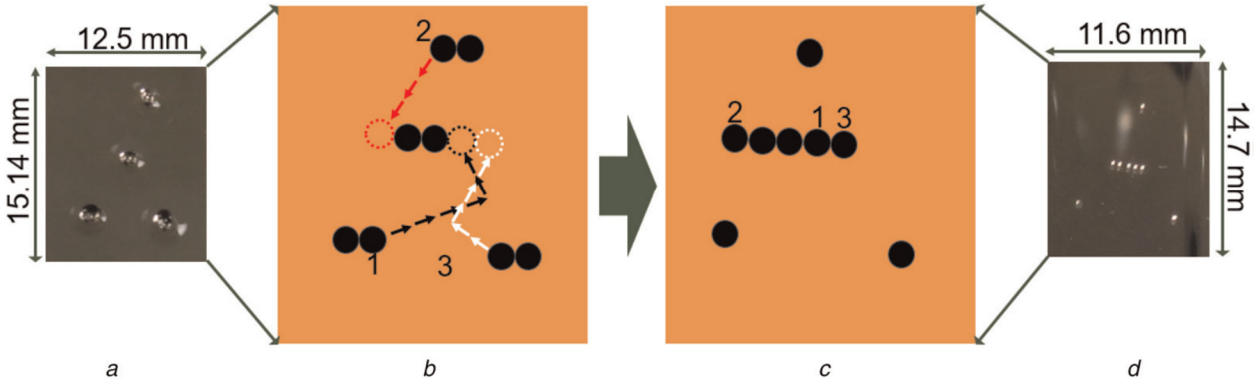

Figure. 4.6 Overview of the micromanipulation of three glass microbeads along different linear trajectories. (a) Image of the four pairs of glass microbeads partly submerged in PBS solution in the open reservoir before manipulation. (b) Schematic of the manipulation operation showing the trajectories of the individual microbeads during manipulation. (c) Microbeads assembled after manipulation. The transported beads are numbered in the order they were assembled. (d) Image of the fluid reservoir after manipulation.

Fig. 4.7 shows microscopic images of the collaborative micromanipulation from Fig. 4.6. Three glass microbeads were transported using multiple OFB microrobots to transport each bead into a single line formation. Five laser spots engaged one to five microrobots (Fig. 4.7a). First, two of the five laser spots were used to nucleate two microrobots, and push one glass bead (Fig. 4.7b). The user manually positioned the two microrobots around the glass bead using the LabVIEW interface. Once the microrobots were positioned, the stage was moved while the laser pattern remained stationary, resulting in bead transportation along the trajectory marked by the black arrows (Fig. 4.7b). Thus, the glass bead was held by two microrobots as the stage moved the reservoir, transporting Bead 1 4807 and 2081 μm along two different linear trajectories, delivering it to the final destination marked with a black dotted circle in Fig. 4.7b. When Bead 1 was close to

the destination location, its position was finely adjusted by pushing it using two microrobots controlled by the CGH system (Fig. 4.7c). Similarly, Bead 2 in Fig. 4.6b was collaboratively carried by two microrobots along a linear trajectory. It was transported 4777 µm along the substrate to the desired location, to form the single line formation with Bead 1 (Figs. 4.7d and e). Unlike the first two spherical beads, the third bead had an irregularity on one side (Fig. 4.7f). If two microrobots transported Bead 3 following the procedure mentioned above, the bead tended to rotate towards the irregularity, making it difficult for two microrobots to carry it on a linear trajectory (Fig. 4.7g). Thus, three microrobots were used grasp Bead 3 more stably and transport it along linear trajectories (Fig. 4.7h). The third bead was manipulated over the distance of 2795 and 3247 µm along two different linear trajectories (Figs. 4.7g–i). The final formation was a single line of transported beads as shown schematically in Fig. 4.6c (microscopic image in Fig. 4.7j). The maximum deviation of the centre of the beads from a straight line was 104 µm. This assembly error was due to operator's skill, and can be improved with automated micromanipulation, as the positioning accuracy of the microrobots is <4 µm.

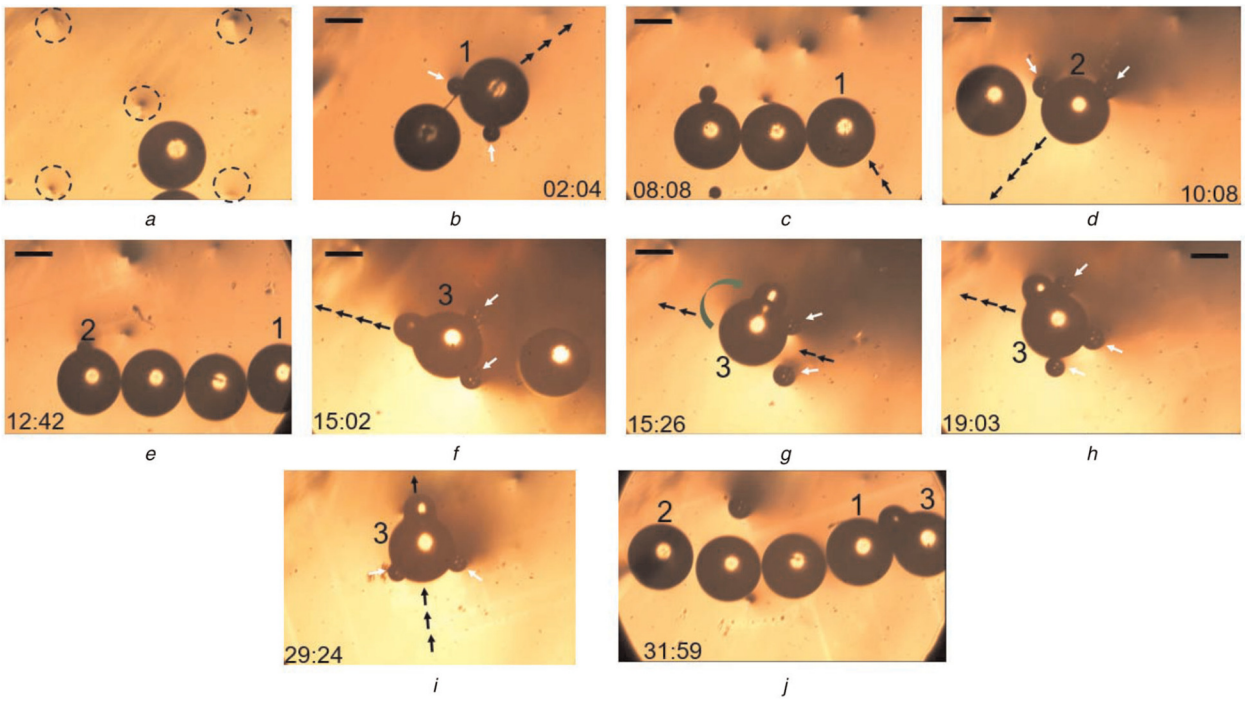

Figure. 4.7 Collaborative manipulation of three micro-objects using two and three OFB microrobots. (a) Five laser spots were generated (marked with black dotted circles). (b) Two microrobots, indicated with white arrows, transported Bead 1 in an open reservoir along the direction indicated by black arrows. (c) Bead 1 is delivered to the destination location beside two other beads, forming a single line. (d, e) Bead 2 is transported and delivered to the

destination by the collaborative effort of two OFB microrobots. (f) Two microrobots marked with white arrows are trying to carry Bead 3, which has an irregular shape due to a particle that was stuck on its surface. (g) Bead 3 tended to rotate towards the particle on its surface, making it difficult for two microrobots to transport it along a linear trajectory. (h) Adding a third microrobot helps with the collaborative manipulation of Bead 3. (i,j) Bead 3 is delivered to the destination location, and the final assembly of five micro-objects into a single line was completed. Time format is mm:ss. Scale bar: 200 μm

4.3 Conclusion

In the experiment where up to nine OFB microrobots were actuated, the sizes of the microrobots at the end of the actuation operation varied from a maximum radius of 230 μm to a minimum radius of 110 μm. The microrobots nucleated earlier were larger compared to the microrobots generated later. Throughout the actuation period, the size of the microrobots increased at a rate of 5–11 $\mu m.s^{-1}$. The difference in the rate of growth was partly due to the irregularities on the light-absorbing coating of the substrate, resulting in slightly different thermal gradients. However, a constant, controllable OFB microrobot size is more desirable. For example, a 50-μm-radius or smaller OFB microrobot is more appropriate for manipulating mammalian cells, which are ~5–20 μm in diameter [134]. On the other hand, a 100-μm-radius OFB microrobot will be better suited for manipulating larger objects like an *Artemia* cyst (~200 μm in diameter) [3]. Controlling the size of the microrobots is an important aspect of OFB microrobot system. The size of OFB microrobots was measured under continuous laser illumination in PBS solution (Fig. 7). The microrobot was kept stationary and illuminated by a laser spot with an optical power density of ~10.74 $kW.^{cm-2}$ for 10 min. The average rate of increase of the microrobot radii was 16 $\mu m.min^{-1}$. However, the rate of increase of the bubble radius was not constant over the time period; it decreased as the illumination duration increased. One way to control the bubble growth is to dynamically vary the power density of each laser spot. The quantification of the increase in bubble size, and the corresponding adjustment of the beam power, is a complex task for an open-loop control system. Another way to maintain a suitable size of the bubble for manipulation in the current setup is to control the actuation time of the microrobot. Using an appropriate combination of microrobots nucleated close to the location of the micro-objects under manipulation and a relatively short actuation time can keep the microrobot size within a desired range. As soon the bubble grows over the maximum allowable size, the respective beam power can be set to zero

allowing the bubble to dissolve in the medium. A new smaller bubble can then be nucleated near to the object under micromanipulation. This procedure was implemented for the collaborative micro-object transportation described in this work. This control phenomenon takes the advantage of two features of the OFB microrobot system: (i) the ease of nucleating microrobots at any desired location, and (ii) the ease of eliminating the microrobots after the manipulation task is finished. The bubble microrobots can be nucleated on demand at any arbitrary position within the workspace. The bubbles also dissolve in PBS in ~240 ms for a wide range of sizes of microrobots, making it easy to launch and withdraw the microrobots from the workspace.

OFB microrobot generation and actuation in saline solution and an open reservoir are challenging compared to the same operation in an oil medium and in closed chamber, so it takes longer to generate the microrobot matrix (Figs. 4.3a–c) [129]. The biggest challenges include the higher drag force experienced by the water-vapour bubble on the hydrophobic substrate (functionalized to improve hydrophilicity), leading to slower actuation comparing to bubbles in silicone oil. Also, if actuation is too rapid, so that the bubble does not follow the actuation laser spot, the bubble will lift off the surface of the substrate, requiring the generation of a new bubble.

In this chapter, independent actuation of up to nine OFB microrobots has been demonstrated actuating in saline solution and open reservoir. Also, mesoscale micromanipulation of several micro-object has been demonstrated using multiple OFB microrobots operating co-operatively in conventional cell culturing environment. It shows the compatibility of the OFB microrobot-based micromanipulation system with the cell-culturing environment. Chapter 2, 3 and 4 reports independent actuation of many microrobots in parallel in various medium. However, parallel actuation of many microrobots requires a robust control system capable of transporting the micro-object with the knowledge of the particle present in the workspace. Chapter 5 presents a vision-based closed loop control system which can perform above task.

CHAPTER. 5 VISION-ASSISTED MICROMANIPULATION USING CLOSED-LOOP ACTUATION OF MULTIPLE MICROROBOTS

In previous chapters many microrobots has been actuated independently in parallel performing single or multiple micromanipulation task co-operatively. However, the simultaneous actuation of many microrobots is beyond the capacity of a human operator using a manual control interface. Micromanipulation using the simultaneous actuation of multiple microrobots requires a robust control system to enable independent motion. In addition, the control system required to accurately control and precisely position the OFB microrobots relative to the location of the object under manipulation. This chapter demonstrates a hybrid closed-loop vision-assisted control system capable of actuating multiple microrobots simultaneously and positioning them at precise locations relative to micro-objects under manipulation. A vision-assisted grasp-planning application was developed and used to calculate the necessary trajectories of the microrobots to form cages around micro-objects. The location of the microrobots and the micro-objects was detected at the caging locations using a particle-tracking application that used image feedback for precise positioning. The closed-loop image feedback information enabled the position update of the microrobots, allowing them to precisely follow the trajectory and caging locations calculated by the grasp-planning application. Four microrobots were assigned to cage a star-shaped micro-object using the closed-loop control system. Once caged, the micro-object was transported to a location within the workspace and uncaged, demonstrating the micromanipulation task. This microrobotic system is well-suited for the micromanipulation of single cells.

5.1 Methodology

Individual and independent control of many OFB microrobots in parallel requires automated and sophisticated control, including features such as grasp planning for caging, path planning for obstacle avoidance, and moving along the shortest path to a destination. Moreover, when multiple OFB microrobots are simultaneously actuated, precise positioning and actuation, as well as knowledge of the payload location, will enhance the accuracy and resolution of the micromanipulation. In this work, a hybrid closed-loop control system for an OFB microrobot system was developed. The hybrid system uses an open-loop computer-generated holographic control system (developed in LabVIEW) to generate the optical patterns necessary to actuate

multiple OFB microrobots simultaneously. The closed-loop part of the hybrid system includes an image-processing algorithm (developed in MATLAB) that provides image feedback control; this allows the actuation of multiple OFB microrobots and the knowledge of the locations of the objects

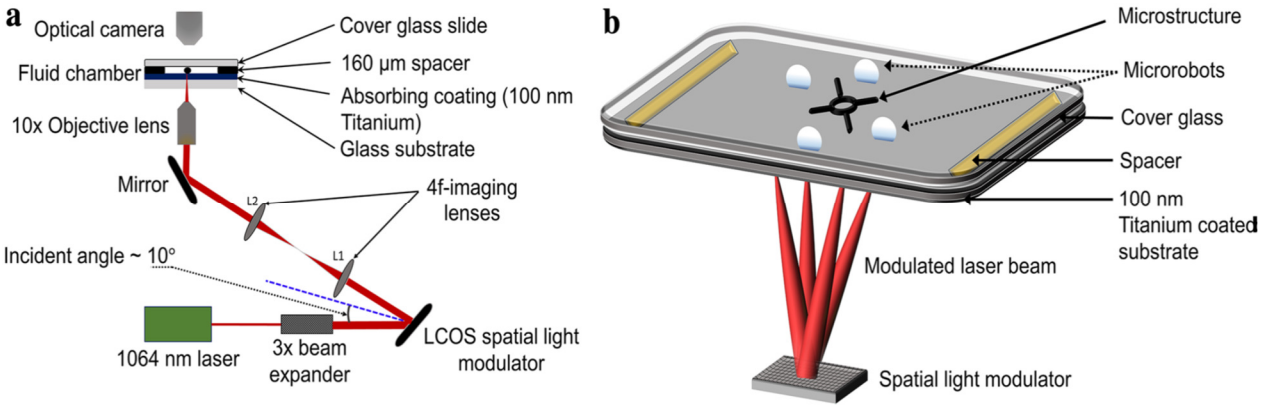

Figure. 5.1 Opto-thermocapillary flow-addressed bubble (OFB) microrobot generation and actuation setup. **a.** The experimental setup for OFB microrobot micromanipulation. **B.** A schematic diagram showing a single laser beam modulated by the spatial light modulator, creating a user-designed pattern on the substrate. Each optical spot on the substrate can generate and actuate an OFB microrobot around the micro-object under manipulation, enabling parallel control of multiple entities.

under manipulation. The control system also includes a grasp-planning algorithm (developed in MATLAB) that determines the shortest path and suitable grasping point of micro-objects. Finally, the closed-loop automatic actuation of four microrobots was demonstrated; the OFB microrobots cooperatively caged a star-shaped SU-8 microstructure and transported it to a desired location within the workspace. The hybrid control system achieved higher accuracy compared to open-loop actuation.

A little variation of the experimental set-up reported in section 2 has been used for closed-loop micromanipulation task. A 1064-nm Nd:YAG, single-mode (TEM00) linearly polarized laser (Laser Quantum, Ventus 1064, 1.5 + W) with a 2-mm beam diameter was expanded using a 3x beam expander (Fig. 5.11a). The expanded beam was incident at approximately 10 degrees on a spatial light modulator (SLM, Hamamatsu, LCOS-SLM X10468- 07) with an active area of 16 mm by 12 mm. The collimated laser beam was modulated by the SLM, which displayed an 800 pixel by 600-pixel computer-generated hologram (CGH) created using a modified version of the

Red Tweezers program [105]. The modulated wavefront containing the user-defined pattern was 4-*f* imaged by placing lens L1 at its focal length from the SLM, and lens L2 at its focal length away from the Fourier plane. A 0.42-N.A. 10X objective lens (Mitutoyo) was placed at the focal length of lens L2, focusing the optical pattern on the light-absorbing coating of the substrate. The 1-mm thick glass substrate is coated with 100 nm of titanium and formed a fluidic chamber when bonded to a 1-mm thick glass slide with a spacer layer consisting of 160-μm double-sided polyimide tape. The liquid medium used in the fluidic chamber was silicone oil (Fisher Scientific, S159-500). A 1600 pixel by 1200-pixel camera (Point Grey Flea3) was used for image capture. One pixel in the image corresponds to 1.02 μm on the workspace.

The spatial light modulator creates the optical pattern desired by the user (Fig. 5.1b). Each optical spot that is focused on the light-absorbing layer of the substrate produces a localized hot spot, vaporizing a small volume of the liquid, and thus generating an OFB microrobot [135]. The thermocapillary flow generated by the temperature gradient and resulting surface tension gradient at the gas–liquid interface of the bubble pulls the OFB microrobot toward the center of the localized hot spot [135].

5.2 Vision-Assisted Closed-Loop Control System

The hybrid closed-loop control system developed in this work has two different parts: the microrobot actuation block developed in LabVIEW, and the image-processing and grasp-planning block developed in MATLAB. The data transfer between the LabVIEW and the MATLAB control blocks was accomplished using the MathScript module of LabVIEW. Figure 5.2 shows the block diagram of the complete control system. The actuation of microrobots was accomplished by the "microrobot actuation block." An open-loop computer-generated holographic (CGH) control system was developed in LabVIEW [29]. An optical spot is represented by a circular spot on the LabVIEW user interface and is maneuvered using manual or automatic control. The user enters the target location of each microrobot, and the MathScript module calculates the navigation parameters, such as initial location, destination, frame rate, and frame size, and passes them to the control application. The control application in LabVIEW then sends the data to the OpenGL Shader hologram engine, which calculates the corresponding hologram using the direct

superposition algorithm. The holograms corresponding to the optical pattern are then displayed on the SLM.

The feedback block was developed in MATLAB (Fig. 5.2). The major function of the feedback loop is to process the camera image of the workspace and output data on the OFB microrobots and the micro-objects under manipulation. The captured image was analyzed by the Hough transform

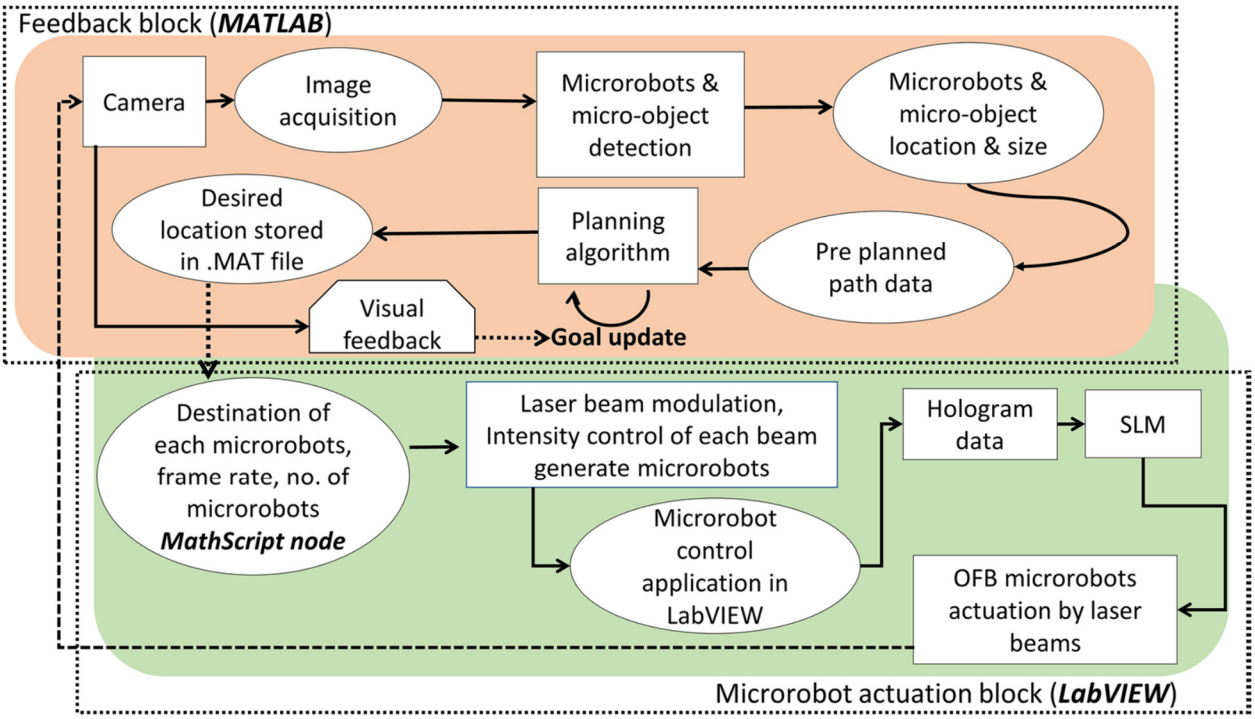

Figure. 5.2 Block diagram of the hybrid vision-assisted closed-loop control system and the microrobot actuation system. The feedback block determines the positions of the microrobots by analyzing the video from the microscope camera and generates trajectories for the microrobots. The microrobot actuation block creates the appropriate optical patterns to move the microrobots.

algorithm, providing the microrobot's locations and sizes, and the micro-object's locations and sizes. The Hough transform detected the shapes in the image, which were then matched to prestored object data. The image data were converted to grayscale and then to a binary image using Otsu thresholding [136] to make the image suitable for the Hough transform. Detection of unwanted objects, such as the white circular spot at the center of Microrobot 1 in Fig. 5.4a, was reduced by defining the size ranges of the objects to detect. A grasp-planning algorithm was also developed in MATLAB to plan the course, speed, and other microassembly-related parameters for

efficient manipulation. Once the microrobot data and micro-object data are available in the MATLAB workspace, the grasp-planning module utilizes user-desired preplanned conditions to calculate the final location of each microrobot for accurate grasping. Once the final destination of each microrobot is calculated, it is saved in a.mat file for subsequent use by the microrobot actuation block. During initiation of the actuation, the destination data from the .mat file are loaded into the MathScript module of LabVIEW.

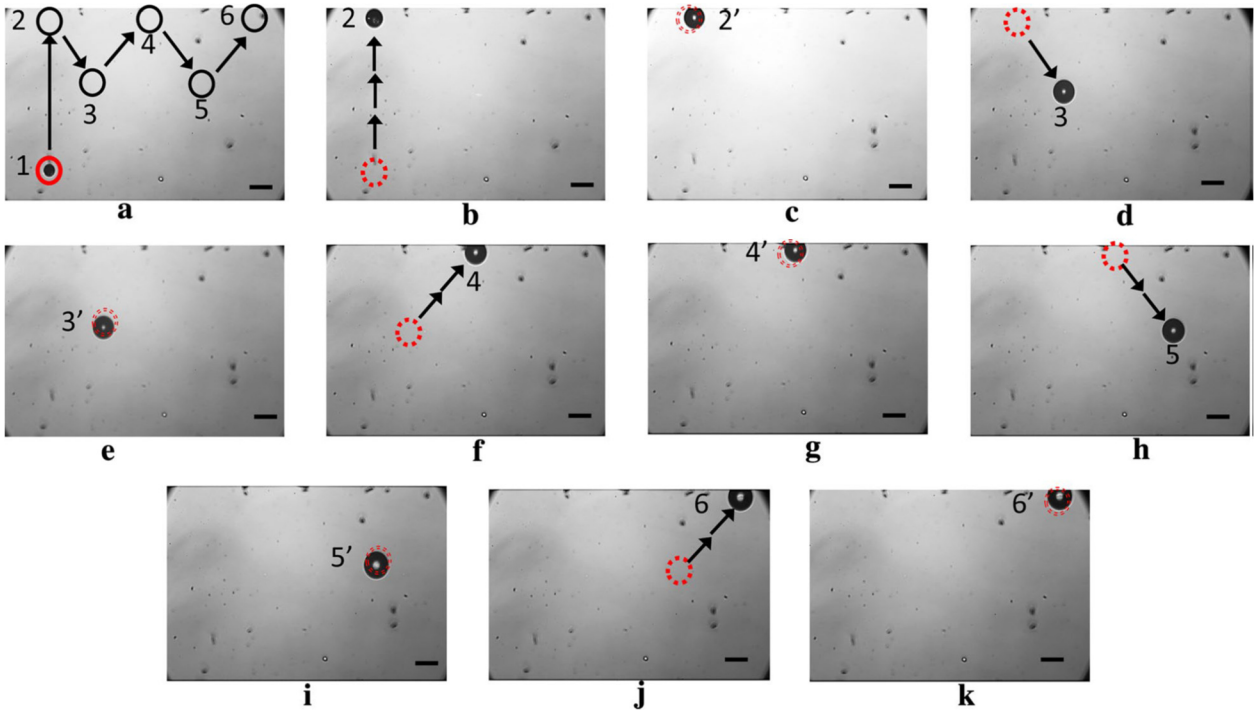

Figure. 5.3 An OFB microrobot was actuated using open-loop control from waypoints 1 to 2 (**a**, **b**), waypoint 2' to 3 (**c**, **d**), waypoint 4' to 5 (**g**, **h**), and waypoint 5' to 6 (**i**, **j**), at velocities of 70, 43, 44, 46, and 39 µm.s^{-1}, respectively. The OFB microrobot location was updated by the vision-assisted closed-loop control at waypoints 2 to 6 (**c**, **e**, **g**, **i**, **k**). The dotted circles mark the previous location of the microrobot. The average size of the microrobot is approximately 85 µm over the duration of the actuation. The scale bar is 100 µm

The hybrid control system described above was used to perform closed-loop actuation of a single microrobot, grasp planning of multiple microrobots for a micromanipulation task, closed-loop actuation of multiple microrobots, and open-loop micromanipulation of a star-shaped SU-8 microstructure.

5.3 Closed-loop Actuation of a Single Microrobot

One of the benefits of the closed-loop control of OFB microrobots is the ability to accurately update the position of the microrobot using data from the image-processing algorithm. Here, we have demonstrated actuation of one microrobot along a preset zigzag path using the hybrid control system (Fig. 5.3). The microrobot was actuated from its initial location to 5 waypoints (waypoints 2–6 in Fig. 5.3) using automated open-loop control sequences. Each point-to-point actuation (1–2, 2–3, 3–4, 4–5, and 5–6; see Fig. 5.3a) consisted of a series of 30 smaller actuation segments, at a rate of 2 Hz. The actuation velocity between the waypoints varied. First, the microrobot was actuated from position 1–2 using open-loop control, a distance of 1048 μm (Fig. 5.3a, b). At location 2 (Fig. 5.3b), the feedback block captured an image of the workspace, detected the physical bubble location within the workspace, and compared it with the intended destination set in the LabVIEW user interface. The microrobot was then moved to a new location (2' in Fig. 5.3c) to correct for the positioning error. Similarly, the microrobot position was determined by the feedback block at each waypoint (3–6 in Fig. 5.3d, f, h, j), compared with the preset destination in LabVIEW actuation block, and then moved to minimize the difference between the preset destination and the actual position (3', 4', 5', 6' in Fig. 5.3e, g, i, k). The position error calculated by the feedback block at 2', 3', 4', 5', 6' in Fig. 5.3 was 5.25, 14.1, 5.1, 16.5, and 2.8 μm, respectively. The position error was then reduced to approximately 1 μm after the microrobot locations were updated using the hybrid closed-loop control system.

Closed-loops control allows microrobot actuation error detection and correction**.** The hybrid control system changes the position of the laser spots with the knowledge of microrobot location. In contrast, open-loop control moves the optical pattern even if the microrobot under actuation does not follow the location of the laser spot. This is demonstrated in Figure 5.4. An OFB microrobot was intended to be actuated from its initial position to the location marked by a dotted black circle, 1200 μm away (Fig. 5.4a). The actuating laser spot was translated at approximately 400 $\mu m.s^{-1}$, but the microrobot was unable to move at this speed (Fig. 5.4b). The image-processing function of the feedback block detected that the microrobot failed to follow the optical spot, and identified the current location of the microrobot (Fig.5. 4b). The laser spot was translated back to the location of the microrobot, and another attempt was made to actuate the

microrobot to the destination at a lower translational velocity of approximately 60 µm.s^{-1}, resulting in successful movement to the destination (Fig. 5.4c). This type of actuation error may occur for various reasons, such as a high translational velocity of the optical spot, insufficient power at the actuating beam, and collision of the microrobot with obstacles. This hybrid closed-loop control system can detect and recover from these actuation errors.

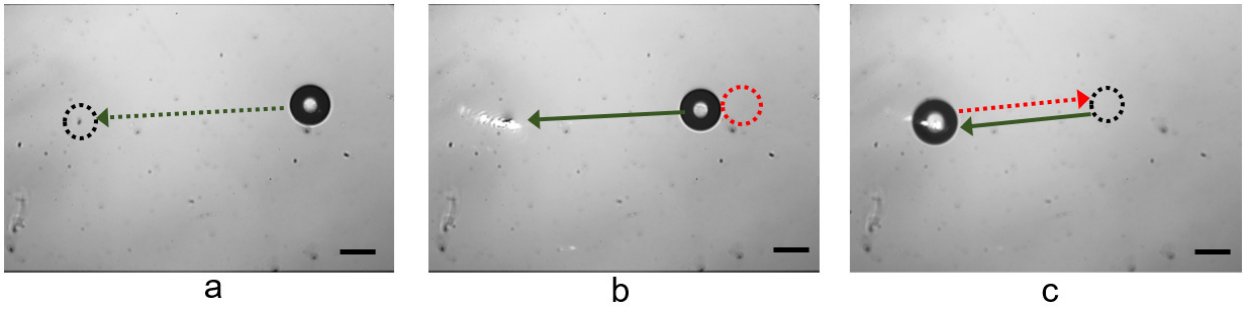

Figure. 5.4 Microrobot actuation error detection and correction using the hybrid closed-loop control system. (a) The microrobot was to be actuated to the destination marked with the black dotted circle. (b) The laser spot was translated at high speed to the target location (following the path of the green arrow), leaving the microrobot behind. The microrobot was actuated 187 µm from its initial position (dotted red circle) in the direction of the laser movement, but failed to follow any further. (c) The feedback block detected the microrobot position and passed it to the actuation block. The actuation block translated the laser beam towards the microrobot, as indicated by the red dotted arrow. Then the microrobot was actuated to the destination a a lower speed, along the path indicated by the green arrow.

5.4 Grasp Planning and Collision-Free Path Determination

Path planning refers to determining a collision-free path for a moving object among obstacles [137]. In this work, a grasp-planning algorithm determines the geometry and location of a microrobot and a micro-object payload. The output of the grasp-planning algorithm is sequences of microrobot locations that form a trajectory from its initial position to its goal position, which is in reference to the payload. There were no obstacles present in the workspace when caging the payload, but the algorithm is capable of determining collision-free path about obstacles. (Fig. 5.6). The grasp-planning algorithm was used to create a cage of four OFB microrobots around a star-shaped SU-8 microstructure, and transport the object to another location. The star-shaped microstructure consisted of four arms, each 59 µm in length, and a hollow circular center with an inner diameter of 62 µm. The width of the wall around the circular center and the width of the arms

were approximately 66 μm. The thickness of the SU-8 was 50 μm, and the structure had an approximate mass of 2.35 μg.

Initially, four OFB microrobots were generated at random locations around the micro-object (Fig. 5.5a) by momentarily increasing the optical power in each spot using the actuation block (Fig. 5.2). The feedback block then detects the location and size of the microrobots and the structure. The grasp-planning algorithm uses the location of the structure within the workspace to calculate the caging positions (1′, 2′, 3′, and 4′ in Fig. 5.5a) at user-defined equidistant locations around the micro-object. The grasp-planning algorithm allows the adjustment of the caging locations based on visual feedbackand the shape of the object. In this experiment, the caging formation was rotated clockwise (Fig. 5.5a–c) to allow a better grasp of the micro-object. The final caging configuration (Fig. 5.5d) puts the microrobots in positions that will allow them to grasp in between the arms of the micro-object when the caging formation is contracted.

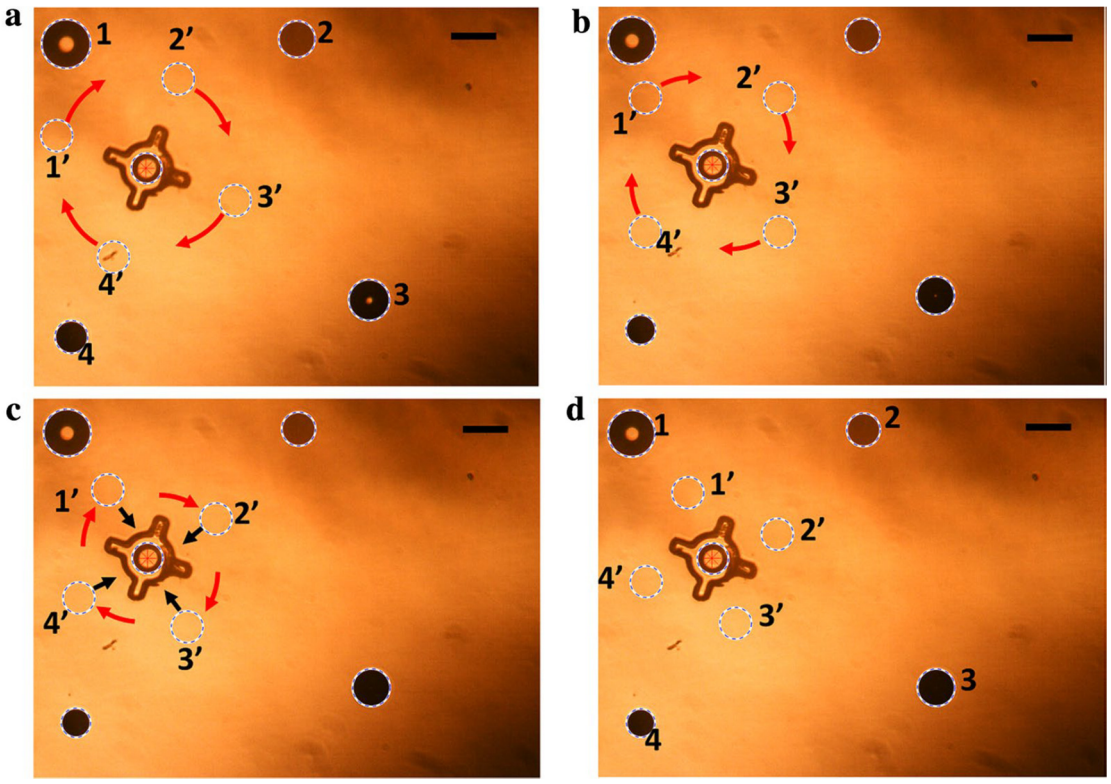

Figure. 5.5 Determining the optimum caging location of the microrobots around a payload using the grasp-planning module. a. The image-processing algorithm determines the location and size of the randomly located microrobots (labeled 1–4) and the micro-object. The path-planning algorithm calculates the caging positions, marked

using dotted circles numbered 1′ to 4′. The initial caging location was set 307 µm away from the center of the micro-object. **b.** The caging formation is rotated 10 degrees clockwise. **c.** The formation is rotated another 10 degrees and contracted 51 µm using the grasp-planning module to position the microrobots between the arms of the star-shaped structure. **d.** The final caging locations calculated by the grasp-planning algorithm are marked with dotted circles labeled 1′ to 4′. The size of Microrobots 1, 2, 3, and 4 is 156, 114, 126, and 101 µm in diameter. Scale bar: 150 µm

The path planning module of the hybrid control system is capable of determining a collision-free path to a destination. Figure 5.5 demonstrates the calculation of a collision-free path for Microrobot 1. The feedback block detected the locations and shapes of the objects in the workspace, including the inner circular feature of the micro-object (blue circle in Fig. 5.6). The destination location of Microrobot 1 is marked by the black dotted circle; the shortest path from the initial location Microrobot 1 to the destination is obstructed by the micro-object. The path-planning algorithm takes the object locations, the destination of Microrobot 1 as entered by the operator, and the minimum collision-free distance (MCD) set by the operator as inputs for calculating the collision-free path. The MCD was set to 2 times the radius of the blue circle marking the micro-object. The collision-free path was calculated from the current location towards the destination along a linear trajectory until the microrobot reaches the MCD (P1 in Fig. 5.6). At P1 the path continues along a curved path towards the destination, maintaining the MCD from the center of the obstacles until it reaches P2. From P2 the path runs on the shortest straight line towards the destination, marked with a black dotted circle.

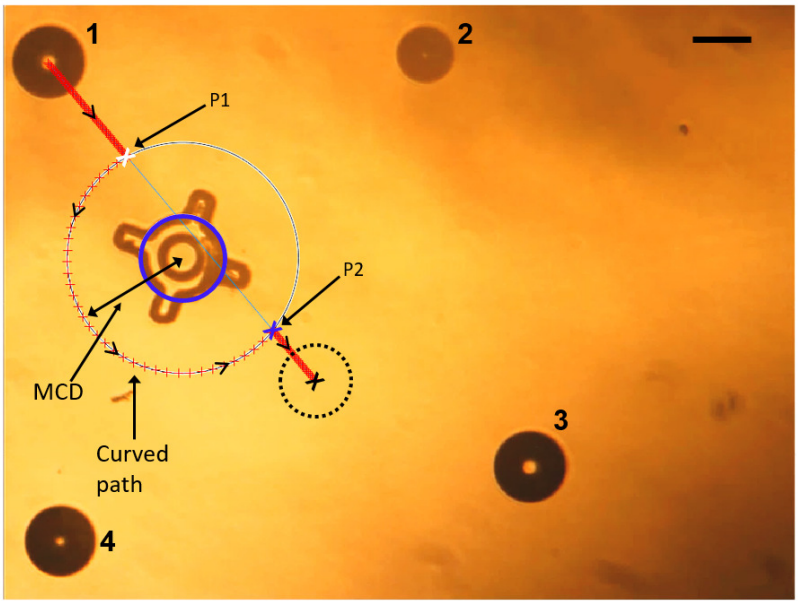

Figure. 5.6 Collision-free path calculation by the path-planning algorithm. The path was calculated for Microrobot 1 from its current position to the destination marked with dotted black circle, while avoiding the obstacle marked with a blue circle. The calculated path consists of linear paths and a curved path to avoid the obstacle.

5.5 Hybrid Closed-Loop Actuation of Multiple Microrobots

The caging formation (1', 2', 3', and 4' in Figure 5.5d), calculated by the grasp-planning algorithm of the feedback block sets the destination location for the individual microrobots. These positions were saved in a .mat file and subsequently loaded into the MathSript module of the LabVIEW actuation block. However, the caging locations require a transformation to match the coordinate system of the actuation block. Once the transformed final destinations of the microrobots are serially loaded into the MathScript module from the .mat file, the destination of the each microrobot is mapped to the corresponding locations on the LabVIEW user interface. In this experiment, the microrobots numbered 1, 2, 3, and 4 were assigned the caging locations 1', 2', 3' and 4' (Figure 5.5d) as their destination in actuation block.

Figure 5.7 shows the open-loop actuation of four microrobots from their initial position to the caging location. Microrobots 1, 2, 3, and 4 were simultaneously actuated at velocities of 19 $\mu m.s^{-1}$, 29.6 $\mu m.s^{-1}$, 44.1 $\mu m.s^{-1}$, and 31.83 $\mu m.s^{-1}$, respectively, using the actuation block (Figure 5.7a-c). Here, the simultaneous actuation of multiple microrobots with different speeds demonstrates a capability of the microrobot control system: parallel, uncoupled movement of microrobots along trajectories that vary in direction and distance traveled during the same actuation time. The microrobot actuation took 15 seconds. Figure 5.7d shows the path of each microrobot from its initial position to the caging location. Here, the simultaneous actuation of multiple microrobots with different speeds demonstrates a capability of the microrobot control system: parallel, uncoupled movement of microrobots along trajectories that vary in direction and distance traveled during the same actuation time.

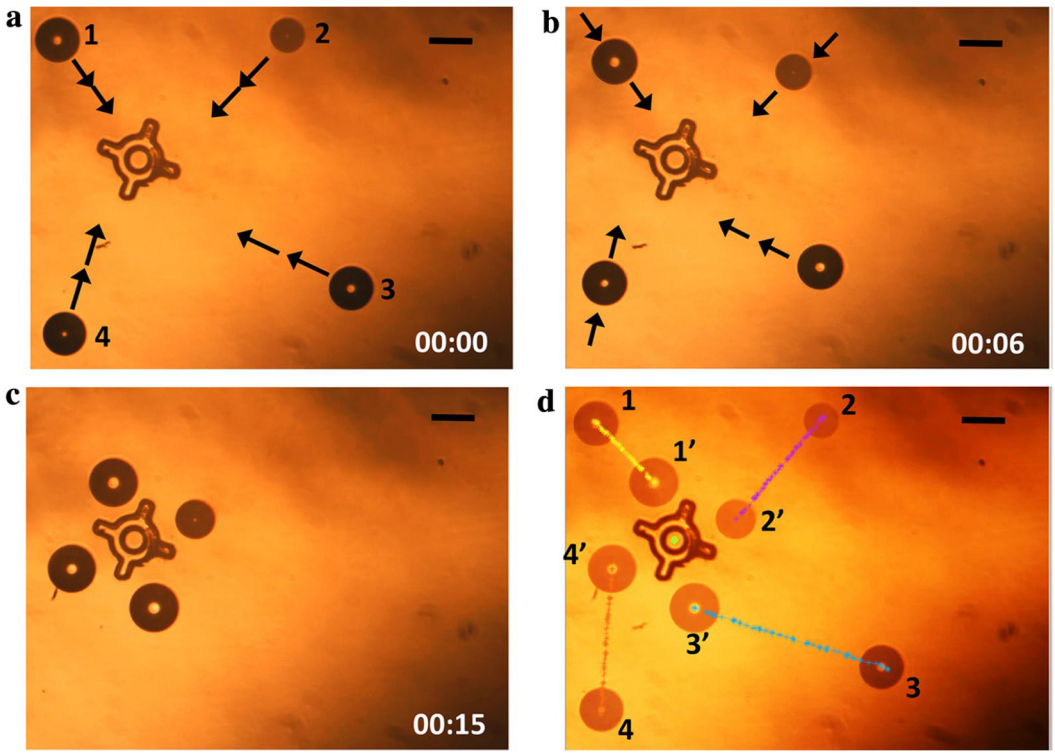

Figure. 5.7 Automatic actuation of four OFB microrobots from their initial positions to the caging formation. (a) Microrobots approaching to the caging formation. (b) Each microrobot is actuated simultaneously at different speeds. (c) Microrobots positioned around the micro-object. (d) Since the microrobots were actuated at different speeds, they all arrive at their caging positions at the same time, despite the differences in the length of the actuation paths. The average size of the microrobot 1, 2, 3, and 4 is 159 µm, 132 µm, 161 µm, and 159 µm in diameter. Scale bar: 150 µm. Time format: minutes:seconds.

Figure 5.8 shows the OFB microrobots at the caging positions. The image-processing algorithm determined the locations of the microrobots and compared them to the caging locations calculated by the grasp-planning algorithm. Figure 5.7a shows the locations of Microrobots 1, 2, 3, and 4 as determined by the image-processing algorithm (white dotted circles), and the desired caging locations set by the grasp-planning algorithm (red circles). The feedback block calculates the error between the actual location of the microrobot and the desired caging position, and calculates the new microrobot destination to minimize the error. Microrobots 1, 2, 3, and 4 in Figure 5.7a were 27 µm, 24.7 µm, 14.28 µm, and 21.5 µm away from their desired caging positions, respectively. This information is passed to the MathScript node of the actuation block, which moves the microrobots to the new destinations (Figure 5.7b). The microrobots were actuated to their new

positions at speeds of 5.4 μm.s^{-1}, 4.94 μm.s^{-1}, 2.86 μm.s^{-1}, and 4.3 μm.s^{-1} for Microrobots 1, 2, 3, and 4, respectively (Figure 5.7b).

After updating the location using open-loop actuation, the physical location of the microrobot within the workspace was determined by the image-processing algorithm of the feedback loop, as shown in Figure 5.8c. The red circles in Figure 5.8c are the caging position set by the grasp planning algorithm at the beginning of the actuation. In Figure 5.8c, the Microrobots at 1', 2', 3' and 4' were 8 μm, 12 μm, 5 μm, and 19 μm away from their desired locations, corresponding to a reduction in the position error of approximately 50 %.

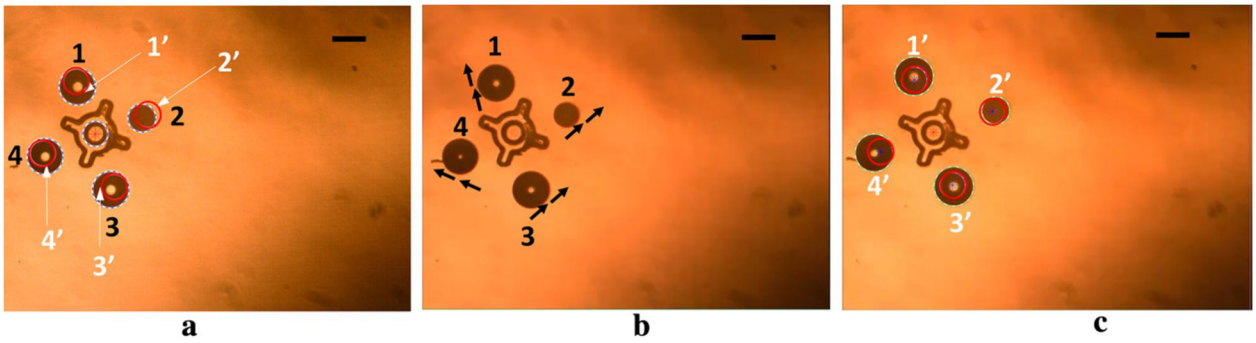

Figure 5.8. Closed-loop position updating of the microrobots at the caging formation. (a) Image captured by the feedback block showing the position error between the desired location of the microrobot (indicated by the red circle marked with white arrows) and the physical location of the microrobots (marked with the dotted white circle). (b) Microrobots are actuated to the new destination, minimizing the position error. (c) Microrobots actuated to the updated caging formation, resulting in reduced position error. The average size of the microrobot 1, 2, 3, and 4 is 149 μm, 108 μm, 150 μm, and 144 μm in diameter. Scale bar: 150 μm.

5.6 Micromanipulation

The hybrid closed-loop vision-assisted control system allowed an accurate placement of a caging formation, as described above. Figure 5.9a shows the open-loop actuation of a microrobot matrix approaching to grasp a micro-object for manipulation. The matrix of microrobots was manually controlled by the actuation block using user input. The object was grasped by contracting the microrobot formation with an average speed of 7.6 μm.s^{-1} (Figure 5.9b). After grasping, the microrobot formation attempted to transport the micro-object in the positive *x*-direction. However, the micro-object was stuck to the floor of the fluid chamber, resulting in the dislocation of the microrobots from their actuation patterns (Figure 5.9c). This phenomenon is more obvious for

Microrobots 2 and 3, marked with red arrows in Figure 5.9c, as they were moved in the positive *x*-direction and left the micro-object behind.

To free the micro-object from the surface, the formation of the microrobots were rotated to create a torque on the object while maintaining a firm grasp (Figure 5.9d). The twisting of the object helped to overcome its stiction, and the micro-object could then be transported. The micro-object was transported along various trajectories (Figure 5.9e) and at various speeds up to approximately 90 $\mu m.s^{-1}$. A graph of the planned trajectory and completed trajectory during the micro-object manipulation is included in. Upon completion of the micro-manipulation, the micro-object was released by expanding the microrobot formation (Figure 5.9f).

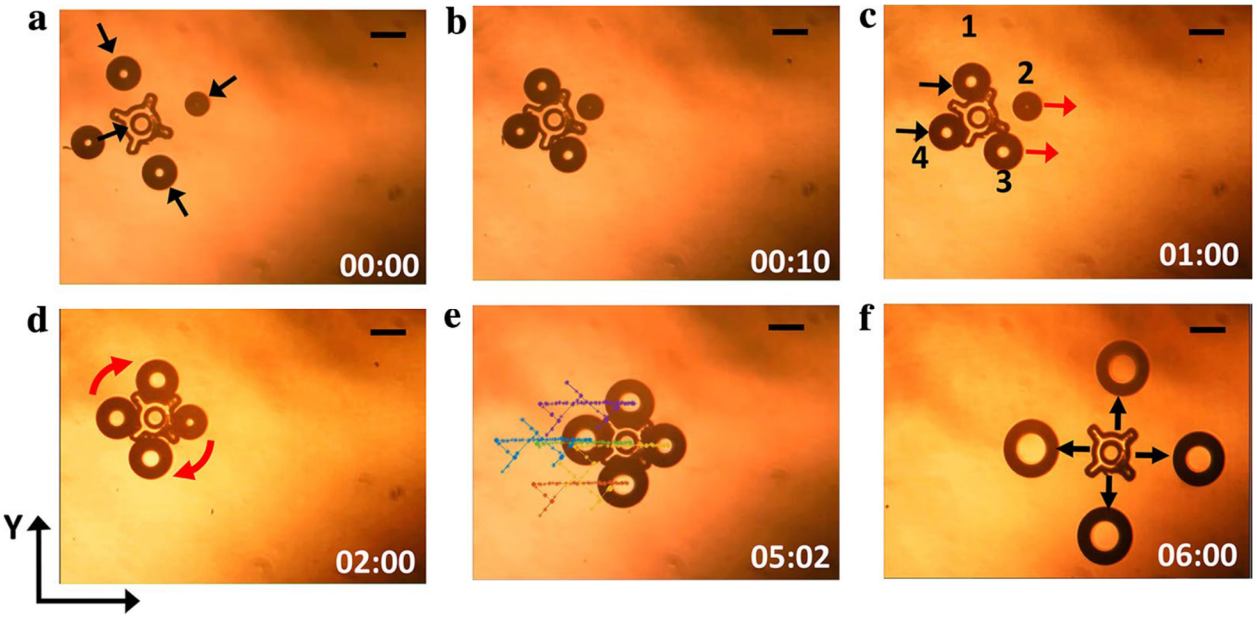

Figure 5.9. Micromanipulation by grasping using open-loop actuation. (a) Microrobots move from the initial caging formation to grasp the micro-object. (b) The microrobots have grasped the micro-object. (c) The formation of four microrobots is attempting to move the micro-object in the x-direction, but fail due to the object's stiction with the substrate. Microrobots 2 and 3, marked by the red arrows, move right, leaving the micro-object behind. (d) A clockwise twisting motion was used to ease the stiction of the micro-object. (e) The micro-object was manipulated along a random trajectory at various speeds. (f) The payload is released within the workspace by expanding the microrobot formation using open-loop actuation. The average size of the microrobot 1, 2, 3, and 4 is 191 µm, 167 µm, 194 µm, and 195 µm in diameter, respectively. Scale bar: 150 µm.

5.7 Discussion and Conclusion

The hybrid closed-loop vision-based control of OFB microrobots with open-loop actuation has leveraged the functionality of two different platforms to perform the micromanipulation tasks. This integration of MATLAB and LabVIEW utilizes the hardware support and rapid configuration of LabVIEW and the advantages of MATLAB's processing of complex image data. Aside from providing more precise manipulation, closed-loop position updates allow the use of standard macroscale robotic functions like grasp planning, collision avoidance and detection, grasping, and payload detection and delivery. Also, the hybrid control allows to detect the failed actuation of individual microrobots (Fig. 5.4). Moreover, the OFB microrobot system, which is capable of the independent actuation of many microrobots, utilizes the vision-based automatic actuation for the simultaneous participation of multiple microrobots in micromanipulation, as it is difficult for a human operator to control many microrobots. In this work, the OFB microrobot system enabled a team of microrobots to transport a large object, which is not possible with a single microrobot. This was quantified in previous work, as it was observed one or two microrobots could produce limited rotational movement of a SU-8 microstructure, but no translational movement. Three or four microrobots were necessary to translate the micro-object [1].

The closed-loop position update increased the accuracy of the caging locations by 50 % compared to one iteration of open-loop actuation. The results suggest that multiple iterations of closed-loop position updating may reduce the error; this needs to be investigated further. The causes of the position error during open-loop actuation can be broadly divided into two categories: system error and mechanical error. The system error is due to the spatial resolution of the SLM and any misalignment of the optical elements. The mechanical error is caused by the misalignment of the image coordinates compared to the LabVIEW user interface coordinates. This misalignment exists due to the mechanical adjustment of the camera position when attempting to match to the LabVIEW coordinates. The software-defined coordinates in LabVIEW were considered the ideal coordinates, and the camera was adjusted by hand to so a single pixel on both the MATLAB image processing module and the LabVIEW actuation module had the same dimensions. Despite the careful adjustment, an error of approximately 6 to 8 px was present; this was quantified by taking multiple measurements of a stationary micro-object.

The closed-loop control system helps with the system error, but is unable to correct for the mechanical error. The average error calculated during open-loop actuation (Figure 5**.7**) was 21.87 µm per microrobot. The closed-loop position update reduced the average error to 11 µm per microrobot.

A micro-object was manipulated in different directions along random trajectory by grasping with four microrobots (Figure 5.9e). Figure 5.10 shows the trajectory of all four microrobots, with measured locations marked with asterisks. All four microrobots were grasping the micro-object, resulting in similar trajectories. The planned trajectory of Microrobot 2 (Figure 5.9c & e) is plotted in Figure 5.10 using a black dotted line. The error between the planned (black dotted line) and the actual (yellow line) trajectory has a maximum approximately 15 µm, suggesting that closed-loop position updates at certain waypoints is sufficient to maintain an acceptable error range on the order of 10 µm.

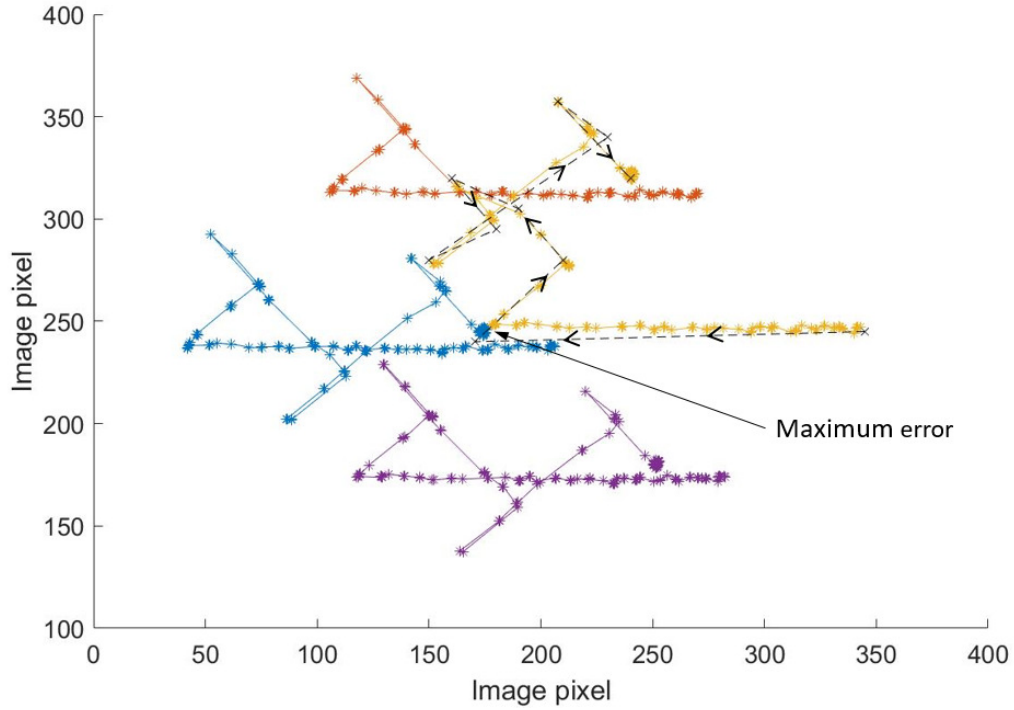

Figure. 5.10. The measured trajectory of four microrobots actuating grasping a micro-object (lines with asterisks) and the planned trajectory of one of the microrobots (black dotted line).

The positioning tolerance of the micromanipulation varies with the size of the objects under manipulation and the type of manipulation. For example, stable caging requires the microrobots to be placed at a distance smaller than the payload size from each other [138, 139]. The caging of the 300-μm-diameter star-shaped micro-object using 130-μm-diameter microrobots required the microrobots to be placed less than 300 μm from each other for stable trapping, and at least 130 μm (one body length) apart to avoid merging of the bubble microrobots. Thus, the calculated microrobot separation of 280 μm with ±10 μm position tolerance satisfies these conditions. The hybrid closed-loop control system was able to reduce the average position error from 21.9 μm to 11 μm, satisfying the position tolerance for this micromanipulation task.

The image feedback of the proposed hybrid control system can detect more than four particles at once; it can detect as many distinct objects that can fit in the camera field of view. The control algorithm is also not limited to four particles; it can set destinations and waypoints for the amount of objects detected in the workspace. The open-loop control part of the hybrid system has been demonstrated to control an array of 50 OFB microrobots [1], and this system can control at least the same amount of microrobots at once.

In this chapter, the vision-based closed-loop position update was executed at the waypoints for single microrobot actuation and at the caging locations for multiple microrobot actuation, instead of iteratively after each camera video frame. The closed-loop position update was not implemented after each frame since the position errors per frame were usually less than one micron. Moreover, the processing time for the image analysis of the high-resolution image (1600 px by 1200) at each frame would increase the overhead on the overall computation process and time.

In chapter 3, chapter 4, and chapter 5 the performance of OFB microrobot is demonstrated. Compared to the other microrobot driven micromanipulation OFB microrobot system is better in several performance matrices. Table I compares popular microrobot systems used for bio-micromanipulation. The OFB microrobots reported in this dissertation are capable of actuating the maximum number of microrobots independently in parallel compared to other microrobots.

TABLE I ACTUATION MECHANISMS FOR MICROROBOTS

Actuation mechanisms	***Achievable velocity***	***Resolution***	***Multiple microrobots****
Magnetic	~ 300 mm.s^{-1} [35]	~ μm [140]	Up to 3 [12]
Electric	~ 35 mm.s^{-1} [16]	~ 3 μm [17]	Up to 5 [17]
Biohybrid	~ 0.8 mm.s^{-1} [19]	~ μm [20]	Not yet [21]
Optothermal	~ 1 mm.s^{-1} [28]	~ μm [34]	Up to 50 [1]
Multiple forces	~ 8 mm.s^{-1} [26]	~ 0.05 μm [141]	Up to 2 [26]

*This category refers to the number of microrobots that can be simultaneously moved along unique trajectories

This chapter demonstrates a hybrid closed-loop vision-assisted control system capable of actuating multiple microrobots simultaneously and positioning them at precise locations relative to micro-objects under manipulation. The grasp-planning application was used to calculate the necessary trajectories of the microrobots to form cages around micro-objects. The position of the microrobots and the micro-objects was detected using a particle-tracking application developed in MATLAB. The closed-loop image feedback information has the potential to enable other microrobot maneuvers such as path planning, and collision avoidance. Chapter 2, 3, 4, and 5 describes the OFB microrobot driven micromanipulation systems, an application of microfluidics for micromanipulation. Chapter 6 presents a different use of microfluidics precisely positioning the liquid-metal conductor as a tuning element for the reconfigurable electronics.

CHAPTER. 6 LIQUID METAL TUNABLE MRI RECEIVE COIL

Medical image acquisition devices such as magnetic resonance imaging (MRI) provide critical anatomical and functional information for diseases diagnosis and patient treatment. The recent development of quantitative image analysis methods has improved the quality of data extracted from the images. However, the image quality and results vary with the signal-to-noise ratio (SNR). Poor SNR limits the spatial resolution, and degrade the image quality. To overcome this MRI data needs to be recorded for a more extended period, which makes the procedure prone to motion artifact because the patient may not be able to remain still for extended periods of time. The SNR becomes worse when receive coil is rigid and does fit the area of the examination well. Also, the padding used for patient comfort exacerbates the performance of receive coil. This chapter proposes a liquid-metal based tunable and flexible MRI receive coil element which can provide good fit over the body curve of the patient and tune for the appropriate receive frequency. One antenna element was fabricated using the liquid-metal tunable capacitor. This liquid-metal based tunable capacitor has the potential to make a flexible and tunable MRI receive coil with high SNR.

6.1 Introduction

High SNR is critical for faster MRI data acquisition. MRI scanning is relatively slow and can take 10 to 100 minutes depending on the part of the body scanned [142]. The scanning time increases if the patient moves during the scanning process. Scanning for longer duration increases the SNR. However, longer scanning limits the spatial resolution, diagnostic image quality and typically results in long acquisition times that are prone to motion artifacts. Recent developments in image reconstruction such as parallel imaging [57] and compressed sensing [58] resulted in 50% reduced scanning time compared to full scanning [57]. The image quality is limited by the SNR obtained during the short scan. Other approaches to increasing SNR includes higher-field scanners [59], use of contrast agents [60], and the better receive coils [62]. Better receive coils resulted in higher gain compared to other methods [61]. An MRI procedure starts by placing the patient in the large static magnetic field; hydrogen protons align with the externally applied static magnetic field to create a net magnetization vector. Radio-frequency (RF) pulses are applied at the resonance frequency of the proton spin. The RF pulses excite the magnetization, protons can absorb energy and jump to a higher energy state. Now, the gradient of the magnetic field is used to encode spatial

information by changing the resonant frequency in three-dimensional space. When the RF signal is stopped, energy is given off as the spins move from high to low energy states. The absorbed RF energy is retransmitted at the resonance frequency and can be detected with RF antennas or "receive coils" placed around the patient. These received RF signals, which represent partial coded information, are amplified, digitized, stored, and processed to become the MR images. This procedure is repeated with a different gradient of the magnetic field leading to long exam time, and make the acquisitions susceptible to motion artifacts. The use of receive coil arrays improves for additional SNR, and parallel imaging can remove the above limitations [58, 64]. The receive coils and arrays are built for specific areas of the body. Currently, the coils are made of high-quality rigid electronics component packaged using stiff medical-grade materials. Figure 6.1 shows a receive coil arrays used for head and chest imaging on an adult. This chest and head array are made of rigid materials. If the patient is a smaller person or child, there will be a gap between the patient body which will reduce the SNR. Therefore, a good coil fit is critical for high SNR images. One example is in Figure 6.1b, where two cervical spine images are compared obtained by a flexible coil with a good fit to the patient (right) and the other obtained using a conventional rigid coil (left). This image clearly shows better performance can be obtained using a flexible receive coil. Previously, flexible receive arrays have been demonstrated using conductors sewn into fabric [64], screen printing on flexible substrates [65], a mercury-based conductor [66], electro-textile-based RF coils [67], and semi-flexible copper tape [68]. These techniques provide flexible, light, and scalable manufacturing of RF coils with relatively high SNR performance. However, none of the technique provides tunability of the antenna element during the MRI procedure. Here, we hypothesize that non-toxic liquid metal has the potential to build flexible, lightweight, and tunable RF receive coil arrays which can be tuned real-time for high SNR. We fabricated the prototype of one antenna element on PET substrate where the fixed capacitors were fabricated with copper tape and the tunable capacitor was fabricated with non-toxic Gallium based liquid-metal alloy. In addition, a tunable liquid-metal tube capacitor was fabricated with high tuning ratio.

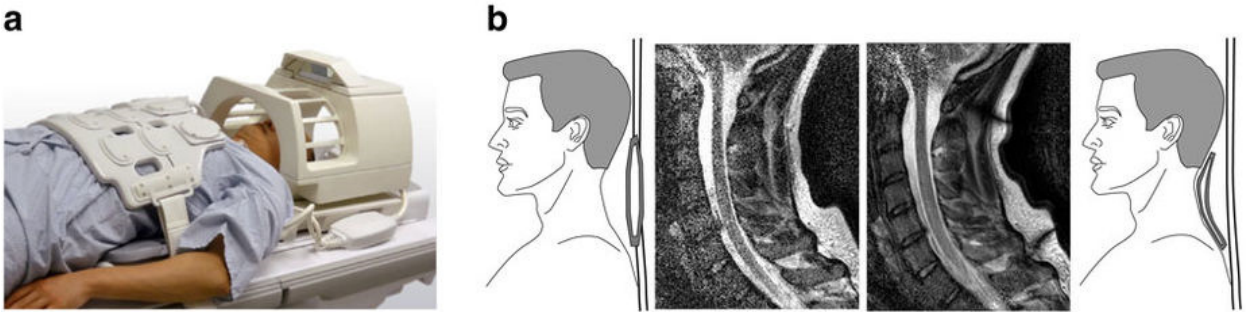

Figure. 6.1 RF receive coil arrays resulted in better image SNR while in contact with experimented area. (a) Conventional rigid MRI receive arrays on the chest and head of a patient. (b) MRI image of cervical spine showing low-SNR when scanning keeping the coil 8 cm away from the spine (left) and high SNR when placed against the skin (right). (Reprinter with permission) [65].

6.2 Antenna Element Prototype

The prototype of the MRI receive coil element was designed and fabricated for 3.0 T scanners. A receive coil is primarily a loop of conductor integrated with the capacitors. The L-C circuit determines the resonant frequency of the antenna loop. The size of the loop is fixed, and its geometry is designed for the required inductance. Figure 6.2 shows the schematic of the antenna element. The capacitor C1, C2, and C3 are fixed value capacitor fabricated sandwiching PET (polyethylene terephthalate) as a dielectric [143] in between two pieces of copper tape.

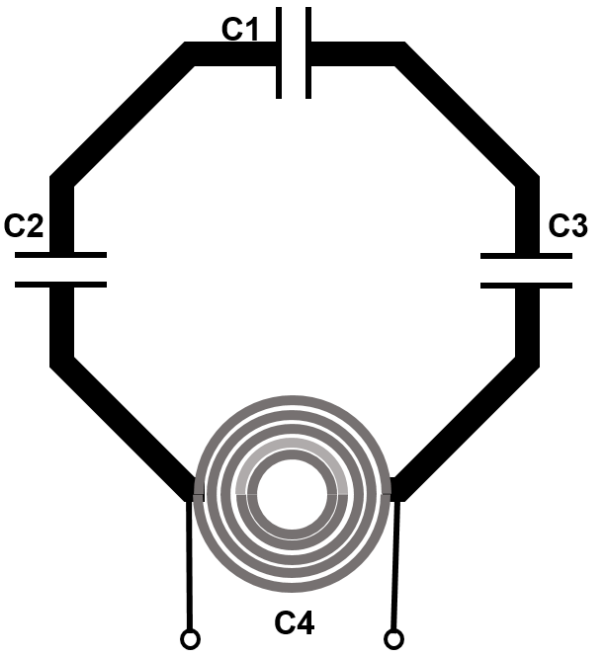

Figure. 6.2 Schematic of a coil loop. Here, matching capacitors C_1, C_2, C_3 are connected equidistant form each other, and liquid-metal tunable capacitor C_4 is connected in parallel.

The value of the fixed capacitors was chosen to match the input impedance of the antenna to 50Ω. The copper tape and the PET was 60 μm and 120 μm thick, respectively. On the other hand, capacitor C4 (Fig. 6.2) is a liquid-metal tunable coil capacitor which was connected in parallel to the other capacitors. C4 can be tuned in real-time to select the resonant frequency of the antenna, discussed in Section 6.3. The coil was designed to be octagonal with a diameter of 8.7 cm [65], with a conductor width of 0.5 cm, and was fabricated with copper tape on PET. Figure 6.3 shows the photograph of the coil. The liquid-metal capacitor C4 was designed for tuning the resonant frequency of the coil from 100 MHz - 220 MHz, covering the Larmor frequency (127 MHz) used in 3.0-T MRI.

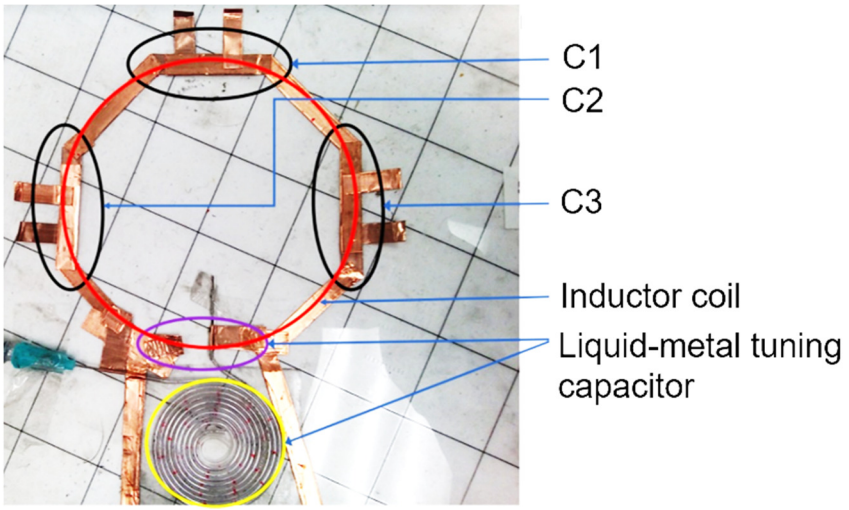

Figure. 6.3 Photograph of a prototype coil. Inductor loop and the capacitors are shown on the figure.

6.3 Liquid-Metal Tunable Capacitor

A liquid-metal tunable capacitor was designed for the flexible MRI receive coil mentioned in above section. This work uses the nontoxic liquid metal Galinstan, which is highly conductive (3.46×10^6 $S.m^{-1}$) and remains a liquid from −19 to 1300°C [144]. Four types of liquid-metal-based tunable capacitors with a high tuning range are demonstrated. The capacitors are easily fabricated by placing a pair of liquid-metal-filled tubes in contact with one another. Tunability is achieved by varying the length of the liquid metal in one of the tubes using a mechanical pump. Four different structures are demonstrated: parallel-tube, folded-tube, coil, and spiral capacitors. The highest measured tuning ratio is 42:1, and the highest change in capacitance per unit length of the pumped liquid metal is 0.07 $pF.mm^{-1}$.

In this work, commercially available tubing was filled with liquid metal and placed in parallel, thus forming the basic structure of a capacitor. With liquid metal serving as the conductive element, the tubing material served a threefold purpose: containing the liquid metal, shaping the liquid metal, and serving as the dielectric of the capacitor. Capacitive tunability was achieved by varying the length of the liquid metal using mechanical pressure. Furthermore, the flexible nature of the capacitor tubing was exploited to create four distinct capacitor structures: parallel-tube, folded-tube, coil, and spiral. Although mechanical pressure was used to tune the capacitors in this work, electrical actuation of liquid metal could be used to make these tunable capacitors easier to integrate with other electrical components [52][145]. The liquid-metal capacitors presented here

are easily made by hand, and can be resized depending on the required capacitance tuning range. The capacitors are flexible and conformable to curved surfaces. The capacitors demonstrated here had a measured tuning ratio of 42:1, higher than the other tunable capacitors mentioned above. Furthermore, the capacitance of the liquid-metal microfluidic capacitors varies linearly over the range measured here, suggesting that even larger tuning ratios are possible. The major trade-off is that larger capacitor footprints are required to increase tunability.

6.3.1 Material and Methods

The capacitors were fabricated using a pair of polyvinyl chloride (PVC) tubes with a dielectric constant of 3.2, an inner diameter of 0.51 mm, and an outer diameter of 1.52 mm (Tygon S-54-HL AAQ04103). Tube 1 and Tube 2 were placed in contact on a sheet of polyimide tape (Fig. 6.4a). Tube 1 was filled with liquid metal, which contacted the 23-gauge copper electrode 1 at one end of the tube. One end of tube 2 was attached to a syringe pump through a 23-gauge stainless-steel syringe needle, which also served as an electrode (electrode 2 in Fig. 6.4a). An impedance analyzer (Hioki 3570) was connected at electrode 1 and electrode 2 to measure the capacitance by sweeping a 1 Vp-p AC signal from 1 kHz to 5 MHz. The liquid metal in tube 2 was incrementally filled to change the capacitance. Various capacitor geometries were explored, as described below.

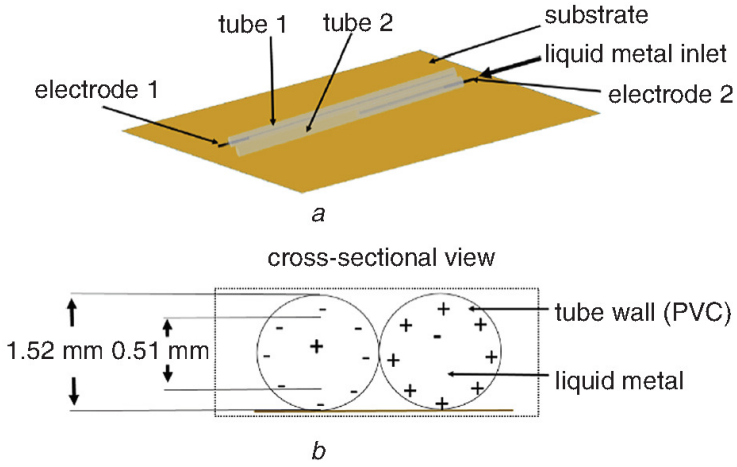

Figure. 6.4 Liquid-metal parallel-tube capacitor

6.3.2 Tunable Liquid-metal Parallel-tube Capacitor

The simplest tunable liquid-metal capacitor structure consisted of two parallel tubes (Fig. 6.4). A pair of 260 mm-long PVC tubes was used to form a tunable liquid-metal parallel-tube capacitor using the methods mentioned above. A significant increase in capacitance was measured as more liquid metal was pumped into tube 2, increasing the overlap of the liquid metal between tube 1 and tube 2 (Fig. 6.5). The length of the liquid metal in tube 2 was changed from 1 to 260 mm, resulting in a tuning range of 42:1 (C_{min}=0.16 pF, C_{max} = 6.7 pF). The measured Q-factor was 10 at 1 MHz. The Q-factor can be improved by using tubing with higher dielectric constant and dielectric strength. The tuning range can be extended by increasing the length of the tubing. To quantify the tuning performance of the various microfluidic capacitors described here, the change in capacitance per change in length of liquid metal in the tubing is calculated using (C_{max}−C_{min})/(length of the liquid metal). This capacitance per unit length of actuation was 0.0252 pF.mm^{-1} for the parallel-tube microfluidic capacitor.

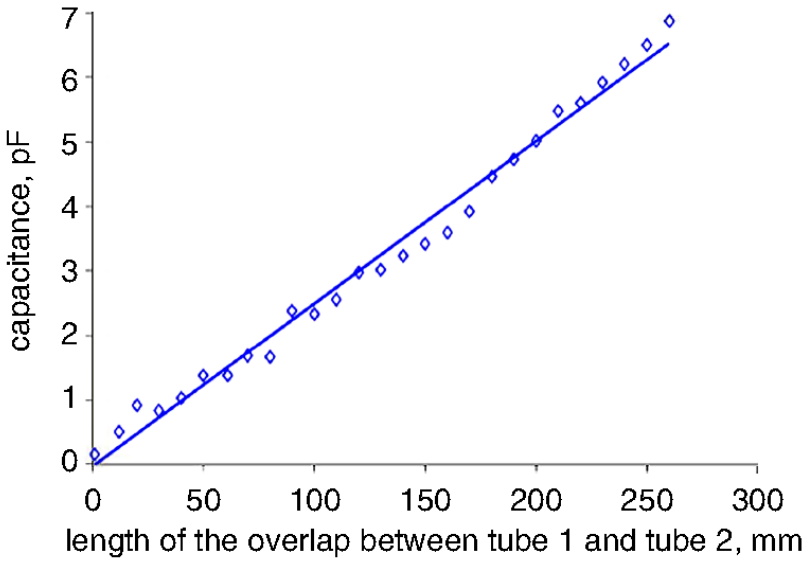

Figure. 6.5 Measured capacitance at 5 MHz for varying lengths of liquid metal in parallel-tube capacitor

6.3.3 Tunable Liquid-metal Folded-tube Capacitor

The liquid-metal folded-tube capacitor consists of a folded tube 1 that envelops tube 2 on both sides (Fig. 6.6a). The tubing and the electrical connections to the impedance analyzer are the same as described in Section 6.3.2. Tube 1 was filled entirely with liquid metal, and tube 2 was filled incrementally with liquid metal to change the capacitance. The design of this capacitor allows charges to build up on both sides of tube 2. Thus, the capacitance per unit length of the coil capacitor is 0.043 pF.mm^{-1}, 170% higher than the parallel-tube capacitor. The change in capacitance due to the variable length of liquid metal in tube 2 resulted in the tuning range of 27:1 (green data in Fig. 6.7).

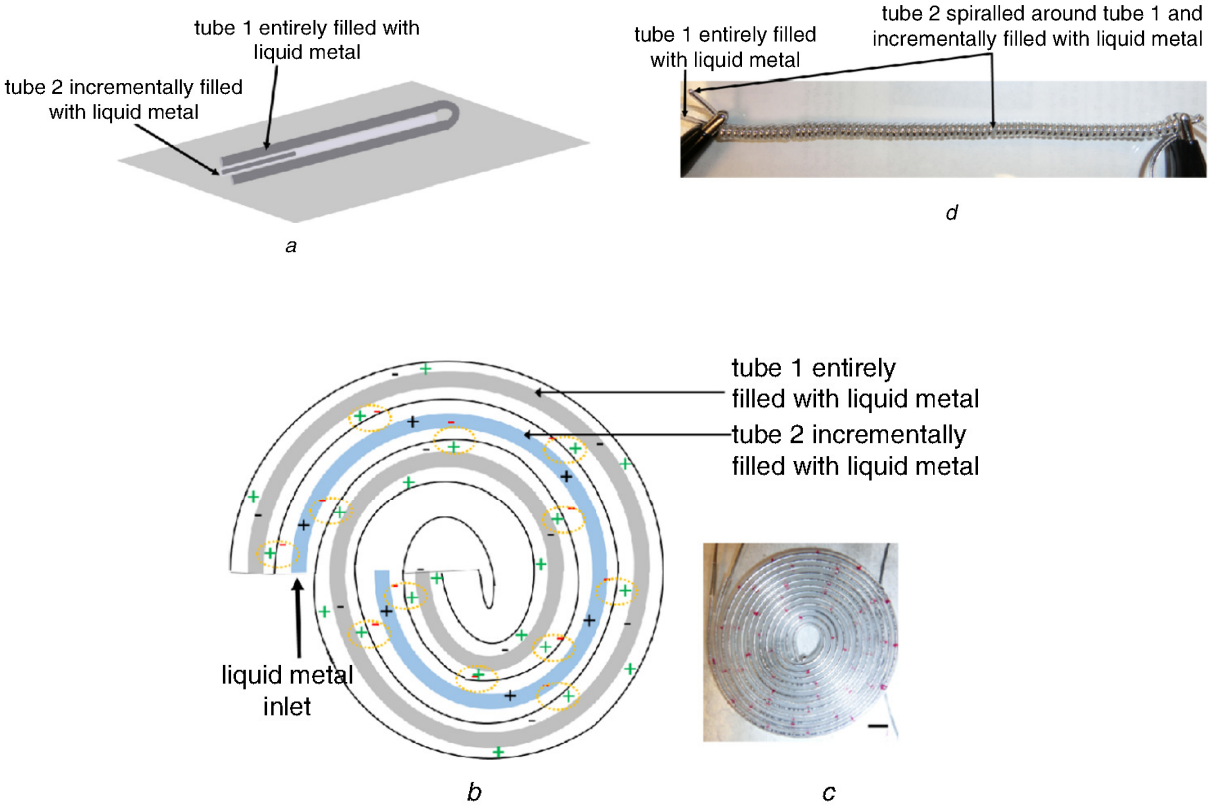

Figure. 6.6 Various shapes of liquid-metal capacitors. (a) Folded-tube liquid-metal capacitor. Tube 1 is filled with liquid metal and wrapped around tube 2. Liquid metal in tube 2 is actuated to vary capacitance. (b) Liquid-metal coil capacitor. Tube 1 is filled with liquid metal, and tube 2 is incrementally filled with liquid metal. Charge accumulation is marked with yellow circles. (c) Photograph of coil capacitor. Scale bar is 5 mm. (d) Photograph of liquid-metal

spiral capacitor. Tube 1 is filled with liquid metal. Tube 2 is spiralled around tube 1, and liquid metal is actuated in tube 2.

6.3.4 Tunable Liquid-metal Coil Capacitor

The third tunable capacitor was constructed by coiling a pair of 500 mm-long PVC tubes (Figs. 6.6b and c). Tube 1 was entirely filled with liquid metal, and liquid metal was pumped into tube 2. As liquid metal was added to tube 2, the capacitance linearly increased from 1.44 to 28.3 pF, a tuning ratio of 20:1 (blue data in Fig. 6.7). The capacitance per unit length of the coil capacitor was calculated 0.053 pF.mm^{-1}, 210% higher than the parallel-tube capacitor. In addition, the maximum capacitance was higher for the coil capacitor, which can be attributed to the charge accumulation on both sides of the pumped liquid metal in tube 2 (coloured in blue in Fig. 6.6b). The charge induced in the dielectric on both sides of the pumped liquid metal is highlighted with the yellow circles in Fig. 6.6b.

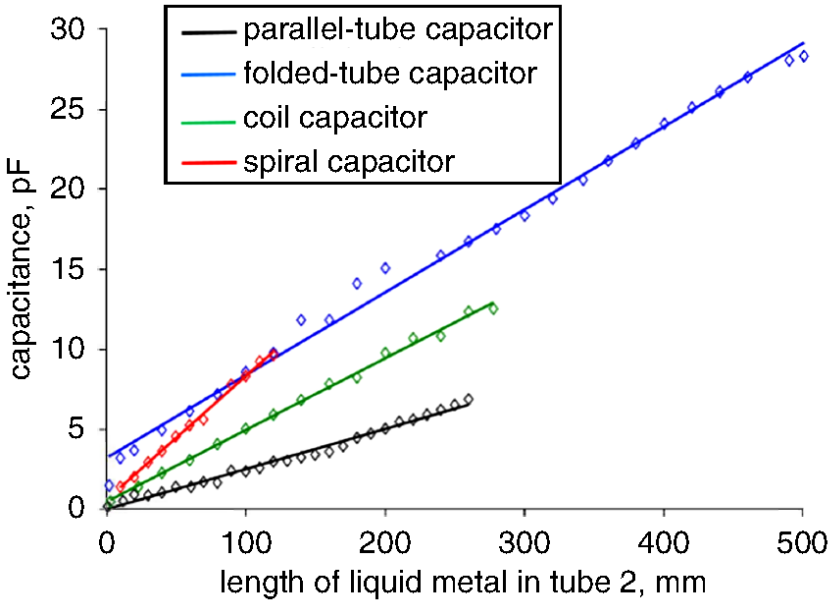

Figure. 6.7 Change in capacitance due to change in length of liquid metal in tube 2 for different liquid-metal capacitors. Change in capacitance per unit length of actuated liquid metal was 0.0252, 0.043, 0.053, and 0.07 pF.mm^{-1} for parallel-tube, folded-tube, coil, and spiral capacitors, respectively. Curves are linear fits to data points.

6.3.5 Tunable Liquid-metal Spiral Capacitor

The liquid-metal spiral capacitor consists of tube 2 spiraled around the entire length of tube 1 (Fig. 6.6d). Tube 1 was fully filled with liquid metal, and liquid metal was pumped into tube 2. The change in capacitance was the highest of the capacitors described here (red data in Fig. 6.7), corresponding to a capacitance per unit length of 0.07 $pF.mm^{-1}$.

6.4 Discussion and Conclusion

Among the four structures of liquid-metal tunable capacitors demonstrated (parallel-tube, folded-tube, coil, and spiral), the parallel-tube capacitor had the highest tuning ratio of 42:1. When considering the length of liquid metal required for tuning, the spiral capacitor performed best, as it had the highest change in capacitance per unit length of actuation. In addition, since the folded-tube and spiral capacitors had differing lengths for tube 1 and tube 2, another performance metric based on the amount of tubing used is defined here. The change in capacitance per unit of the average tubing length is given by

$$C_{max} - C_{min} = \frac{LT1+LT2}{2} \tag{6.1}$$

where C_{max} and C_{min} are the maximum and minimum capacitance of the tuning range, and LT1 and LT2 are the lengths of tube 1 and tube 2. This metric serves to compare the change in capacitance that can be achieved by the capacitor structures with respect to the footprint of the paralleltube capacitor. The coil-shaped microfluidic capacitor has the best performance according to this metric, measuring 214, 273, and 185% higher change in capacitance per unit length of the average tubing length as compared to parallel, spiral, and folded-tube microfluidic capacitors, respectively. The capacitance was linearly dependent on the length of liquid metal over the range of capacitance measured here, suggesting that the tuning range of the capacitors could be increased by extending the length of the liquid metal in every capacitor geometry demonstrated.

The liquid-metal-based microfluidic capacitors described in this chapter are easily constructed by hand, making them useful for the rapid prototyping of reconfigurable electronics. Their flexible nature (Fig. 6.8) allows usage on a curved surface without hampering the tunability. Use of this capacitor in MRI receive coil allows the antenna to be tuned in real time for correct resonance

frequency and its flexible nature will help build flexible MRI coil providing a good fit to the patient of all ages. Here, we leveraged various techniques of the microfluidics for construction liquid-metal based reconfigurable electronics for healthcare. In the next chapter, a bio-MEMS microfluidics device is used to position a micro-object for developing a non-invasive embryo grading system.

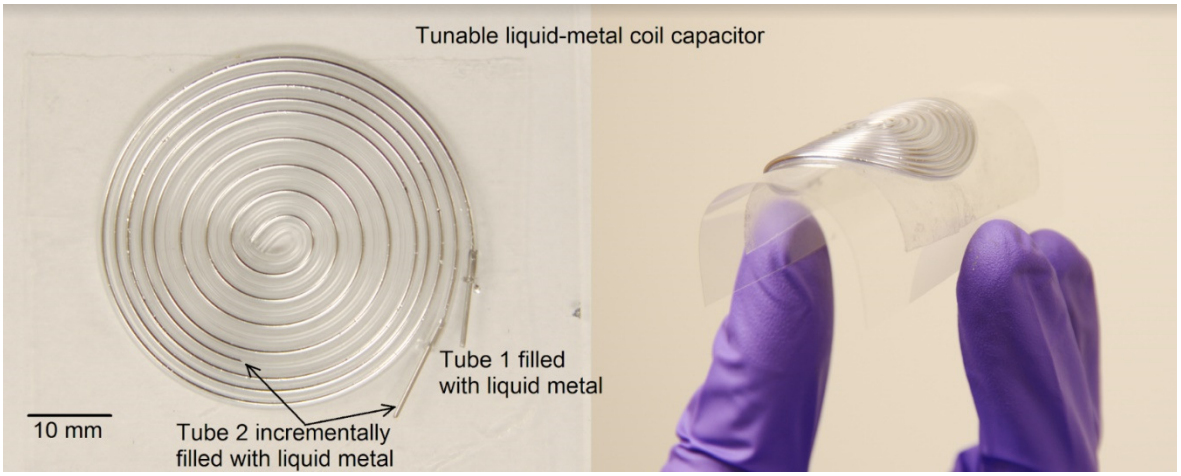

Figure. 6.8 Liquid-metal tunable, flexible, and lightweight capacitor

CHAPTER. 7 NON-INVASIVE EMBRYO GRADING SYSTEM

In vitro fertilization (IVF) is a common infertility treatment for couples who face difficulties getting pregnant naturally. According to the World Health Organization (WHO), any couple is failing to achieve a clinical pregnancy after 12 months or more of regular unprotected sexual intercourse is suffering from infertility disease [146]. About 10% of women (6.1 million) in the USA has infertility, and the number is higher in developing countries. Despite significant progress in IVF technology, the average pregnancy rate in IVF is about 30% with two or more replaced embryos. This statistic declines further with increasing maternal age, certain causes of infertility, and with various clinical parameters [69].

7.1 Challenges in Embryo Grading

In vitro fertilization (IVF) is a common infertility treatment. During the procedure, the woman is stimulated with injected medications to retrieve sufficient eggs for the IVF process. Then, a fertility doctor takes the eggs from the ovaries and fertilizes them *in vitro* with sperm in an IVF lab. After fertilization, the eggs develop into embryos. Three to five days later, the specialist re-implants the embryos back into the uterus. The reasons for IVF failure can be broadly divided into three groups: decreased endometrial receptivity, multifactorial effectors, and defective embryonic development [70]. Endometrial receptivity is temporary unique sequence of factors that make the endometrium receptive to the embryonic implantation. Multifactorial effectors include all markers of the reproductive process such as poor ovarian response. Decreased endometrial receptivity and multifactorial effectors like suboptimal ovarian stimulations are conditions of the patient, and need to be treated clinically. On the other hand, the effect of defects in embryonic development can be minimized by quality determination of the embryo prior to implantation (preimplantation). Although higher pregnancy success rates can be achieved by transferring two or more embryos to the patient, this can create multiple pregnancies [147], increasing risks to both mothers and infants. Thus, it is highly desired to be able to objectively select the healthiest available embryo for a single-implantation IVF pregnancy. However, the methods of healthy embryo selection in practice lack in quantitative analysis and automation. Currently, embryos are graded based on morphological observation at each stage of development [148]. This morphological grading is manually intensive, and is a qualitative method. However, recent developments in preimplantation genetic diagnosis (PGD) have led to human embryos being classified for their chromosomal

content [75]. PGD is a quantitative analysis of the embryo health which includes an invasive biopsy of the embryo and detailed screening of one cell for chromosome normalcy. The disadvantages of this approach are the need to remove one or two blastomeres from embryos for diagnosis, and added cost of screening to the patient [76]. Here, two approaches have been considered to address the need for automation in morphological grading, and for developing a non-invasive quantifiable embryo classification technique.

7.2 Real-Time Semi-Automatic Embryo Grading of Human Blastocyst

The precise assessment of embryo viability is extremely critical for successful IVF treatments. Several embryo-scoring systems are currently in practice in order to assess embryo viability. However, they depend mostly on a subjective visual analysis of embryo morphological features and thus are subject to observational variation. In this chapter, we propose a method for the image analysis of the human blastocysts, enabling classification with the aim of automating embryo grading.

7.2.1 Image Processing Methodology

Embryos at the blastocyst stage (5 to 8 days old) were imaged using an embryoscope, an incubator that maintains the necessary physiological conditions required by a living embryo. The embryoscope also has a camera that continuously captures images of the embryonic development. Time-lapse videos over a span of 10 hours during the early blastocyst stage were captured and used for image analysis. The images of the embryos were captured at 400x magnification. The time-lapse videos were exported in .avi format, then a MATLAB code that we developed was used to extract the frames from the time-lapse video. Each video has four frames in every hour, at 12- to 18-minute intervals. Figure 7.1 shows the steps of the image analysis operation. Another MATLAB function was developed to analyze the images using the MATLAB Image Batch Processor. The objective of the image analysis is to measure the area of the embryo over time. A total of 16 embryos were analyzed each with the same duration.

Figure 7.1a is a frame from the time-lapse video, showing a blastocyst in the embryoscope well. The objective of the image processing is to measure the area of the embryo in each frame. To achieve the objective, the embryo needs to be separated from the background. The embryoscope well position in all the image frames is fixed, so it is possible to accurately locate the well perimeter

based on its physical size. A circular binary mask was created where the pixels of the well were set to 1, and all other pixels were set to zero. Figure 7.1a includes the total ROI of the microscope camera. After passing through the binary mask, Figure 7.1b shows only the well; other parts of the image were cropped. In Figure 7.1c, the image is converted from RGB to grayscale by eliminating the hue and saturation information while retaining the luminance. Also, the image was sharpened by removing the blur using the MATLAB function "imfilter".

A binary image was created from Figure 7.1c by replacing all values above a globally determined threshold with 1s and setting all other values to 0s. Otsu's method was used to binarize the image, which chooses the threshold value to minimize the intraclass variance of the thresholded black and white pixels (Fig 7.1d) [136]. Next, a flood-fill operation was performed on the background pixels of the input binary image, Figure 7.1d. After the flood fill operation, the flood filled image was subtracted from the binarized image (Fig. 7.1d), resulting in the image shown in Figure 7.1e.

The approach for measuring the area was to measure the radius of the embryo by fitting it to a circle. In order to detect the circle-fit, the embryo edge was detected using "Sobel edge detector" comprised of two 2D filters, one to calculate the gradient in the column direction (top filter) and one to calculate the gradient in the row direction (bottom filter) (Fig. 7.1f). Another flood fill operation was carried out, and finally, the image was dilated (Fig. 7.1h). The dilation operation replaces each pixel with the local maximum of the neighborhood around the pixel, operating on a stream of binary intensity values. Figure 7.1h is the final processed image ready for circle detection. At this point, all the dilated image of a video was exported to a folder. A different MATLAB code was developed to detect circles from the dilated image (Fig. 7.1i) using the Hough transform, and the area of the circle was measured, which corresponds to the detected area of the embryo (Fig. 7.1j).

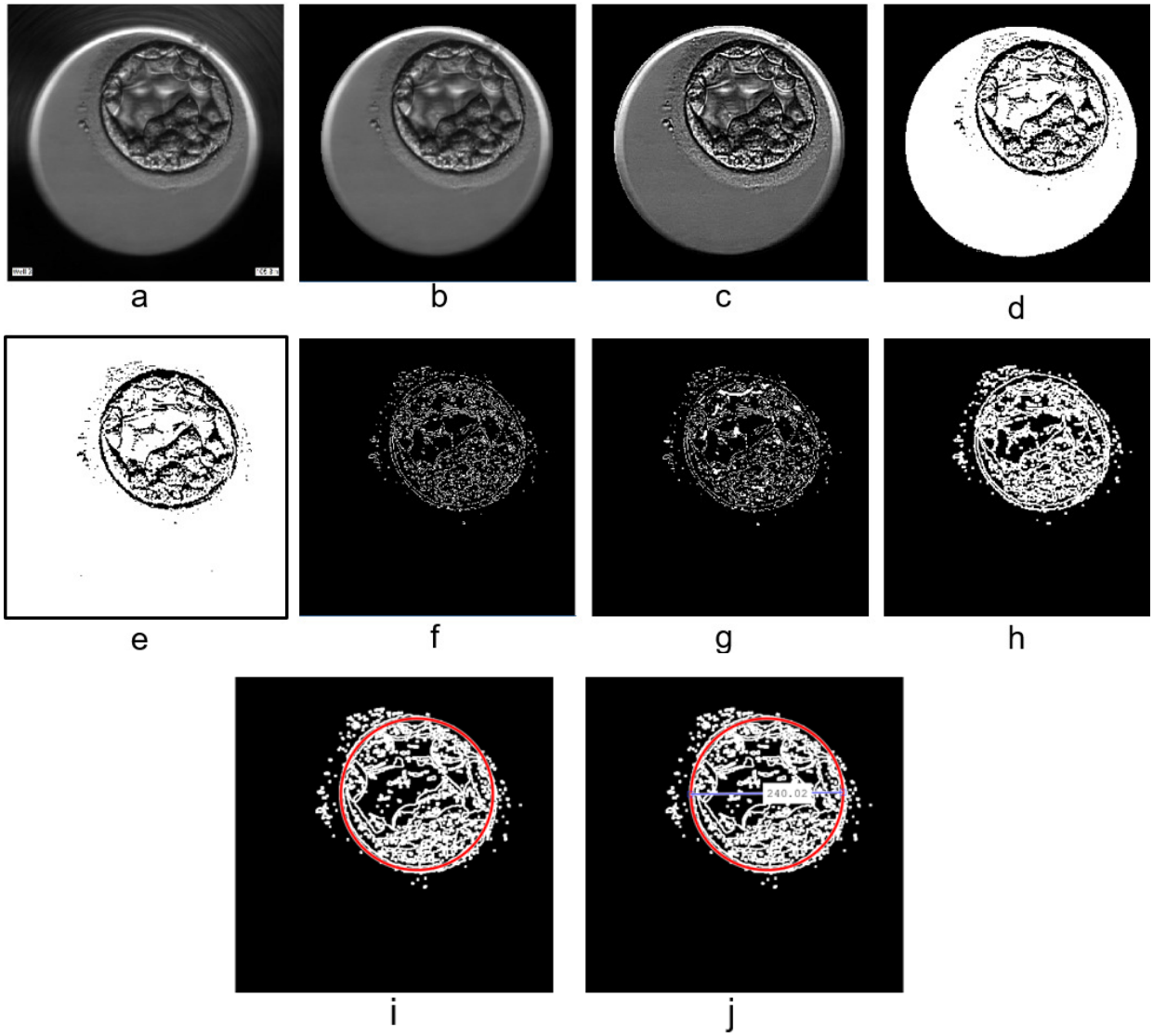

Figure. 7.1 Image analysis for calculating the area of an embryo. (a) Example of a blastocyst microscope image. (b) Circular ROI applied to crop the well from the image. (c) The image is converted from RGB to grayscale, and sharpened. (d) Binary image thresholding by Otsu's method. (e) The image was flood filled and then subtracted from the binarized image. (f) Edge detection using the "Sobel edge detector". (g) Flood-fill operation. (h) Image dilation replaces each pixel with the local maximum of the neighborhood around the pixel. (i) Circle detection using the Hough transform. (j) Diameter of the circle was measured.

7.2.2 Results Analysis

A total of 16 embryos were analyzed. Their area was measured using image processing algorithm explained above. Figure 7.2 and 7.3 shows the area of the embryos vs. hours over the time of observation (in terms of frame number of the video). The data points were fit with a linear regression. The slope of the linear fit is measured 279.98 μm^2. $frame^{-1}$, where average time gap between each frame is ~15 min. Figure 7.3 and 7.4 shows the linear fit of the area growth of all 16 embryos plotted against the number of image frame. Figure 7.3 and 7.4 shows the linear fit to the area growth of all 16 embryos plotted against the number of the image frame. The slope of each linear fit is mentioned in the inset.

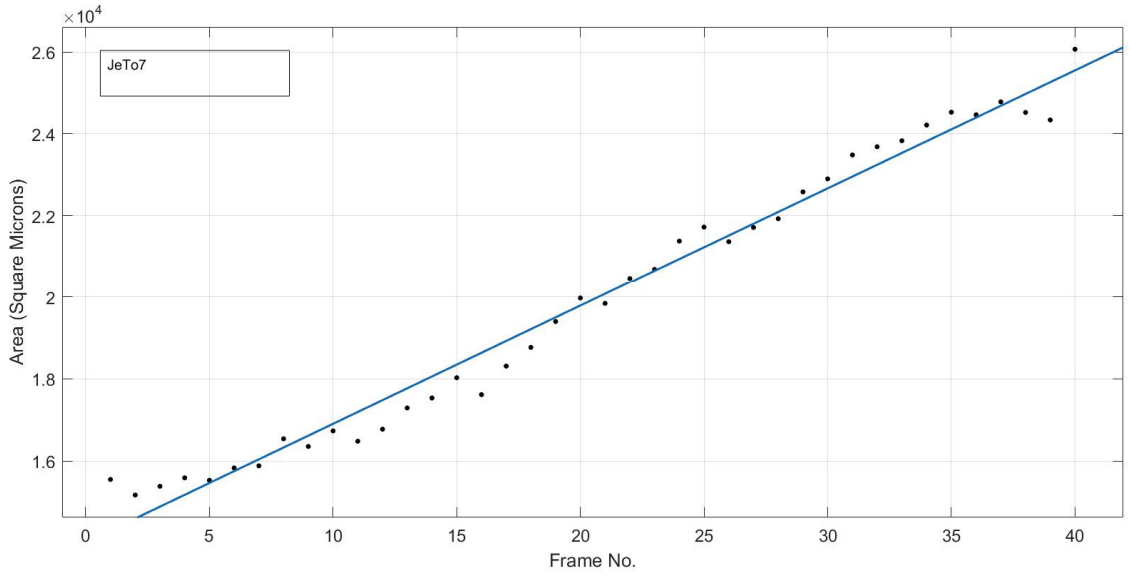

Figure. 7.2 Frame number Vs area of the blastocyst over 10 hours of observation before freezing for cryoprotection.

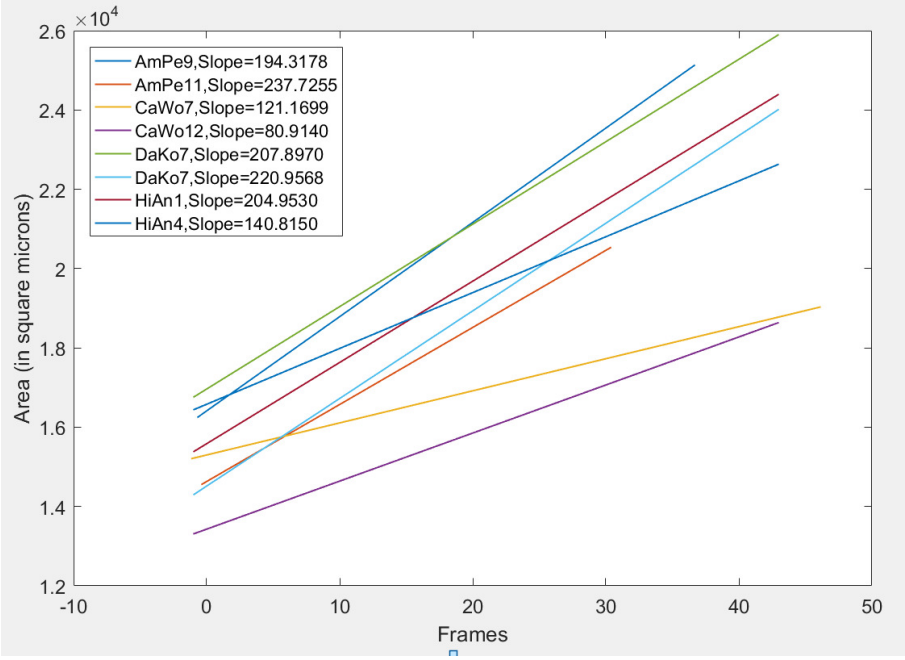

Figure. 7.3 Embryo growth over time for the embryo 1-8. The area is plotted against the frame number. Average time gap between each frame is ~ 15 min.

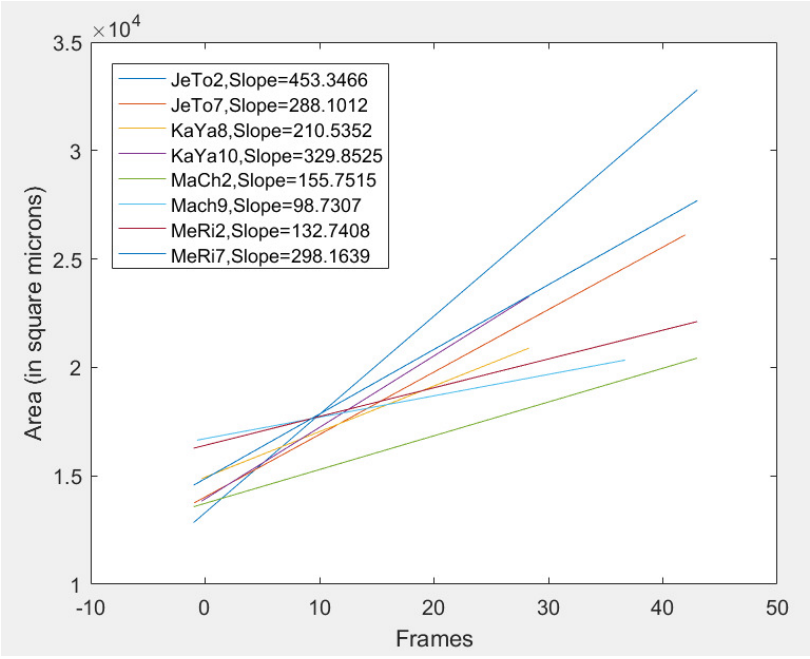

Figure. 7.4 Embryo growth over time for the embryo 9-16. The area is plotted against the frame number. Average time gap between each frame is ~ 15 min.

The embryo is randomly named for ease of discussion. The highest slope or highest average growth rate among the embryos was calculated as 453.37 μm^2/ frame (Fig. 7.4, JeTo2) and the lowest

growth rate was calculated as 80.91μm^2/frame (Fig. 7.3, CaWo12). The image processing algorithm developed here takes about 10 minutes to analyzed one video (10 hours at blastocyst stage) and calculate the growth rate over the duration of the video which includes visual verification of each frame for accuracy. The average number of blastocyst achieved from the 10-retrieved egg is about 3. Therefore, it will take about 30 minutes to analyze blastocyst image data from one patient using our code.

Figure 7.5 shows the comparison of the embryo growth rate measured through the digital image processing discussed above versus a manual process using the National Instruments (NI) Vision Assistant tools. The blue curve represents the data measured using digital image processing, and the green curve represents the manual measurement. The manual measurement is considered to be more accurate because each frame was visually observed and processed using the NI Vision Assistant tool. The embryo size measured using the image processing algorithm has average embryo area difference of 1345 μm^2 compared to manual measurement, an error of approximately 8%. The slope of the linear regression of the graphs is 177 μm^2 per frame (manually analyzed) and 122 μm^2 per frame (analyzed with image processing). Although these values are not equal, both of the growth trends in Figure 7.5 are similar, reducing the significance of this difference. The algorithm reported here fits the image of the embryo to a circle, then measures the circle area to calculate the area of the embryo (Fig. 7.1j). However, the embryo is slightly elliptical, which creates error compared to the manual measurement. As most embryos have a similar degree of ellipticity, the error does not have a significant effect on the final result, as the growth rate of all the embryos will have this relatively consistent error.

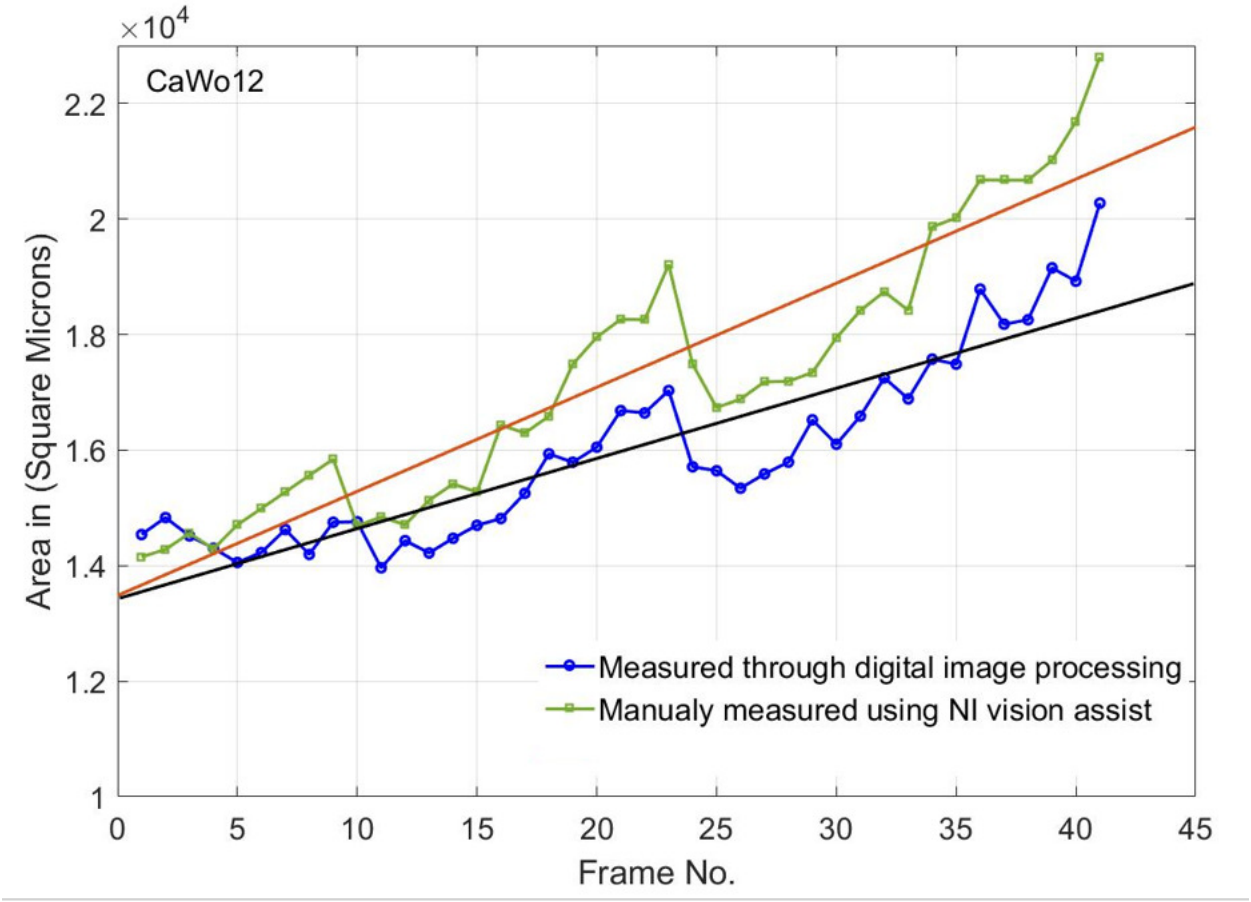

Figure. 7.5 Comparison of embryo growth over time measured through manual and digital image processing (a frame is captured approximately every 15 minutes).

7.3 Real-Time Embryo Grading Using Image Analysis

Preimplantation genetic diagnosis (PGD) is more detailed and quantitative process compare to morphological grading. This test is performed on cells taken out from the blastocyst using biopsy procedure. The cells are tested for chromosome normalcy. Chromosomes are found in the center of the cell nucleus. A human typically has 23 pairs of chromosomes, for a total of 46 individual chromosomes. An embryo receives 23 chromosomes from the sperm and 23 from the egg. Chromosomes are made up of genes, which contain the genetic information that instructs the body on how to function. While the number of chromosome in a cell is more or less than 46 the cell is regarded as genetically abnormal, a condition called aneuploidy. On the other hand, if the number of chromosomes is normal (23 pair), the cell is called euploid. The major disadvantages of this approach are that it is an invasive and costly procedure. Analyzing the growth rate of the previous

embryo which went through PGD, it was observed that euploid embryos have a higher growth rate than aneuploid embryos [149]. These suggest that the embryos with highest growth rate collected from one patient are more likely to be euploid compared to the other blastocyst collected from the same patient. The image-processing algorithm developed here can be used to calculate the growth rate in the real-time and the most viable embryos can be determined without the invasive PGD procedure. We are reporting the engineering solution to the problem, but the results need to be verified by the clinical data.

7.4 Non-Invasive Embryo Grading Solution

The image-analysis-based embryo grading demonstrated above is a semi-automatic qualitative measurement similar to other standard morphological gradings, except it includes quantitative analysis of the image. A more quantitative approach of embryo grading may improve the viability test further. Electrical impedance spectroscopy can provide quantitative information of single *Artemia* cysts at various phases of development. A distinct pattern of impedance changes was observed at three different stages of cyst development. The measured impedance changes corresponded to physiological changes as the cyst developed. The change in impedance during the first stage of development provided sufficient quantitative data to predict if the cyst would hatch. This work shows the potential of impedance spectroscopy for developing a non-invasive test to quantitatively determine the health of the embryos.

Conventional monitoring of embryos for IVF is qualitative, including observing physiological and morphological changes in different phases of development [148, 149]. There exists a need for a low-cost, time-efficient, non-invasive system to quantify the health of embryos at the early stages of development [148]. Impedance spectroscopy in a microfluidic environment has the potential to satisfy these requirements, as it enables monitoring and characterization of bioprocesses by measuring the electrical properties of single cells or embryos [152]. Collected data can be analyzed for correlation with physiological changes in the embryo. Here, the impedance of single *Artemia* (brine shrimp) cysts are measured in a microfluidic channel and in an open reservoir. The measured impedance corresponds to distinct stages in the cyst development, and can be used to predict if the cyst hatches. As a cyst is like an embryo in its prenatal development stage, these measurements show the potential of this technique for quantifying the health of embryos during development.

7.4.1 Model and Methodology

A simplified electrical equivalent circuit of an *Artemia* cyst between two electrodes is shown in Fig. 7.6. This equivalent circuit includes a double layer capacitance on each electrode, impedances and capacitances for the cell and interior of the cyst, and the capacitance and impedance of the liquid media. This model of the experimental environment provides insight into the impedance as a function of frequency for the cyst and the surrounding liquid media.

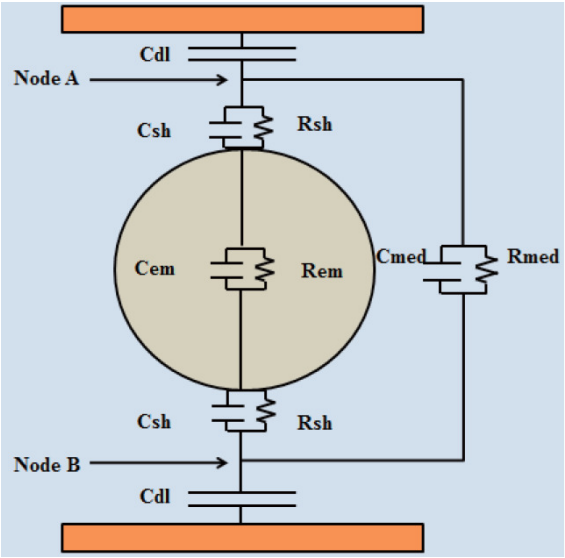

Figure. 7.6 The equivalent circuit model for the measurement of cyst impedance using the fabricated microfluidic device. Since the cyst has a hard shell, it can be modeled using a single-shell structure. The orange boxes represent the electrodes.

The circuit elements shown in Fig. 1 are characterized by Equations (7.1) to (7.6) below [8, 9]. In these equations, C_{dl}, C_{sh} and R_{sh}, C_{em} and R_{em}, and C_{med} and R_{med} are the capacitances and resistances of the electrical double-layer, shell, embryo, and media, respectively.

$$Z_t = 2 * Z_{dl} + [(Z_{sh} + Z_{em}) || Z_{med}]$$
$$= 2 * Z_{dl} + \frac{2*Z_{sh}*Z_{sol}+Z_{em}*Z_{med}}{2*Z_{sh}+Z_{em}+Z_{med}} \quad (7.1)$$

$$Z_{sh} = Z_{Rsh} \| Z_{Csh} = \frac{R_{sh}}{j*\omega*R_{sh}*C_{sh}+1} \quad (7.2)$$

$$Z_{em} = Z_{Rem} \| Z_{Cem} = \frac{R_{em}}{j*\omega*R_{em}*C_{em}+1} \quad (7.3)$$

$$Z_{med} = Z_{Rmed} \| Z_{Cmed} = \frac{R_{med}}{j*\omega*R_{med}*C_{med}+1} \quad (7.4)$$

$$Z_{dl} = \frac{1}{j*\omega*C_{dl}+1} \quad (7.5)$$

$$C_{dl} = \frac{\varepsilon*A}{d} = \frac{\varepsilon*A}{L_d} \quad (7.6)$$

The double layer capacitance, C_{dl}, at the electrode contacts depends on the Debye length, as shown in Equation (7.6). The Debye length can be solved for using

$$L_d = \sqrt{\frac{\varepsilon*k_B*T}{2*z^2*q_e^2*C_0}} \quad (7.7)$$

where ε is the permittivity, k_B is Boltzmann's constant, T is the absolute temperature, z is the count of valence ions in the solution, q_e is the elementary charge value, and C_0 is the molar concentration of ions [8, 9]. The *Artemia* cysts were smaller than the electrodes used in the study, making the impedance contribution from the media an important factor to consider. It is important to use salinated natural spring water to properly hydrate the quiescent cysts and prepare them for eventual hatching. The 100-µm-radius cyst is placed between two 250 µm-radii conductors, and can be replaced by a circuit equivalent Z_{cyst} between nodes A and B. Z_{med} is then the modeled impedance contribution from the surrounding media, which is in this case salinated natural spring water. Z_{med} is in parallel to Z_{cyst}, and has a significant contribution to the overall impedence changes of the circuit. Another contribution to the overall impedance stems from the impedance from electric double layer, Z_{dl}. This term cannot be negated since the media used had a significant ionic concentration of salts. Therefore, the circuit modeled in Fig. 7.6 provides an understanding of each circuit element and their underlying contribution to the overall impedance as measrured using the electrodes. Two separate measurements were then taken in the experiments, one with the cyst between the electrodes and one with only the aqueous media between the electrodes. The differential impedance was then calculated by subtracting the media-only measurement from the cyst measurement. Fig. 7.7 shows the measured change of impedance as the frequency of a 1 Vp-p ac signal was swept from from 1 kHz to 1 MHz. The impedance changes as a function of

frequency as different impedances dominate (from the cyst or the media). A frequency of 1 kHz was selected for impedance measurements over the cyst development period, as it has a high magnitude, and the impedance values near that frequency vary linearly over a smaller range than at higher frequencies.

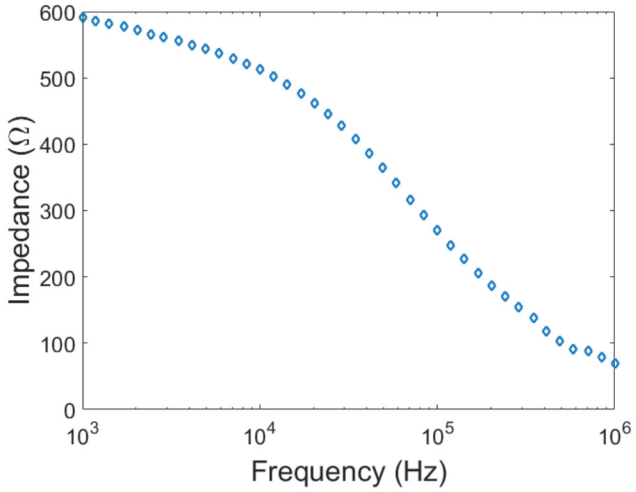

Figure. 7.7 Experimentally measured data from a single cyst measured during the pre-emergence development phase. A frequency of 1 kHz was selected for the measurement of impedance over the embryo development period, as it has a high impedance magnitude, and the impedance has a relatively small linear variance about this frequency.

7.4.2 Design, Fabrication, and Experimental Setup

Artemia create dormant embryos, called "cysts." Thus, *Artemi*a cysts were chosen for this initial study due to their hardiness, cost, and availability, even though a cyst has a hard shell, unlike a mammalian embryo. The impedance of the cysts was measured using two different configurations. In the first configuration, the cysts were placed between two electrodes in a microfluidic channel (Fig. 7.8). The medium used was spring water mixed with sea salt to a salinity of approximately 70 gm·l^{-1}. A rapidly prototyped microfluidic device was fabricated for the precise positioning of an *Artemia* cyst between two electrodes for the measurement of the cyst impedance during its growth (Fig. 7.8). The size of a hydrated *Artemia* cyst ranges from 200 to 230 µm [153], and influenced the dimensions of the main fluidic channel, which is approximately 500 µm wide and 500 µm high. Copper electrodes placed in channels orthogonal to the main channel were connected to a Hioki IM 3570 impedance analyzer. A 500 µm thick PDMS film was used as the ceiling of the channel. One end of the main channel was left open for inserting the cysts, and the other end was connected to a syringe pump.

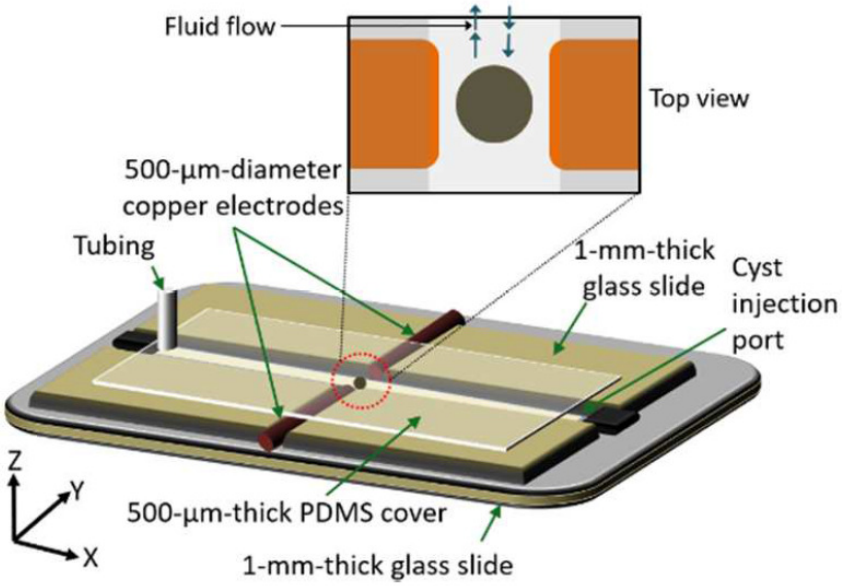

Figure. 7.8 The microfluidic device for measuring impedance changes in *Artemia* cysts using the first configuration. The inset shows the top view of the device with a cyst positioned between the electrodes. The green arrows show the fluid flow used for positioning the cyst.

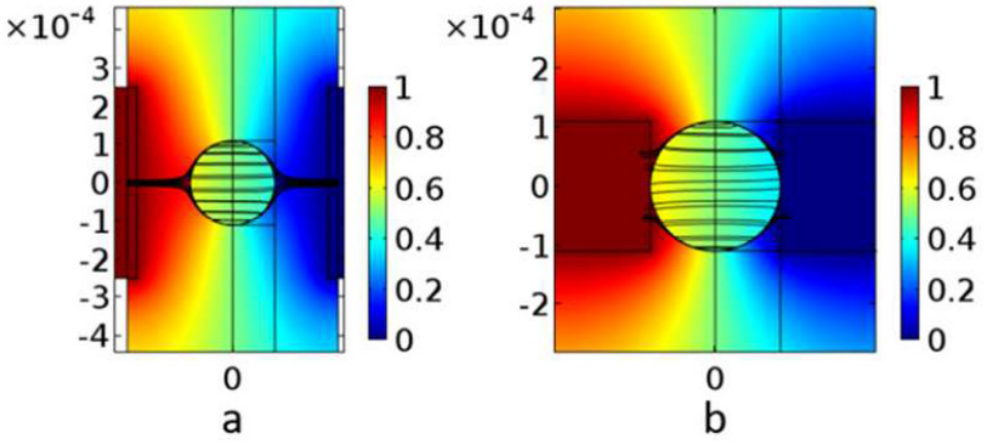

Figure. 7.9 COMSOL simulation of two different device configurations used for this experiment. (a) The device configuration where the cyst is suspended in a medium, centered in the channel, and 140 µm away from each of the conductor's face. The simulation measures total x component of current density passing from anode to cathode is 7.2271 $A.m^{-1}$, 0.10743 $A.m^{-1}$ through the center of the cyst, and 1.6488 $A.m^{-1}$ at the cyst shell near the anode. (b) The cyst is sandwiched between the conductor's face measuring higher current passing through the cyst compare to Fig. 7.9a.

Ideally, the measured impedance over time should correspond to changes to the cyst as it grows. Thus, more current passing through the cyst should result in a higher sensitivity. A COMSOL Multiphysics simulation shows that the first configuration (Fig. 7.9) allows 1.5% of the total current to pass through the center of the cyst and 22.8% of the total current to pass through the cyst shell (Fig. 7.9a). This is expected, since the electrode surface is larger than the cyst, so the liquid impedance is significant. However, if the surface of the measurement electrode is the same size as the cysts and placed in contact with the cyst surface (as in the second configuration Fig. 7.9b), 2.2% of the total current passes through the center of the cyst and 32% of the current passes through the cyst shell (Fig. 7.9b). This suggests that the second configuration will provide higher sensitivity.

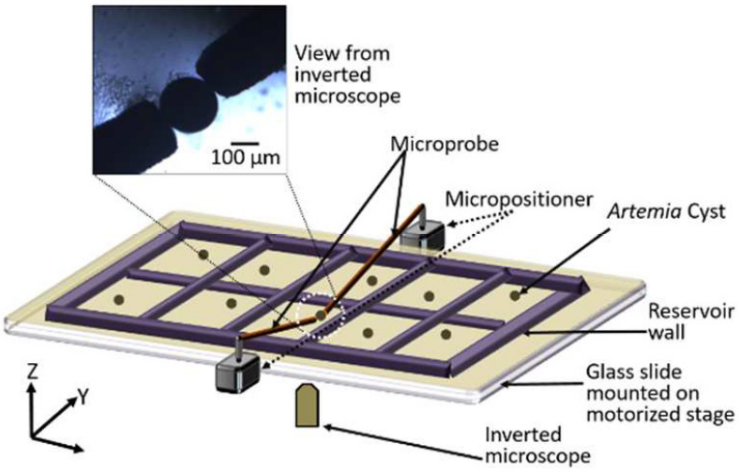

Figure. 7.10 Multiwell reservoir for the measurement of cyst impedance allows the measurement setting of Fig. 7.8b.

A platform to enable the measurement setting of Fig. 7.9b was created (Fig. 7.10). Ten reservoirs, each 10 mm long, 8 mm wide, and 500 µm deep, were formed on a 75-mm by 25-mm glass slide. Two micropositioners were used to position 200-µm-diameter electrodes that were connected to the impedance analyzer.

The *Artemia* cysts were suspended in salt water at a pH of approximately 7.6 and a temperature of 26 °C. The impedance and phase were measured using the first configuration (Fig. 7.8) with a 1-Vpp ac signal sweeping from 1 kHz to 1 MHz at 400 discrete frequencies. The sweep range and interval were adjusted to 100 Hz to 5 MHz at 301 discrete frequencies for the second configuration (Fig. 7.10). The impedance was measured at varying time intervals over a period of approximately

20 to 40 hours, or until hatching of the cyst was visually observed. The results are presented for the impedance measured at 1 kHz, because the impedance values at and near 1 kHz varied less than the measurements at the higher frequencies. The impedance data reported here were calculated by taking the difference of an impedance measurement with the cyst between the electrodes and an impedance measurement of only the salinized water.

7.4.3 Results & Discussions

In the first experiment, the impedance magnitude and phase of the cyst was monitored until it hatched [3]. Several *Artemia* cysts were monitored using multiple devices in the first configuration (Fig. 7.8). A dry cyst is an undifferentiated gastrula containing less than 10 % water. The cyst starts its metabolic activities when its water levels are higher than 10% and when it is exposed to oxygen [154]. Metabolic activities increase significantly as the cyst hydration level increases to 140% of the initial dry state, which usually occurs within an hour or two. Once the cyst reaches the 140% hydration level, its developmental stage can be divided into three phases. They are: 1) a preparatory phase that is about 20% of the total hatching time; 2) a pre-emergence development (reversible phase) that lasts about 50% of the total hatching time; 3) a non-reversible phase that lasts for approximately 30% of the total hatching time [153]. Figure 7.11 shows the change of impedance across the cyst measured using measurement setting of Figure 7.8. Figure 7.11a, 7.11b, and 7.11c correspond to different cysts, but similar trends of impedance changes over time suggest this method is suitable for the monitoring of cyst development. A low impedance was observed during the preparatory phase. The large increase in impedance in the pre-emergence phase corresponds to another change in biological activity. Finally, a substantial decrease in impedance is observed in the non-reversible phase. Thus, the hydration of the cyst and the three stages of development correspond to changes in the cyst impedance. Specifically, these events are marked through hydration of the cyst, ending the quiescence period and leading up to full hydration of the cyst, and finally hatching. The non-reversible phase indicates the end of dormancy, and if the cyst does not hatch then it will die. Three separate cysts had peak impedances in the preparatory, pre-emergence development, and non-reversible phases of 75 Ω, 300 Ω, and 100 Ω for the first cyst, 25 Ω, 225 Ω, and 50 Ω for the second cyst, and 250 Ω, 600 Ω, and 100 Ω for the third cyst.

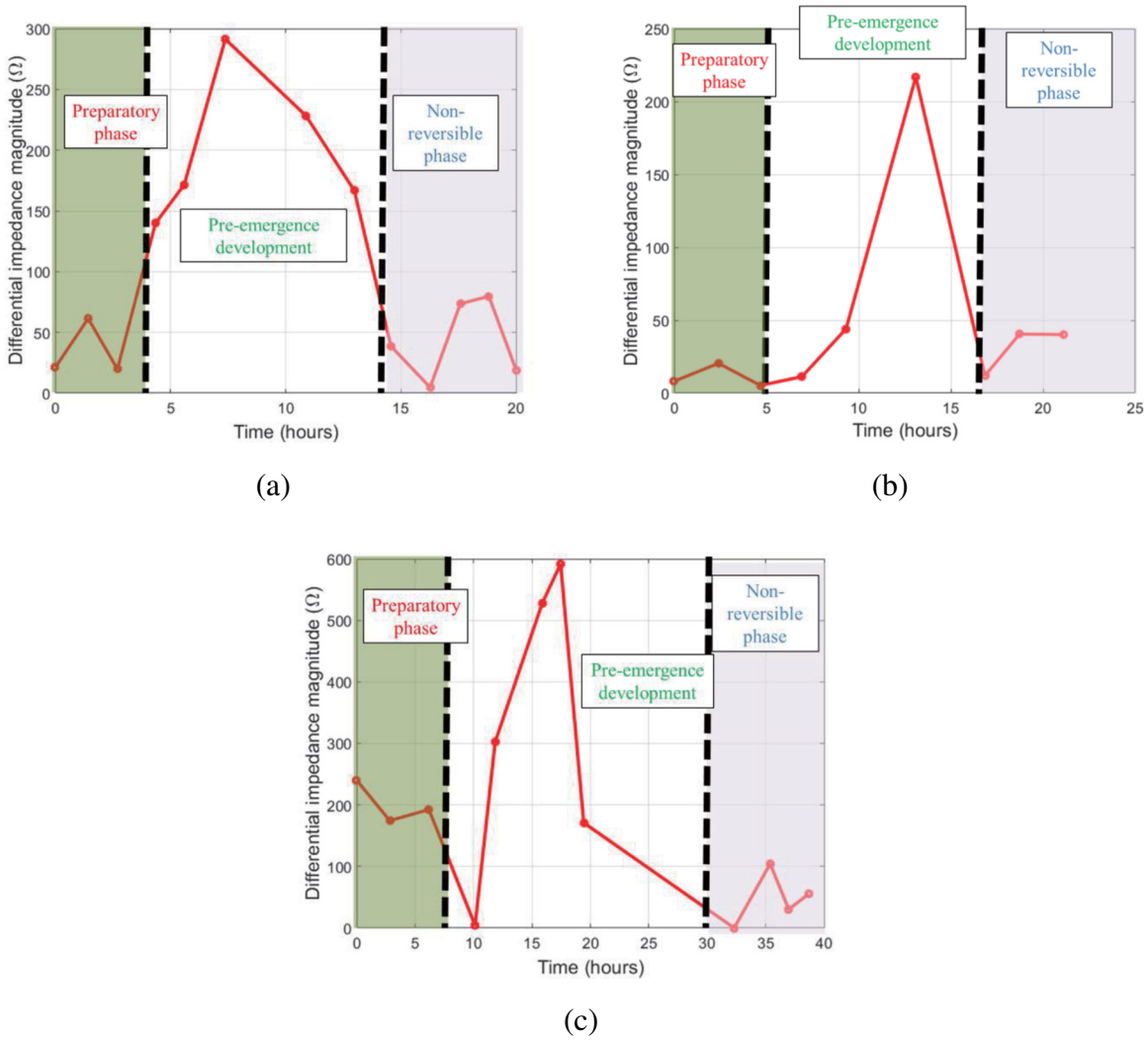

Figure. 7.11 Differential impedance magnitude from 0 hours until the approximate hatching time (0 hours indicates when the cyst was first placed in media), for three separate cysts. The three major stages of development are outlined: the preparatory phase, the pre-emergence development phase, and the non-reversible phase.

A major concern was to also not severely impact the health of the *Artemia* cyst by interrogating it with electrical impulses. The effects of electric fields were previously investigated for freely swimming *Artemia*, and it was found that they were able to withstand 100 50-ns pulses of a 7 $kV.cm^{-1}$ field, 10 50-ns pulses of a 12 $kV.cm^{-1}$ field, and 2 50-ns pulses of a 20 $kV.cm^{-1}$ field before being immobilized [155]. The interrogation voltage in the experiments performed here is 1 V across a 500-µm gap, corresponding to an electric field of 20 $V.cm^{-1}$, although the cysts are exposed to this electric field for a longer period of time than the higher fields tested in [155].

Therefore, this interrogation method should have a negligible impact on the cysts, although more detailed viability testing is necessary.

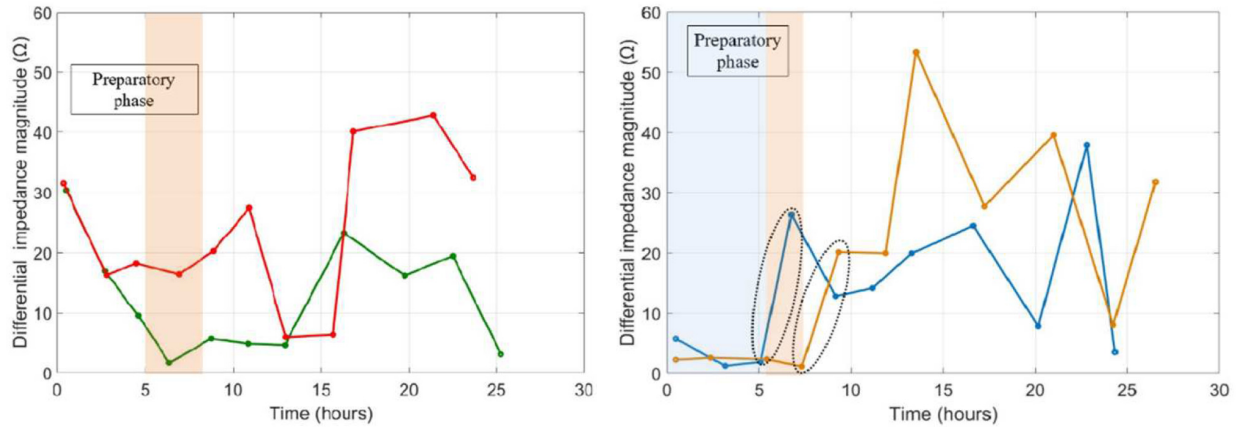

(a) (b)

Figure. 7.12 Differential impedance magnitude of four different *Artemia* cysts (a) Change of impedance magnitude over time for two cysts that did not hatch. The shaded area indicates the range of time where the preparatory phase ends (~20% of the total hatching time). The hatching time observed during the experiment varied from 24 to 40 hours for different cysts. (b) Change of impedance magnitude over time for two cysts that hatched. The shaded areas indicate the approximate duration of the preparatory phase for the cysts; blue shading corresponds to the blue curve and orange shading corresponds to the orange curve. The dotted semicircle highlights the steep increase of impedance at the end of the preparatory phase or during the first hours of pre-emergence development phase.

Fig. 7.12 shows the change of cyst impedance measured using the second configuration (Fig. 7.10). The impedance of several cysts was measured from zero to up to 27 hours. Close to their hatching time, the cysts were transferred to bulk media for hatching. Fig. 7.12a shows the data for two cysts which did not hatch and Fig. 7.12b shows the data of two cysts which did hatch. The hatching time of the cysts represented by blue and orange curves was ~28 hours and ~37 hours, respectively (Fig. 7.12b). We observed the sharp rise of impedance at the end of the preparatory phase in Fig. 7.12b (hatched). On the other hand, Fig. 7.12a shows the increase of impedance at a much slower rate at the same stage (did not hatch). The slopes of the curve at the end of the preparatory phase for the cysts that hatched were 15 $\Omega.hr^{-1}$ (Fig. 7.11b, blue curve), and 13 $\Omega.hr^{-1}$ (Fig. 7.12b, orange curve). The cysts which did not hatch have a slope in the range of 1-2 $\Omega.hr^{-1}$ at the end of the preparatory phase (Fig. 7.12b). Thus, the slope. of the impedance magnitude at the end of the preparatory phase or first hours of the pre-emergence development phase can be used to predict cyst hatching at an

early stage of development. The growth of the nauplii (larvae of brine shrimp) inside the cyst shell resembles the biological process in mammalian embryos, so this method has potential for the quantifiable measurement of bovine embryos. Moreover, determining the *in vitro* health information of the embryos requires conclusive detection at an early stage of its growth. In this regard, these experiments also show impedance spectroscopy is a potential method for this application.

7.5 Conclusion

In this chapter, two approaches of embryo viability detection presented. In the first approach, human blastocyst microscope images are analyzed to measure the growth rate over the period of observation. This semi-automatic embryo grading technique will aid the current morphological grading system and provide real-time data for selecting the most viable embryo. In the second approach, the impedance across the embryos was measured over time as they grow. The change of impedance across the embryo correlates the cellular activities happening inside the embryo. We performed the experiment on *Artemia* cysts and observed that a distinct impedance pattern was found for the specific phases of development, which implies that this method can work for other embryos providing critical quantitative health information of the embryo. This result shows promise for a non-invasive embryo grading method.

CHAPTER. 8 CONCLUSION AND FUTURE WORK

Microfluidics enables disease detection at earlier stages compared to conventional bulk specimen tests, and has many other uses, from health monitoring to the treatment of various diseases. Bio-MEMS provides engineering solutions for the next generation of healthcare devices. In this dissertation, the technologies in these two branches of engineering were leveraged to create potential solutions for specific healthcare problems.

The ability to manipulate biological entities in a liquid medium is beneficial for various biomedical applications. The challenges in manipulating bio-micro-objects include increasing precision, reducing invasiveness, and increasing throughput. This dissertation presented a cell-friendly, high-resolution, high-throughput bio-micromanipulation system based on opto-thermocapillary flow-addressed bubble (OFB) microrobots. Independent actuation of fifty OFB microrobots in parallel was demonstrated. The independent addressing of many microrobots enables higher-throughput microassembly of micro-objects, and cooperative manipulation using multiple microrobots. The independent maneuverability of the microrobots was demonstrated by the transportation of microstructures using a pair or team of microrobots and the cooperative manipulation of multiple micro-objects. Also, a hybrid closed-loop vision-assisted control system was demonstrated that is capable of actuating multiple microrobots simultaneously and positioning them at precise locations relative to micro-objects under manipulation. The closed-loop control resulted in 50% less position error compared to the open loop actuation. In addition, the closed loop control enables robotic actuation such as path planning, and collision avoidance. Actuation of many microrobots independently in parallel, and demonstration of co-operative micromanipulation with robust control system have shown promise for tissue engineering applications such as *in vitro* tissue constructs. However, this application can benefit from 3D manipulation of bio-objects using untethered microrobots. The future direction for this research is going to be 3D actuation of microrobots using hybrid forces such as optothermal and magnetic force. An automated real-time closed-loop control system can be developed for controlling the microrobots in 3D.

Microfluidics techniques were leveraged to control and precisely position liquid metal as a tuning element for passive electronics. The tunable liquid-metal capacitor reported in this dissertation can effectively be used for tunable and flexible MRI receive coils. Four different structures are demonstrated: parallel-tube, folded-tube, coil, and spiral capacitors. The highest measured tuning ratio is 42:1, and the change in capacitance per unit length of the pumped liquid metal for above structures are 0.0252, 0.043, 0.053, and 0.07 $pF.mm^{-1}$. The tuning range of the capacitor covers the Larmor frequency for a 3-T MRI scanner (127 MHz). The tunable capacitor developed in this work can be used in tunable circuits that require high tuning ranges, such as filters, resonators, oscillators, and antennas. The rapid prototyping demonstrated here also makes this work suitable in a research lab setting. Moreover, the flexible nature of the capacitor allows its use in wearable medical electronics. The future direction for this research is fabricating the antenna array and testing its performance in MRI scanner.

Accurate assessment of embryo viability is essential for successful IVF treatment. This dissertation has reported an image-processing-based semi-automatic real-time grading method for human blastocysts during IVF procedures. The image processing algorithm calculates the growth rate of the embryo at blastocyst stage in the real-time and plots the area over time. The slope of the graph reports the embryo with highest growth rate. The control group for the grading system is the growth data of the blastocysts that went through preimplantation genetic diagnostics (PGD) procedure and proved to be euploid. The grading method proposed will aid the current morphological grading practices, and have the potential to supersede current practices after being verified by the clinical trials. The future direction of this research will be to implement the embryo grading technique in IVF clinics and verify its outcome by the successful or unsuccessful pregnancies resulted from the implantation.

Image-assisted embryo grading is a qualitative measurement similar to other standard morphological gradings. This dissertation hypothesizes that the embryo health information can be quantitatively measured by measuring the electrical impedance changes across the embryo during its biological development at an early stage of development. This method is non-invasive and provides quantitative data about the health of the embryo. We reported data recorded using *Artemia* cysts that supports this hypothesis. Currently, research is ongoing using embryos without

a hard shell, such as sea urchin embryos. Future studies will be carried out using mouse embryos and ultimately human embryos.

BIBLIOGRAPHY

[1] M. A. Rahman, J. Cheng, Z. Wang, and A. T. Ohta, "Cooperative micromanipulation using the independent actuation of fifty microrobots in parallel," *Sci. Rep.*, vol. 7, no. 1, pp. 1–11, 2017.

[2] M. A. Rahman, W. A. Shiroma, and A. T. Ohta, "Liquid-metal capacitors with a 42:1 tuning ratio," *Electron. Lett.*, vol. 53, no. 11, 2017.

[3] K. Matthews, M. A. Rahman, A. T. Ohta, and M. Garcia, "Rapid measurement of impedance changes associated with developmental phases in Artemia cysts," in *12th IEEE International Conference on Nano/Micro Engineered and Molecular Systems (NEMS)*, Los Angeles, CA, 2017.

[4] S. Yim, S. Miyashita, D. Rus, and S. Kim, "Teleoperated micromanipulation system manufactured by cut-and-fold techniques," *IEEE Trans. Robot.*, vol. 33, no. 2, pp. 456–467, 2017.

[5] L. Feng, S. Zhang, Y. Jiang, D. Zhang, and F. Arai, "Microrobot with passive diamagnetic levitation for microparticle manipulations," *J. Appl. Phys.*, vol. 122, no. 24, 2017.

[6] H. Li, G. Go, S. Y. Ko, J. O. Park, and S. Park, "Magnetic actuated pH-responsive hydrogel-based soft micro-robot for targeted drug delivery," *Smart Mater. Struct.*, vol. 25, no. 2, pp. 027001, 2016.

[7] C. Y. Chen, C. F. Chen, Y. Yi, L. J. Chen, L. F. Wu, and T. Song, "Construction of a microrobot system using magnetotactic bacteria for the separation of Staphylococcus aureus," *Biomed. Microdevices*, vol. 16, no. 5, pp. 761–770, 2014.

[8] F. Ullrich *et al.*, "Mobility experiments with microrobots for minimally invasive intraocular surgery," *Investig. Ophthalmol. Vis. Sci.*, vol. 54, no. 4, pp. 2853–2863, 2013.

[9] M. Sitti *et al.*, "Biomedical applications of untethered mobile milli/microrobots," *Proceedings of the IEEE.* , vol. 103, no. 2, pp.205-224, 2015.

[10] L. Feng, X. Wu, Y. Jiang, D. Zhang, and F. Arai, “Manipulating microrobots using balanced magnetic and buoyancy forces,” *Micromachines*, vol. 9, no. 2, 2018.

[11] F. Niu, J. Li, W. Ma, J. Yang, and D. Sun, “Development of an enhanced electromagnetic actuation system with enlarged workspace,” *IEEE/ASME Trans. Mechatronics*, vol. 22, no. 5, pp. 2265–2276, 2017.

[12] E. Diller, J. Giltinan, and M. Sitti, “Independent control of multiple magnetic microrobots in three dimensions,” *Int. J. Rob. Res.*, vol. 32, no. 5, pp. 614–631, 2013.

[13] M. Latulippe, O. Felfoul, P. E. Dupont, and S. Martel, “Enabling automated magnetic resonance imaging-based targeting assessment during dipole field navigation,” *Appl. Phys. Lett.*, vol. 108, no. 6, 2016.

[14] D. Folio and A. Ferreira, “Two-dimensional robust magnetic resonance navigation of a ferromagnetic microrobot using Pareto optimality,” *IEEE Trans. Robot.*, vol. 33, no. 3, pp. 583-593, 2017.

[15] N. A. Torres and D. O. Popa, “Cooperative control of multiple untethered magnetic microrobots using a single magnetic field source,” *IEEE Int. Conf. Autom. Sci. Eng.*, vol. 2015–Octob, no. October, pp. 1608–1613, 2015.

[16] D. S. Contreras and K. S. J. Pister, “Dynamics of electrostatic inchworm motors for silicon microrobots,” in *IIEEE nternational Conference on Manipulation, Automation and Robotics at Small Scales (MARSS)*, pp. 1–6, 2017.

[17] B. R. Donald, C. G. Levey, and I. Paprotny, “Planar microassembly by parallel actuation of MEMS microrobots,” *J. Microelectromechanical Syst.*, vol. 17, no. 4, pp. 789–808, 2008.

[18] B. R. Donald, C. G. Levey, I. Paprotny, and D. Rus, “Simultaneous control of multiple MEMS microrobots,” *Springer Tracts Adv. Robot.*, vol. 57, no. i, pp. 69–84, 2010.

[19] D. H. Kim, U. K. Cheang, L. Khidai, D. Byun, and M. J. Kim, “Artificial magnetotactic motion control of Tetrahymena pyriformis using ferromagnetic nanoparticles: A tool for

fabrication of microbiorobots," *Appl. Phys. Lett.*, vol. 97, no. 17, 2010.

[20] J. Zhuang, B. W. Park, and M. Sitti, "Propulsion and chemotaxis in bacteria-driven microswimmers," *Adv. Sci.*, vol. 4, no.9, pp. 1700109, 2017.

[21] R. W. Carlsen and M. Sitti, "Bio-hybrid cell-based actuators for microsystems," *Small*, vol. 10, no. 19, pp. 3831–3851, 2014.

[22] L. Schwarz, M. Medina-Sánchez, and O. G. Schmidt, "Hybrid biomicromotors," *Appl. Phys. Rev.*, vol. 4, no. 3, 2017.

[23] X. Yan *et al.*, "Multifunctional biohybrid magnetite microrobots for imaging-guided therapy," *Sci. Robot.*, vol. 2, no. 12, p. eaaq1155, 2017.

[24] T. H. Tran, D. Hyung Kim, J. Kim, M. Jun Kim, and D. Byun, "Use of an AC electric field in galvanotactic on/off switching of the motion of a microstructure blotted by Serratia marcescens," *Appl. Phys. Lett.*, vol. 99, no. 6, 2011.

[25] E. B. Steager, M. S. Sakar, D. H. Kim, V. Kumar, G. J. Pappas, and M. J. Kim, "Electrokinetic and optical control of bacterial microrobots," *J. Micromechanics Microengineering*, vol. 21, no. 3, pp. 035001, 2011.

[26] C. Pawashe, S. Floyd, and M. Sitti, "Multiple magnetic microrobot control using electrostatic anchoring," *Appl. Phys. Lett.*, vol. 94, no. 16, pp. 2–4, 2009.

[27] L. Dai, N. Jiao, X. Wang, and L. Liu, "A micromanipulator and transporter based on vibrating bubbles in an open chip environment," *Micromachines*, vol. 8, no. 4, pp. 130, 2017.

[28] W. Hu, K. S. Ishii, and A. T. Ohta, "Micro-assembly using optically controlled bubble microrobots," *Appl. Phys. Lett.*, vol. 99, no. 9, p. 094103, 2011.

[29] M. A. Rahman, J. Cheng, Q. Fan, and A. T. Ohta, "Automated actuation of multiple bubble microrobots using computer-generated holograms," in *Proceedings of the International Society for Optics and Photonics (SPIE) - Next-Generation Robotics II; and Machine*

Intelligence and Bio-inspired Computation: Theory and Applications IX, vol. 9494, pp. 94940G, 2015.

[30] W. Hu, K. S. Ishii, Q. Fan, and A. T. Ohta, "Hydrogel microrobots actuated by optically generated vapour bubbles," *Lab Chip*, vol. 12, no. 19, p. 3821, 2012.

[31] W. Hu, Q. Fan, and A. T. Ohta, "An opto-thermocapillary cell micromanipulator," *Lab Chip*, vol. 13, no. 12, pp. 2285-2291, 2013.

[32] Q. Fan, W. Hu, and A. T. Ohta, "Efficient single-cell poration by microsecond laser pulses," *Lab Chip*, vol. 15, no. 2, pp. 581-588, 2015.

[33] M. A. Rahman, Z. Wang, and A. T. Ohta, "Collaborative micromanipulation using multiple bubble microrobots in an open reservoir," *Micro Nano Lett.*, vol. 12, no. 11, pp. 1–6, 2017.

[34] M. A. Rahman, N. Takahashi, K. F. Siliga, N. K. Ng, Z. Wang, and A. T. Ohta, "Vision-assisted micromanipulation using closed-loop actuation of multiple microrobots," *Robot. Biomimetics*, vol. 4, no. 1, p. 7, 2017.

[35] M. Hagiwara, T. Kawahara, T. Iijima, and F. Arai, "High-speed magnetic microrobot actuation in a microfluidic chip by a fine V-groove surface," *IEEE Trans. Robot.*, vol. 29, no. 2, pp. 363-372, 2013.

[36] A. Servant, F. Qiu, M. Mazza, K. Kostarelos, and B. J. Nelson, "Controlled in vivo swimming of a swarm of bacteria-like microrobotic flagella," *Adv. Mater.*, vol. 27, no. 19, pp. 2981-2988, 2015.

[37] D. Cappelleri, D. Efthymiou, A. Goswami, N. Vitoroulis, and M. Zavlanos, "Towards mobile microrobot swarms for additive micromanufacturing," *Int. J. Adv. Robot. Syst.*, vol. 11, no. 9, pp. 150, 2014.

[38] S. Tottori, N. Sugita, R. Kometani, S. Ishihara, and M. Mitsuishi, "Selective control method for multiple magnetic helical microrobots," *J. Micro-Nano Mechatronics*, vol. 6, no. 3–4, pp. 89–95, 2011.

[39] S. Floyd, E. Diller, C. Pawashe, and M. Sitti, "Control methodologies for a heterogeneous group of untethered magnetic micro-robots," *Int. J. Rob. Res.*, vol. 30, no. 13, pp. 1553–1565, 2011.

[40] M. M. Stanton, B. W. Park, A. Miguel-López, X. Ma, M. Sitti, and S. Sánchez, "Biohybrid microtube swimmers driven by single captured bacteria," *Small*, vol. 13, no. 19, pp. 1–10, 2017.

[41] K. S. Ishii, W. Hu, and A. T. Ohta, "Cooperative micromanipulation using optically controlled bubble microrobots," *Proc. - IEEE Int. Conf. Robot. Autom.*, pp. 3443–3448, 2012.

[42] A. Grichener and G. M. Rebeiz, "High-reliability RF-MEMS switched capacitors with digital and analog tuning characteristics," *IEEE Trans. Microw. Theory Tech.*, vol. 58, no. 10, pp. 2692-2701, 2010.

[43] H. D. Nguyen *et al.*, "Angular vertical comb-driven tunable capacitor with high-tuning capabilities," *J. Microelectromechanical Syst.*, vol. 13, no. 3, pp. 406-413, 2004.

[44] C. F. Moldovan, W. A. Vitale, P. Sharma, M. Tamagnone, J. R. Mosig, and A. M. Ionescu, "Graphene quantum capacitors for high frequency tunable analog applications," *Nano Lett.*, vol.16, no. 8, pp.4746-4753, 2016.

[45] M. A. Rahman, R. C. Gough, M. M. Moorefield, G. B. Zhang, W. A. Shiroma, and A. T. Ohta, "Electrically actuated liquid metal for reconfigurable RF devices," *2016 IEEE/ACES Int. Conf. Wirel. Inf. Technol. ICWITS 2016 Syst. Appl. Comput. Electromagn. ACES 2016 - Proc.*, pp. 11–12, 2016.

[46] J. H. So, J. Thelen, A. Qusba, G. J. Hayes, G. Lazzi, and M. D. Dickey, "Reversibly deformable and mechanically tunable fluidic antennas," *Adv. Funct. Mater.*, vol. 19, no. 22, pp. 3632-3637, 2009.

[47] A. M. Morishita, C. K. Y. Kitamura, A. T. Ohta, and W. A. Shiroma, "A liquid-metal monopole array with tunable frequency, gain, and beam steering," *IEEE Antennas Wirel. Propag. Lett.*, vol. 12, pp. 1388-1391, 2013.

[48] C. H. Chen and D. Peroulis, "Liquid RF MEMS wideband reflective and absorptive switches," in *IEEE Transactions on Microwave Theory and Techniques*, vol. 55, no. 12, pp. 2919-2929, 2007.

[49] W. Irshad and D. Peroulis, "A 12-18 GHz electrostatically tunable liquid metal RF MEMS resonator with quality factor of 1400-1840," in *IEEE MTT-S International Microwave Symposium Digest*, pp. 1-4, 2011.

[50] X. Liu, L. P. B. Katehi, and D. Peroulis, "Non-toxic liquid metal microstrip resonators," in *Asia Pacific Microwave Conference (APMC)*, pp. 131-134, 2009.

[51] K. S. Yun, I. J. Cho, J. U. Bu, C. J. Kim, and E. Yoon, "A surface-tension driven micropump for low-voltage and low-power operations," *J. Microelectromechanical Syst.*, vol. 11, no. 5, pp. 454-461, 2002.

[52] R. C. Gough, A. M. Morishita, J. H. Dang, M. R. Moorefield, W. A. Shiroma, and A. T. Ohta, "Rapid electrocapillary deformation of liquid metal with reversible shape retention," *Micro Nano Syst. Lett.*, vol. 3, no. 1, p.4, 2015.

[53] R. C. Gough *et al.*, "Self-Actuation of Liquid Metal via Redox Reaction," *ACS Appl. Mater. Interfaces*, vol. 8, no. 1, pp. 6-10, 2016.

[54] Q. Gu, *RF tunable devices and subsystems: Methods of modeling, analysis, and applications*. Switzerland: Springer, Cham, 2015.

[55] R. C. Gough, J. H. Dang, A. M. Morishita, A. T. Ohta, and W. A. Shiroma, "Frequency-tunable slot antenna using continuous electrowetting of liquid metal," in *IEEE MTT-S International Microwave Symposium Digest*, pp. 1-4, 2014.

[56] J. H. Dang, R. C. Gough, A. M. Morishita, A. T. Ohta, and W. A. Shiroma, "Liquid-metal frequency-reconfigurable slot antenna using air-bubble actuation," *Electron. Lett.*, vol. 51, no. 21, pp. 1630-1632, 2015.

[57] M. A. Griswold *et al.*, "Generalized autocalibrating partially parallel acquisitions (GRAPPA)," *Magn. Reson. Med.*, vol. 47, no. 6, pp. 1202-1210, 2002.

[58] M. Lustig, D. Donoho, and J. M. Pauly, "Sparse MRI: The application of compressed sensing for rapid MR imaging," *Magn. Reson. Med.*, vol. 58, no. 6, pp. 1182-1195, 2007.

[59] O. Ocali and E. Atalar, "Ultimate intrinsic signal-to-noise ratio in MRI," *Magn. Reson. Med.*, vol. 39, no. 3, pp. 462-473, 1998.

[60] P. Caravan, J. J. Ellison, T. J. McMurry, and R. B. Lauffer, "Gadolinium(III) chelates as MRI contrast agents: structure, dynamics, and applications.," *Chem. Rev.*, vol. 99, no. 9, pp. 2293-2352, 1999.

[61] P. B. Roemer, W. A. Edelstein, C. E. Hayes, S. P. Souza, and O. M. Mueller, "The NMR phased array," *Magn. Reson. Med.*, vol. 16, no. 2, pp.192-225, 1990.

[62] F. Wiesinger, P. Boesiger, and K. P. Pruessmann, "Electrodynamics and ultimate SNR in parallel MR imaging," *Magn. Reson. Med.*, vol. 52, no. 2, pp. 376-390, 2004.

[63] K. P. Pruessmann, M. Weiger, M. B. Scheidegger, and P. Boesiger, "SENSE: Sensitivity encoding for fast MRI," *Magn. Reson. Med.*, vol. 42, no. 5, pp. 952-962, 1999.

[64] J. A. Nordmeyer-Massner, N. De Zanche, and K. P. Pruessmann, "Stretchable coil arrays: Application to knee imaging under varying flexion angles," *Magn. Reson. Med.*, vol. 67, no. 3, pp. 872-879, 2012.

[65] J. R. Corea *et al.*, "Screen-printed flexible MRI receive coils," *Nat. Commun.*, vol. 7, p.10839, 2016.

[66] J. A. Malko, E. C. McClees, I. F. Braun, P. C. Davis, and J. C. Hoffman, "A flexible mercury-filled surface coil for MR imaging," *Am. J. Neuroradiol.*, vol. 7, no. 2, pp. 246-247, 1986.

[67] D. Zhang and Y. Rahmat-Samii, "Electro-textiles as potential candidate of flexible MRI RF coil for stroke prevention," in *United States National Committee of URSI National IEEE Radio Science Meeting (USNC-URSI NRSM)*, pp. 1–2, 2017.

[68] G. Adriany *et al.*, "A geometrically adjustable 16-channel transmit/receive transmission

line array for improved RF efficiency and parallel imaging performance at 7 Tesla," *Magn. Reson. Med.*, vol. 59, no. 3, pp. 590-597, 2008.

[69] Center for human reproduction, "In vitro fertilization (IVF) success rates," *Our IVF Pregnancy Rates & Outcomes*, 2018. [Online]. Available: https://www.centerforhumanreprod.com/about/pregnancyrates/.

[70] E. J. Margalioth, A. Ben-Chetrit, M. Gal, and T. Eldar-Geva, "Investigation and treatment of repeated implantation failure following IVF-ET," *Human Reproduction*. 2006.

[71] J. M. R. Gerris, "Single embryo transfer and IVF/ICSI outcome: A balanced appraisal," *Human Reproduction Update*. vol. 21, no. 12, pp. 3036-3043, 2005.

[72] M. F. G. Verberg *et al.*, "Why do couples drop-out from IVF treatment? A prospective cohort study.," *Hum. Reprod.*, vol. 23, no. 9, pp. 2050-2055, 2008.

[73] D. K. Gardner, E. Surrey, D. Minjarez, A. Leitz, J. Stevens, and W. B. Schoolcraft, "Single blastocyst transfer: A prospective randomized trial," *Fertil. Steril.*, vol. 81, no. 3, pp. 551-555, 2004.

[74] A. E. Baxter Bendus, J. F. Mayer, S. K. Shipley, and W. H. Catherino, "Interobserver and intraobserver variation in day 3 embryo grading," *Fertil. Steril.*, vol. 86, no. 6, pp. 1608-1615, 2006.

[75] C. Márquez, M. Sandalinas, M. Bahçe, M. Al ikani, and S. Munné, "Chromosome abnormalities in 1255 cleavage-stage human embryos," *Reprod. Biomed. Online*, vol. 1, no. 1, pp. 17-26, 2000.

[76] A. Veiga *et al.*, "Confirmation of diagnosis in preimplantation genetic diagnosis (PGD) through blastocyst culture: Preliminary experience," *Prenat. Diagn.*, vol. 19, no. 13, pp. 1242-1247, 1999.

[77] T. Petit, L. Zhang, K. E. Peyer, B. E. Kratochvil, and B. J. Nelson, "Selective trapping and manipulation of microscale objects using mobile microvortices," *Nano Lett.*, vol. 12, no. 1, pp. 156-160, 2012.

[78] E. B. Steager, M. Selman Sakar, C. Magee, M. Kennedy, A. Cowley, and V. Kumar, "Automated biomanipulation of single cells using magnetic microrobots," *Int. J. Rob. Res.*, vol. 32, no. 3, pp. 346-359, 2013.

[79] L. Feng, M. Hagiwara, A. Ichikawa, and F. Arai, "On-Chip enucleation of bovine oocytes using microrobot-assisted flow-speed control," *Micromachines*, vol. 4, no. 2 , pp. 272-285, 2013.

[80] S. Tasoglu, E. Diller, S. Guven, M. Sitti, and U. Demirci, "Untethered micro-robotic coding of three-dimensional material composition," *Nat. Commun.*, vol. 5, pp. 1–9, 2014.

[81] Z. Ye and M. Sitti, "Dynamic trapping and two-dimensional transport of swimming microorganisms using a rotating magnetic microrobot," *Lab a Chip - Miniaturisation Chem. Biol.*, vol. 5, pp. 3124, 2014.

[82] D. Ahmed *et al.*, "Rotational manipulation of single cells and organisms using acoustic waves," *Nat Commun*, vol 7, pp. 11085, 2016.

[83] S. Yim, E. Gultepe, D. H. Gracias, and M. Sitti, "Biopsy using a magnetic capsule endoscope carrying, releasing, and retrieving untethered microgrippers," *IEEE Trans. Biomed. Eng.*, vol. 61, no. 2, pp. 513-521, 2014.

[84] U. A. Gurkan, S. Tasoglu, D. Kavaz, M. C. Demirel, and U. Demirci, "Emerging technologies for assembly of microscale hydrogels," *Adv. Healthc. Mater.*, vol. 1, no. 2, pp. 149-158, 2012.

[85] W. Hu, Q. Fan, and A. T. Ohta, "Assembly of cell-laden microgels by an optically controlled bubble manipulator," *17th Int. Conf. Miniaturized Syst. Chem. Life Sci.*, Freiburg, Germany, 2013.

[86] B. R. Donald, C. G. Levey, I. Paprotny, and D. Rus, "Planning and control for microassembly of structures composed of stress-engineered MEMS microrobots," *Int. J. Rob. Res.*, vol. 32, no. 2, pp. 218-246, 2013.

[87] K. E. Peyer, L. Zhang, and B. J. Nelson, "Bio-inspired magnetic swimming microrobots for

biomedical applications," *Nanoscale*, vol. 5, no. 4, pp.1259-1272, 2013.

[88] E. Diller, J. Giltinan, G. Z. Lum, Z. Ye, and M. Sitti, "Six-degree-of-freedom magnetic actuation for wireless microrobotics," *Int. J. Rob. Res.*, vol 35, no. 1-3, pp. 114-128, 2016.

[89] Q. Fu, S. Guo, Y. Yamauchi, H. Hirata, and H. Ishihara, "A novel hybrid microrobot using rotational magnetic field for medical applications," *Biomed. Microdevices*, vol. 17, no. 2 , pp. 31, 2015.

[90] Y. Jung, J. Shim, K. Kwon, J. B. You, K. Choi, and K. Yu, "Hybrid integration of III-V semiconductor lasers on silicon waveguides using optofluidic microbubble manipulation," *Sci. Rep.*, vol. 6, pp. 29841, 2016.

[91] W. Hu, Q. Fan, and A. T. Ohta, "Interactive actuation of multiple opto-thermocapillary flow-addressed bubble microrobots," *Robot. Biomimetics*, vol. 1, no. 1, pp. 14, 2014.

[92] M. A. Rahman, J. Cheng, and A. T. Ohta, "Parallel actuation and independent addressing of many bubble microrobots," in *11th IEEE Annual International Conference on Nano/Micro Engineered and Molecular Systems*, pp. 279-282, 2016.

[93] J. H. Shin, J. Seo, J. Hong, and S. K. Chung, "Hybrid optothermal and acoustic manipulations of microbubbles for precise and on-demand handling of micro-objects," *Sensors Actuators, B Chem.*, vol. 246, pp 415-420, 2017.

[94] S. Martel, "Bacterial microsystems and microrobots," *Biomed. Microdevices*, vol. 14, no. 6, pp.1033-1045, 2012.

[95] J. Zhuang, R. W. Carlsen, and M. Sitti, "PH-taxis of biohybrid microsystems," *Sci. Rep.*, vol. 5, p.11403, 2015.

[96] J. Zhuang and M. Sitti, "Chemotaxis of bio-hybrid multiple bacteria-driven microswimmers," *Sci. Rep.*, vol. 6, pp. 32135, 2016.

[97] R. Pelrine *et al.*, "Diamagnetically levitated robots: An approach to massively parallel robotic systems with unusual motion properties," in *Proceedings - IEEE International*

Conference on Robotics and Automation, pp. 739-744, 2012.

[98] B. G. Chung, K. H. Lee, A. Khademhosseini, and S. H. Lee, "Microfluidic fabrication of microengineered hydrogels and their application in tissue engineering," *Lab on a Chip*. vol 12, no. 1, pp. 45-59, 2012.

[99] P. Y. Chiou, A. T. Ohta, and M. C. Wu, "Massively parallel manipulation of single cells and microparticles using optical images," *Nature*, vol. 436, no. 7049, pp. 370–372, 2005.

[100] C. Mio, T. Gong, A. Terray, and D. W. M. Marr, "Design of a scanning laser optical trap for multiparticle manipulation," *Rev. Sci. Instrum.*, vol. 71, no. 5, pp. 2196–2200, 2000.

[101] D. G. Grier, "A revolution in optical manipulation," *Nature*, vol. 424, no. 6950, pp. 810–816, 2003.

[102] M. Sitti, *Mobile Microrobotics*. MIT Press, Jun 9, 2017.

[103] S. Bruckenstein, "Physicochemical hydrodynamics," *Nature*, 1977.

[104] E. Lajeunesse and G. M. Homsy, "Thermocapillary migration of long bubbles in polygonal tubes. II. Experiments," *Phys. Fluids*, vol. 15, no. 2, pp. 308-314, 2003.

[105] R. W. Bowman *et al.*, "Red tweezers: Fast, customisable hologram generation for optical tweezers," *Comput. Phys. Commun.*, vol. 185, no. 1, pp. 268-273, 2014.

[106] R. W. Bowman, A. J. Wright, and M. J. Padgett, "An SLM-based Shack-Hartmann wavefront sensor for aberration correction in optical tweezers," *J. Opt.*, vol. 12, no. 12 pp. 124004, 2010.

[107] I. A. Palani, N. J. Vasa, M. Singaperumal, and T. Okada, "Investigation on laser-annealing and subsequent laser-nanotexturing of amorphous silicon (a-Si) films for photovoltaic application," *J. Laser Micro Nanoeng.*, vol. 5, no. 2, 2010.

[108] O. Yavas and M. Takai, "Effect of substrate absorption on the efficiency of laser patterning of indium tin oxide thin films," *J. Appl. Phys.*, vol. 85, no. 8, pp. 4207-4212, 1999.

[109] M. A. Rahman, J. Cheng, Q. Fan, and A. T. Ohta, "Automated actuation of multiple bubble microrobots using computer-generated holograms," *Proc. SPIE Next-Generation Robot. II; Mach. Intell. Bio-inspired Comput. Theory Appl. IX*, vol. 9494, p. 94940G, 2015.

[110] M. A. Rahman, J. Cheng, and A. T. Ohta, "Automated Cooperative Micro-Assembly Using Multiple Bubble Microrobots," in *9th IEEE International Conference on Nano/Molecular Medicine and Engineering*, pp. 15-18, 2015.

[111] S. Martel, "Microrobotics in the vascular network: present status and next challenges," *J. Micro-Bio Robot.*, vol. 8, no. 1, pp. 41-52, 2013.

[112] O. Ergeneman, G. Dogangil, M. P. Kummer, J. J. Abbott, M. K. Nazeeruddin, and B. J. Nelson, "A magnetically controlled wireless optical oxygen sensor for intraocular measurements," *IEEE Sens. J.*, vol. 8, no. 1, pp. 29-37, 2008.

[113] J. Giltinan, E. Diller, C. Mayda, and M. Sitti, "Three-dimensional robotic manipulation and transport of micro-scale objects by a magnetically driven capillary micro-gripper," *Proc. - IEEE Int. Conf. Robot. Autom.*, pp. 2077–2082, 2014.

[114] S. Kim *et al.*, "Fabrication and characterization of magnetic microrobots for three-dimensional cell culture and targeted transportation," *Adv. Mater.*, vol. 25, no. 41, pp. 5863-5868, 2013.

[115] A. Mishra *et al.*, "Optoelectric patterning: Effect of electrode material and thickness on laser-induced AC electrothermal flow," *Electrophoresis*, vol. 37, no. 4, pp. 658-665, 2016.

[116] N. Takahashi, M. A. Rahman, A. T. Ohta, and Z. Wang, "Analysis of geometric and motion characteristics of bubble microrobots for caging based cell manipulation," in *10th International Conference on New Actuators (Actuator 2006)th IEEE International Conference on Nano/Molecular Medicine and Engineering*, 2016.

[117] B. Jeong, S. W. Kim, and Y. H. Bae, "Thermosensitive sol-gel reversible hydrogels," *Advanced Drug Delivery Reviews*. vol. 64, pp. 154-162, 2012.

[118] S. E. Chung, X. Dong, and M. Sitti, "Three-dimensional heterogeneous assembly of coded

microgels using an untethered mobile microgripper," *Lab Chip*, vol. 15, no. 7, pp. 1667–1676, 2015.

[119] D. R. Albrecht, G. H. Underhill, T. B. Wassermann, R. L. Sah, and S. N. Bhatia, "Probing the role of multicellular organization in three-dimensional microenvironments," *Nat. Methods*, vol. 3, no. 5, pp. 369, 2006.

[120] M. He, J. S. Edgar, G. D. M. Jeffries, R. M. Lorenz, J. P. Shelby, and D. T. Chiu, "Selective encapsulation of single cells and subcellular organelles into picoliter- and femtoliter-volume droplets," *Anal. Chem.*, vol. 77, no. 6, pp. 1539-1544, 2005.

[121] E. Briganti, P. Losi, A. Raffi, M. Scoccianti, A. Munaò, and G. Soldani, "Silicone based polyurethane materials: A promising biocompatible elastomeric formulation for cardiovascular applications," *J. Mater. Sci. Mater. Med.*, vol. 17, no. 3, pp. 259-266, 2006.

[122] W. L. Robb, "Thin silicon membranes. Their permeation properties and some applications.," *Ann. N. Y. Acad. Sci.*, vol. 146, no. 1, pp. 119-137, 1968.

[123] V. Srinivasan, V. K. Pamula, and R. B. Fair, "An integrated digital microfluidic lab-on-a-chip for clinical diagnostics on human physiological fluids," *Lab Chip*, vol. 4, no. 4, pp. 310-315, 2004.

[124] S.-Y. Teh, R. Lin, L.-H. Hung, and A. P. Lee, "Droplet microfluidics," *Lab Chip*, vol. 8, no. 2, pp. 198-220, 2008.

[125] V. Srinivasan, V. Pamula, M. Pollack, and R. Fair, "Clinical diagnostics on human whole blood, plasma, serum, urine, saliva, sweat, and tears on a digital microfluidic platform," *Proc. μTAS*, pp. 1287-1290, 2003.

[126] D. Kim, A. Liu, E. Diller, and M. Sitti, "Chemotactic steering of bacteria propelled microbeads," *Biomed. Microdevices*, vol. 4, no. 6, pp. 1009-1017, 2012.

[127] O. C. Jeong and S. Konishi, "Experimental study on a single particle trap with a pneumatic vibrator matrix," *Microfluid. Nanofluidics*, vol. 6, no. 1, pp. 139-144, 2009.

[128] C. Moraes, J. H. Chen, Y. Sun, and C. A. Simmons, "Microfabricated arrays for high-throughput screening of cellular response to cyclic substrate deformation," *Lab Chip*, vol. 10, no. 2, pp. 227-234, 2010.

[129] M. A. Rahman and A. T. Ohta, "Parallel actuation of multiple bubble microrobots in saline solution in an open reservoir," in *2017 IEEE 12th International Conference on Nano/Micro Engineered and Molecular Systems, NEMS 2017*, pp. 738-741, 2017.

[130] W. Hu, K. S. Ishii, and A. T. Ohta, "Micro-assembly using optically controlled bubble microrobots in saline solution," in *Proceedings - IEEE International Conference on Robotics and Automation*, pp. 733-738, 2012.

[131] Y. Li *et al.*, "Rapid Assembly of Heterogeneous 3D Cell Microenvironments in a Microgel Array," *Adv. Mater.*, vol. 28, no. 18, pp. 3543-3548, 2016.

[132] Y. F. Tian, J. M. Devgun, and J. H. Collier, "Fibrillized peptide microgels for cell encapsulation and 3D cell culture," *Soft Matter*, vol. 7, no. 13, pp. 6005-6011, 2011.

[133] L. Feng, P. Di, and F. Arai, "High-precision motion of magnetic microrobot with ultrasonic levitation for 3-D rotation of single oocyte," *Int. J. Rob. Res.*, vol. 5, no. 12, pp. 1445-1458, 2016.

[134] R. Milo and R. Phillips, "Cell Biology By the Numbers," *Curr. Opin. Plant Biol.*, 2014.

[135] P. S. S. Kim, A. Becker, Y. Ou, A. A. Julius, and M. J. Kim, "Imparting magnetic dipole heterogeneity to internalized iron oxide nanoparticles for microorganism swarm control," *J. Nanoparticle Res.*, vol. 17, no. 3, pp. 144, 2015.

[136] N. Otsu, "A Threshold Selection Method from Gray-Level Histograms," *IEEE Trans. Syst. Man. Cybern.*, vol. 9, no. 1, pp. 62-66, 1979.

[137] S. Chowdhury, B. V. Johnson, W. Jing, and D. J. Cappelleri, "Designing local magnetic fields and path planning for independent actuation of multiple mobile microrobots," *J. Micro-Bio Robot.*, vol. 12, no. 1-4, pp. 21-31, 2017.

[138] D. J. Cappelleri and Z. Fu, "Towards flexible, automated microassembly with caging micromanipulation," in *Proceedings - IEEE International Conference on Robotics and Automation*, pp. 1427-1432, 2013.

[139] N. Takahashi, Z. Wang, M. A. Rahman, J. Cheng, and A. T. Ohta, "Automated micro-object caging using bubble microrobots," in *11th IEEE Annual International Conference on Nano/Micro Engineered and Molecular Systems(NEMS),* pp. 237-240, 2016.

[140] A. Ghanbari, P. H. Chang, B. J. Nelson, and H. Choi, "Magnetic actuation of a cylindrical microrobot using time-delay-estimation closed-loop control: Modeling and experiments," *Smart Mater. Struct.*, vol. 23, no. 3, pp. 035013, 2014.

[141] J. Li *et al.*, "Swimming Microrobot Optical Nanoscopy," *Nano Lett.*, vol. 16, no. 10, pp. 6604-6609, 2016.

[142] Drs. Hill & Thomas Co., "Specializing in Radiology and Medical Imaging," 2018. [Online]. Available: https://www.hillandthomas.com/faq.shtml.

[143] S. Nasreen *et al.*, "Polymer Dielectrics for Capacitor Application," in *Kirk-Othmer Encyclopedia of Chemical Technology*, 2017.

[144] T. Liu, P. Sen, and C. J. Kim, "Characterization of nontoxic liquid-metal alloy galinstan for applications in microdevices," *J. Microelectromechanical Syst.*, vol. 21, no. 2, pp. 443-450, 2012.

[145] R. C. Gough, A. M. Morishita, J. H. Dang, W. Hu, W. A. Shiroma, and A. T. Ohta, "Continuous Electrowetting of Non-toxic Liquid Metal for RF Applications," *IEEE Access*, vol. 2, pp. 874-882, 2014.

[146] World Health Organization, "Infertility definitions and terminology." [Online]. Available: http://www.who.int/reproductivehealth/topics/infertility/definitions/en/.

[147] P. De Sutter, J. Van der Elst, T. Coetsier, and M. Dhont, "Single embryo transfer and multiple pregnancy rate reduction in IVF/ICSI: a 5-year appraisal," *Reprod. Biomed. Online*, vol. 6, no. 4, pp. 464-469, 2003.

[148] I. Boiso, A. Veiga, and R. G. Edwards, "Fundamentals of human embryonic growth in vitro and the selection of high-quality embryos for transfer," *Reprod. Biomed. Online*, vol. 5, no. 3, pp. 328–350, 2002.

[149] T. T. F. Huang, K. Chinn, T. Kosasa, H. J. Ahn, and B. Kessel, "Morphokinetics of human blastocyst expansion in vitro," *Reprod. Biomed. Online*, vol. 33, no. 6, pp. 659-667, 2016.

[150] E. S. Filho, J. A. Noble, M. Poli, T. Griffiths, G. Emerson, and D. Wells, "A method for semi-automatic grading of human blastocyst microscope images," *Hum. Reprod.*, vol. 27, no. 9, pp. 2641–2648, 2012.

[151] A. Mölder, S. Drury, N. Costen, G. M. Hartshorne, and S. Czanner, "Semiautomated analysis of embryoscope images: Using localized variance of image intensity to detect embryo developmental stages," *Cytom. Part A*, 87, no. 2, pp. 119-128, 2015.

[152] K. F. Lei, "Review on impedance detection of cellular responses in micro/nano environment," *Micromachines*. vol. 1, pp. 1-12, 2014.

[153] F. Bruni, G. Careri, and J. S. Clegg, "Dielectric properties of Artemia cysts at low water contents. Evidence for a percolative transition," *Biophys. J.*, vol. 55, no. 2, pp. 331-338, 1989.

[154] P. Lavens and P. Sorgeloos, *Manual on the production and use of live food for aquaculture*. no. 361, 1996.

[155] K. Schoenbach *et al.*, "Effect of submicrosecond electric fields on microorganisms: experiments and applications," in *Proc. International Society for Optics and Photonics (SPIE), Novel Applications of Lasers and Pulsed Power*, vol. 2374, pp. 199-206, 1995.